ABSTRACT

HELIOSEISMIC DIAGNOSTICS OF ACTIVE REGIONS AND THEIR MAGNETIC FIELDS

by
John T. Stefan

While two and a half decades of nearly constant observation by the Solar and Heliospheric Observatory (SOHO) and the Solar Dynamics Observatory (SDO) spacecraft have yielded key insights into the structure and dynamics of active regions, it is still unclear if active regions can be identified before emerging on the solar surface and, once emerged, whether the subsurface structure of an active region's magnetic field can be measured. Regarding the dynamical processes associated with active regions, the height and mechanism of sunquake excitation remains poorly understood. To answer these questions, a comprehensive survey of active region magnetic fields and their associated helioseismic signatures for both the pre-emergence and post-emergence phase is completed.

For the former, deviations of the mean phase travel time of acoustic waves are used to detect the rise of magnetic flux from the solar interior. Calibration and testing of the time-distance technique is performed using simulations of submerged sound speed perturbations. A detailed case study of select active regions is performed, and the technique is then applied to a collection of 46 active regions to determine the statistical significance of mean travel time perturbations as a signature of active region emergence.

Next, a novel technique is developed for the assessment of existing active region magnetic fields. By combining the travel time of acoustic waves propagating in varying directions, perturbations due to subsurface horizontal magnetic fields are isolated from structural changes. The resulting measurements provide a proxy for the magnitude of the horizontal magnetic field as well as a direct measurement of

the field's azimuth. The technique is applied to a sunspot simulation for validation, and is then used to investigate the subsurface magnetic structure of several observed sunspots.

Finally, a model of solar acoustic wave propagation is constructed using the compressible form of the mass, momentum, and entropy conservation equations to study the excitation of sunquakes. The constructed model is used to determine at what height sunquakes are excited, what mode of excitation is most energetically favorable, and what properties of particle beams are relevant to sunquake excitation. The excitation height is determined from comparison of observed events with a catalogue of simulated sunquakes for a range of excitation locations and for several excitation mechanisms, which allows the excitation height and energy to be estimated. Additionally, the output of FP proton beam simulations are used to derive forcing functions for the excitation of sunquakes in the model to determine the dependence of wave front amplitude on the low-energy cut-off.

HELIOSEISMIC DIAGNOSTICS OF ACTIVE REGIONS AND THEIR MAGNETIC FIELDS

by
John T. Stefan

A Dissertation
Submitted to the Faculty of
New Jersey Institute of Technology and
Rutgers, The State University of New Jersey-Newark,
in Partial Fulfillment of the Requirements for the Degree of
Doctor of Philosophy in Applied Physics

Department of Physics

December 2022

APPROVAL PAGE

HELIOSEISMIC DIAGNOSTICS OF ACTIVE REGIONS AND THEIR MAGNETIC FIELDS

John T. Stefan

Dr. Alexander G. Kosovichev, Dissertation Advisor — Date
Distinguished Professor of Physics, NJIT

Dr. Haimin Wang, Committee Member — Date
Distinguished Professor of Physics, NJIT

Dr. Gregory D. Fleishman, Committee Member — Date
Distinguished Research Professor of Physics, NJIT

Dr. Gelu M. Nita, Committee Member — Date
Research Professor of Physics, NJIT

Dr. Xuejian Wu, Committee Member — Date
Assistant Professor of Physics, Rutgers University - Newark

BIOGRAPHICAL SKETCH

Author: John T. Stefan

Degree: Doctor of Philosophy

Date: December 2022

Undergraduate and Graduate Education:

- Doctor of Philosophy in Applied Physics,
  New Jersey Institute of Technology, Newark, NJ, 2022
- Master of Science in Applied Physics,
  New Jersey Institute of Technology, Newark, NJ, 2018
- Bachelor of Science in Applied Physics,
  New Jersey Institute of Technology, Newark, NJ, 2016

Major: Applied Physics

Presentations and Publications:

Stefan, J. T. & Kosovichev, A. G. 2022. Analysis and Modeling of High-Frequency Emission and Deep Seismic Sources of Sunquakes. The Astrophysical Journal 937, L26, doi: 10.3847/2041-8213/ac8f92

Stefan, J. & Kosovichev, A. 2022. Detection of Phase Travel Time Anisotropy from Subsurface Horizontal Magnetic Fields in the Sun. American Astronomical Society Meeting Abstracts 54, 350.14

Stefan, J. T. & Kosovichev, A. G. 2022. Detection of Travel Time Anisotropy from Subsurface Horizontal Magnetic Fields. The Astrophysical Journal 930, 10, doi: 10.3847/1538-4357/ac602a

Stefan, J. & Kosovichev, A. 2021. Examining Correlations Between Helioseismic Signatures of Active Regions and their Emergence. AGU Fall Meeting Abstracts 2021, SH55D-1866

Stefan, J. T., Kosovichev, A. G. & Stejko, A. M. 2021. Analysis of Time-Distance Helioseismology for Detection of Emerging Active Regions. The Astrophysical Journal 913, 87, doi: 10.3847/1538-4357/abf2bf

Stefan, J. T. & Kosovichev, A. G. 2020. Early Detection of Emerging Magnetic Flux using Time-Distance Helioseismology. AGU Fall Meeting Abstracts 2020, SH002-0011

Stefan, J. T. & Kosovichev, A. G. 2020. Estimation of Key Sunquake Parameters through Hydrodynamic Modeling and Cross-correlation Analysis. The Astrophysical Journal 895, 65, doi: 10.3847/1538-4357/ab88ae

Stefan, J. & Kosovichev, A. G. 2019. Time-Dependent Hydrodynamic Modeling of Solar Acoustic Waves. American Astronomical Society Meeting Abstracts #234 234, 302.09

And people are my religion because I believe in them,
People are my enemies and people are my friends.
I have faith in my fellow man,
And I only hope that he has faith in me.

—AJJ, *People*

ACKNOWLEDGMENT

I would first like to thank my dissertation advisor, Dr. Alexander Kosovichev, for his invaluable advice, guidance, and support.

Thank you to my dissertation committee, Drs. Haimin Wang, Gregory Fleishman, Gelu Nita, and Xuejian Wu, for their insightful comments which helped develop this research.

A special thanks to the Heliophysics Modeling and Simulation group at National Aeronautics and Space Administration's Ames Research Center, Drs. Irina Kitiashvili, Alan Wray, Slava Sadykov, Andrey Stejko, and others, whose work both inspired and educated me.

I extend my gratitude to Mr. Martin Tuchman, who supported my Masters' studies and encouraged me to pursue this degree.

I am immeasurably grateful to my dear friends, Maura Canonico and Kaitlyn Mazzeo; my brother, Joey Stefan; and my parents, Ronnie and John Stefan, whose love and support kept me grounded through my studies.

TABLE OF CONTENTS

TABLE OF CONTENTS
(Continued)

Chapter **Page**

TABLE OF CONTENTS
(Continued)

Chapter **Page**

LIST OF TABLES

LIST OF FIGURES

LIST OF FIGURES
(Continued)

Figure **Page**

LIST OF FIGURES
(Continued)

Figure **Page**

CHAPTER 1

INTRODUCTION

1.1 Solar Activity

The first physical model of the solar cycle—variations in the Sun's activity and magnetic field, with period 11 years—was developed by Babcock in 1961 (Babcock, 1961). The clearest visualization of the solar cycle is the butterfly diagram, pictured in Figure 1.1. In his work, Babcock identified five stages of the solar cycle: the initial dipolar field; the amplification of the magnetic field; the formation of bipolar magnetic regions; neutralization and reversal of the dipolar field; and the reversed dipolar field. We are primarily interested in the first three stages of the cycle, as they explain the formation of active regions. In the second stage, the initial dipolar field becomes wound around the Sun as a toroidal field because of the Sun's differential rotation. Instabilities in or near the toroidal field cause kinks, which rise to the surface due to the magnetic pressure, forming the dipolar magnetic regions on the surface that we observe. Babcock also suggests that unipolar magnetic regions may form from the remnants of bipolar magnetic regions, which was supported by Leighton's 1964 study of magnetic dissipation (Leighton, 1964).

The current understanding of solar activity indicates that strong concentrations of magnetic flux originate at the base of the solar convective zone (Fan, 2004), where solar rotation transitions from the inner solid-body rotation to the outer differentially-rotating layers. This region, known as the tachocline, sits at around $0.7R_\odot$ or roughly 200 Mm beneath the photosphere, shown in Figure 1.2 as the boundary between the radiative and convective zones. The deep origins of magnetic flux implies that it must rise through the convective zone before emerging on the solar surface. Recent MHD models have shown that the strong rotational shear at the tachocline can convert

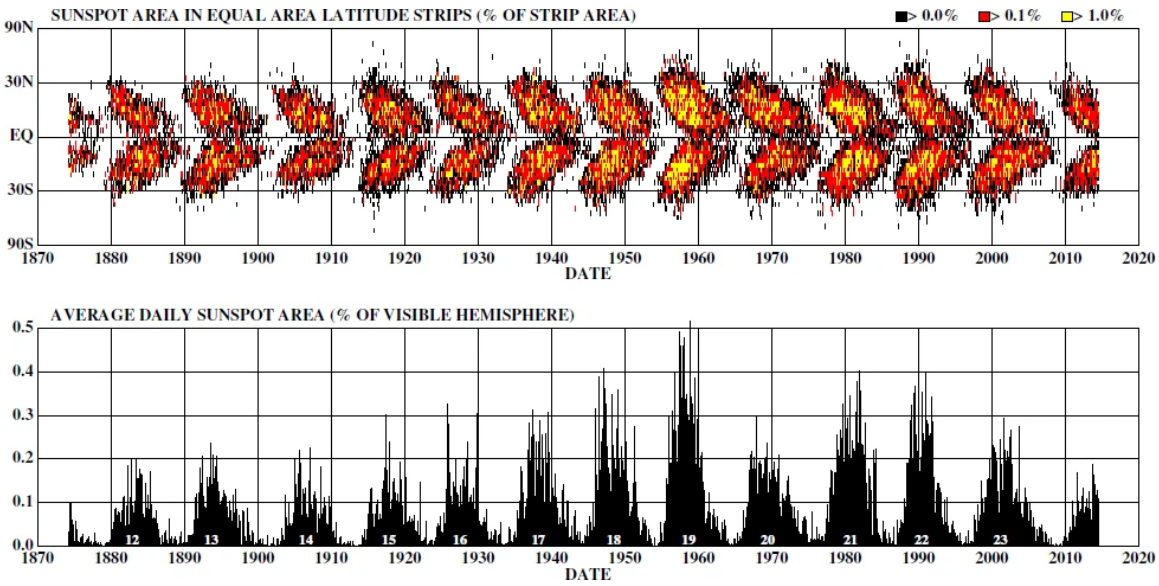

Figure 1.1 A depiction of the solar cycle. The top image is the butterfly diagram, showing the longitudinally averaged sunspot area coverage for each latitude over time, and the averaged daily sunspot coverage over time is shown in the lower image.
Source: Hathaway (2015)

weak background poloidal magnetic fields into strong strong toroidal fields (Hughes et al., 1998; Brummell et al., 2002). This concentration of the magnetic field can be considered as a flux tube, which experiences a buoyant force causing the tube to bend and rise through the convective zone towards the surface (Cline et al., 2003). Other full-scale MHD simulations of magnetic flux emergence have been able to reproduce this process, in which the flux concentration takes between 24 and 68 days to reach the surface depending on the tube's initial twist and symmetry (Fan, 2008).

1.2 Active Regions

Once emerged, concentrations of magnetic flux are called active regions, so called because of their solar flare productivity and other associated energetic phenomenon. One of the more distinct markers of the presence of an active region is an associated sunspot, composed of an inner, darker area called the umbra and an outer, less dark area called the penumbra (see Figure 1.3). The umbra radiates around 20% to 30%

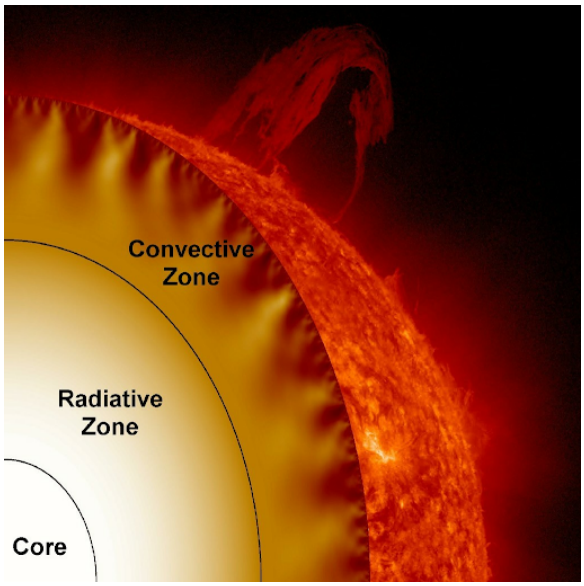

Figure 1.2 The three distinct layers of the Sun's interior. The tachocline is located at the boundary between the convective and radiative zones.
Source: Hathaway (2015)

of the quiet Sun flux and is between one- to two-thousand Kelvin cooler than the surrounding quiet Sun while the penumbra radiates 75% to 85% of the quiet Sun flux and is only a few hundred Kelvin cooler than the surrounding plasma (Solanki, 2003).

It is generally thought that since the magnetic field of active regions is so strong, on the order of thousands of Gauss compared to tens of Gauss in the quiet Sun (Livingston, 2002), that surface convection is suppressed (Solanki, 2003). This, in turn, reduces the energy flux from the convective zone to the surface, reducing the local temperature and therefore brightness. In fact, a direct correspondence between the surface magnetic field and continuum emission intensity of sunspot umbrae as well as the surface temperature has been established, with the continuum emission decreasing linearly with the magnetic field strength and the temperature decreasing with the square of the magnetic field strength (Martinez Pillet & Vazquez, 1993).

An additional consequence of the relative coolness and suppressed convection within sunspots is the Wilson effect (Parker, 1979). Since the Sun is composed of plasma and has no discernible surface, relative heights and the beginning of the

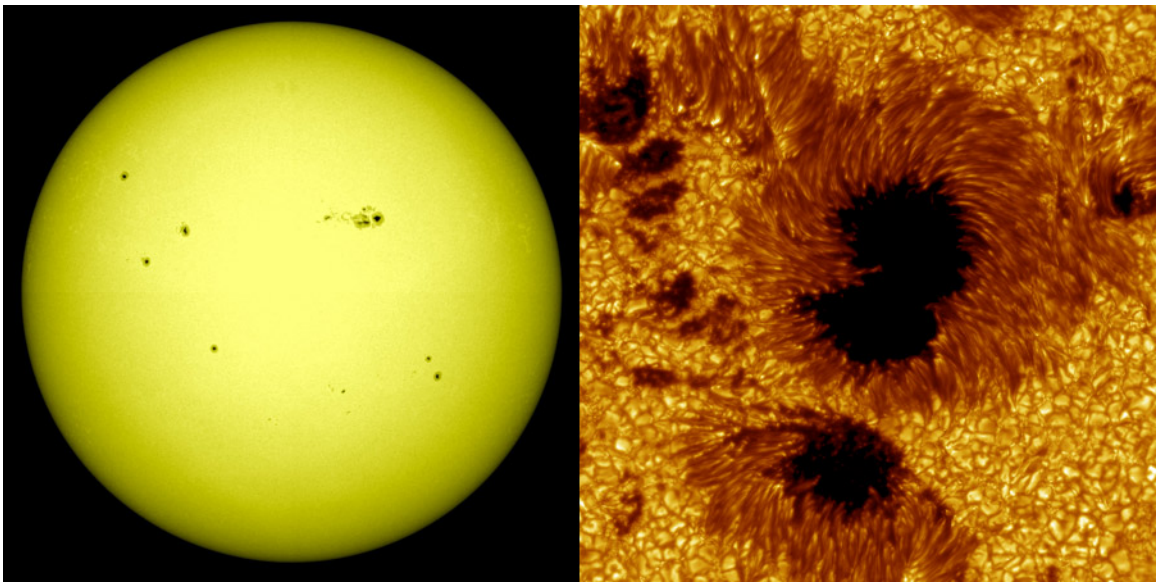

Figure 1.3 The Sun covered with several sunspots and a close-up view of one of the sunspots. The sunspot in the right panel shows a well-developed umbra (inner dark area) and penumbra (outer less-dark area).
Source: UCAR (2011)

solar atmosphere is, by convention, marked by the height at which the optical depth approaches 2/3, which is called the photosphere (Carroll & Ostlie, 1996). Alternatively, the beginning of the photosphere is sometimes marked where the optical depth is equal to unity (Jeffery & Branch, 1990). In either definition, the probability for light to scatter at least once is $\leq$50% and decreases exponentially above the photosphere. Because the hydrogen opacity gives the greatest contribution to the overall photospheric opacity and is very sensitive to temperature, the effective photosphere in sunspots is depressed several hundred kilometers, and up to 2000 km for large sunspots (Prokakis, 1974). This depressed photosphere means that observations of the solar surface within sunspots are actually looking at deeper layers than compared to the surrounding quiet Sun regions, which has complicated implications for helioseismic measurements. Such implications are discussed in, for example, the Acoustic Showerglass series of papers by Lindsey & Braun (2005).

The most important aspect of active regions and sunspots, however, are their ability to produce strong solar flares and occasionally coronal mass ejections (CMEs), which have the potential to seriously impact the local geospace environment. It is widely accepted that solar flares are the result of magnetic reconnection, where twisted magnetic fields with a large amount of stored energy relax to a lower-energy configuration, releasing magnetic energy through heating, shocks, and particle acceleration (Priest & Forbes, 2002; Masuda et al., 1994). CMEs may also be triggered by reconnection, though there are several other mechanisms which may cause a flux rope to rise and eventually erupt, including various MHD instabilities (Chen, 2011). While the two processes are sometimes considered intertwined, not all flares are associated with CMEs and nearly 70% of C-class flares are not accompanied by a CME (Yashiro et al., 2005). However, this proportion decreases significantly with flare intensity, and only 10% of X-class flares are not associated with a CME (Wang & Zhang, 2007). Additionally, there exists a strong correlation between the overall size and amount of magnetic flux within an active region, and the intensity of associated flares (Schrijver, 2007). Based on this relationship several estimates have been given of the greatest possible energy release in a modern solar flare, generally near 10^{33} ergs (Cliver et al., 2022; Tschernitz et al., 2018).

1.3 Helioseismology

In general, helioseismology is the study of solar oscillations and the properties and processes that can be detected using these oscillations. While the precise details regarding the stochastic nature of these oscillations has not been fully understood, it is well-known that strong downdrafts in intergranular lanes are a source of the vast majority of solar pressure waves (Rimmele et al., 1995). These downdrafts occur when plasma rising from the convective region radiatively cools at the surface and sinks back down because of changes in buoyancy (Skartlien & Rast, 2000). Since these

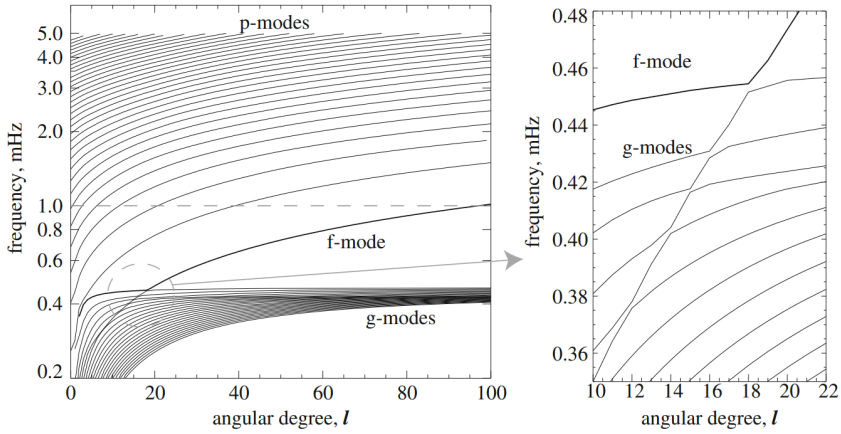

Figure 1.4 Resonant modes computed from the Standard Solar Model (Christensen-Dalsgaard et al., 1996).
Source: Kosovichev (2011)

oscillations are excited stochastically, there are no preferred frequencies. However, which oscillation modes—characterized by a specific frequency and spherical harmonic angular degree l—are resonant is very strongly constrained by solar structure (Gough, 1993). As shown in Figure 1.4, these oscillations are separated into three distinct categories: p-modes, solar pressure waves; the f-mode, a surface gravity wave; and g-modes, internal gravity waves. In particular, p-mode resonance is constrained by the internal sound speed profile and g-modes by the buoyancy frequency (Vallis, 2006; Tassoul, 1980), both of which are dictated by pressure and density stratification.

In turn, this means that the internal structure of the Sun can be determined by the observed resonant frequencies, which lead to the development of some of the earlier standard models of solar structure (Christensen-Dalsgaard et al., 1988). Additional methods were later developed which also revealed the adiabatic index, convective stability, and chemical composition of the solar interior (Asplund et al., 2009). Helioseismology reveals not only the internal structure of the Sun, but also its internal motions. For example, inversion of the frequency splitting from rotation revealed that the differential rotation observed on the surface extends down through the convective zone and transitions to very nearly solid-body rotation beyond the

tachocline and into the radiative zone (Schou et al., 1998). All of these previously mentioned findings are categorized as *global* helioseismology, as they are concerned with the structure of the entire Sun. *Local* helioseismology, on the other hand, studies specific areas and structures in the Sun, mainly through variations in wave travel times and phase shifts.

1.3.1 Local Time-Distance Helioseismology

Local helioseismology can be divided into two main methods, acoustic holography and and time-distance helioseismology. The principle behind acoustic holography is similar to traditional optics, where variations in the surface acoustic wavefield can be attributed to specific perturbations in the interior using Green's functions for wave propagation (Gizon et al., 2018). Such attribution is accomplished by examining either changes in wave phase, as in phase-sensitive holography (Lindsey & Braun, 2000), or in wave amplitude, as in acoustic power holography (Lindsey & Braun, 1997). Time-distance helioseismology, as the name suggests, detects interior perturbations by measuring variations in the travel time of waves as they move from point to point.

Time-distance helioseismology naturally requires that wave travel times can be extracted from stochastic oscillations and that variations in the travel time can be attributed to specific sources. Regarding the first requirement, the cross-correlation function provides an invaluable tool to measure the wave travel time. By cross-correlating the Doppler velocities of two separate points on the solar surface, one may obtain a time-dependent function which is maximized at the travel time between the two points (Rickett & Claerbout, 2000). This cross-correlation maximizing time is the group travel time, relating the propagation time of a given wave packet's envelope. Subsurface perturbations are more easily detected by their corresponding perturbation to the phase travel time, which necessitates the use of some analytical

function with which to fit the observed cross-correlation. It has been shown, such as in Nigam et al. (2007), that the solar cross-correlation function is well-fit by a Gabor wavelet, with the phase travel time as one of the function's parameters.

Attributing the variations in phase travel time to specific perturbations is accomplished through inversions of the travel times based upon either the ray approximation or the Born approximation (Birch et al., 2001). While the Born approximation takes into account the band-limited nature of the solar oscillation signal and is therefore better at resolving small-scale features (Birch & Felder, 2004), the ray approximation is more straight-forward and generally considered more robust (Kosovichev, 2011). An additional tool for isolating the contribution from perturbations at specific depths is phase speed filtering (Gizon & Birch, 2005). As solar acoustic waves travel into the interior, they are reflected back upwards by the sound speed gradient. The specific depth at which these waves reflect, called the turning point, is determined by the spherical harmonic degree l and frequency ω of a given oscillation mode. A more detailed description of turning points is given in Appendix A, however, the relevant point is that oscillations which penetrate to a specific depth can be selected for, which increases the signal-to-noise ratio of helioseismic measurements (Couvidat & Birch, 2006).

1.3.2 Helioseismic Studies of Active Regions and Effects of Magnetic Fields on Travel Times

There exist several helioseismic techniques which have been successful in examining active regions, including the identification of existing active regions on the far-side of the Sun. This far-side imaging has been accomplished using both acoustic holography and time-distance analysis. In the acoustic holography technique, the far-side wavefield is extracted from near-side measurements, and inhomogeneities in the wavefield measured by relative phase-shift can be attributed to the magnetic field's magnitude (Malanushenko et al., 2004; Gizon et al., 2018). In the time-distance

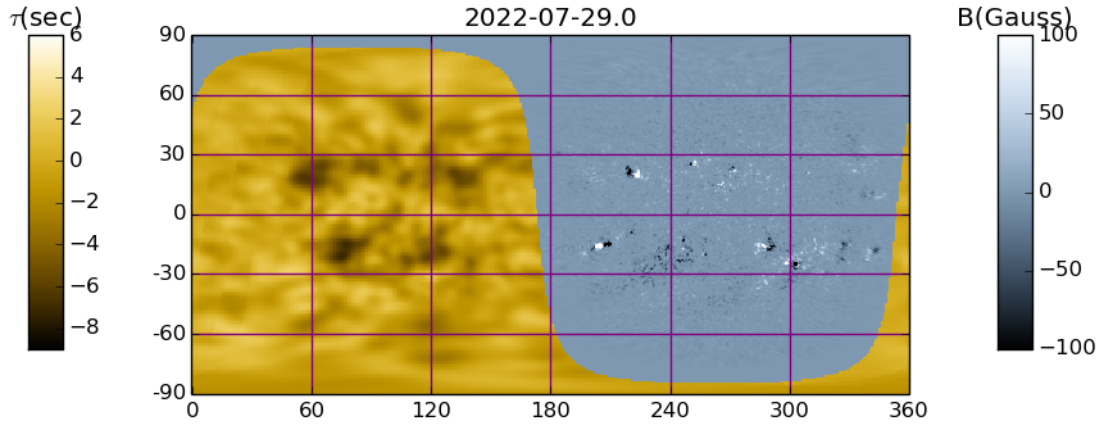

Figure 1.5 Composite map of the full Sun for July 29 2022; the black and white color scale indicates the near-side magnetic field magnitude observed by HMI and the gold and black color scale indicates the far-side travel time shift.
Source: Joint Science Operations Center (2022)

method, shifts in the phase travel time of waves traveling from the near-side to the far-side and back are used to identify far-side active regions (Braun et al., 2010). Applying phase speed filters as well as combining measurement configurations for a so-called multi-skip analysis further increases the signal-to-noise ratio (Hartlep et al., 2008; Zhao, 2007). This far-side imaging has been used to provide a full Sun map of existing active regions, as in Figure 1.5, which is made available every 12 hours by the Joint Science Operations Center (JSOC) (Braun et al., 2010).

While far-side imaging has only been able to identify existing active regions, other efforts have been made to detect emerging active regions. For example, Lindsey & Braun (1997) have detected subsurface flows prior to active regions emergence using acoustic holography. A detailed study of emerging active regions using a similar technique found statistically significant differences in the mean phase travel time of waves penetrating the upper 20 Mm of the convection zone (Birch et al., 2013). Early efforts using time-distance helioseismology have also been able to identify subsurface structures and estimate the emergence rate of an active region observed by the Michelson Doppler Imager (MDI) (Kosovichev et al., 2000, 2001).

Of particular note are the results of Ilonidis et al. (2012) and Ilonidis et al. (2013), which establish a measurement procedure for identification of pre-emergence active regions with a SNR of 4.2-4.9. The authors find significant reductions in the mean travel time of waves one to two days prior to the emergence of several active regions. Additional study of pre-emergence active regions, including some of the regions studied by Kosovichev et al. (2000) and Ilonidis et al. (2013), have found 10-15 second phase travel time perturbations around the eventual location of several active regions at depths of 40 to 75 Mm (Kholikov, 2013). Additional investigation at shallower depths, between 2 and 15 Mm beneath the photosphere, by Toriumi et al. (2013) of an active region studied by Ilonidis et al. (2013) also confirm mean phase travel time reductions preceding the active region's emergence.

One of the mean critiques of these mean travel time analyses, however, is the large difference between the 10 to 15 second variations which were measured and the theoretical effect of the magnetic field in the convection zone, which should produce immeasurably small variations in the travel time (Braun, 2012). A recent study by Felipe et al. (2016) may provide an alternative explanation, where the authors perform MHD simulations to develop a realistic sunspot. The authors then initiate two simulations, one with the previous sunspot's thermal profile with zero magnetic field, and another with the previous sunspot's magnetic field but with a quiet sun thermal profile, with the goal of identifying the individual contribution of thermal and magnetic effects. While the magnetic-only sunspot produces weak mean travel time shifts, those from the thermal simulation are both stronger and more persistent with depth. Furthermore, the thermal variations should decrease the wave speed and lengthen the travel time, but strong reductions in the travel time are measured instead. The authors show that this can be explained by considering the corresponding change in the cut-off frequency, which would shorten the travel time in agreement with Moradi et al. (2009). It may be possible that similar thermal effects

originating from the concentration of rising magnetic flux can lead to the observed pre-emergence travel time variations.

A full understanding of the magnetic field's effect on helioseismic measurements remains difficult to achieve. While significant progress has been made in assessing some aspects of the subsurface structure of active regions, for example their surrounding flows (Jain et al., 2012; Braun, 2016) and associated sound speed variations (Zhao & Kosovichev, 2003), there has yet to be a successful direct assessment of an active region's subsurface magnetic field. In theory, at least, the basis for such assessment has been laid; namely, the conversion of purely acoustic waves into fast magnetoacoustic waves in the presence of strong magnetic fields. Cally (2005) find significant conversion from acoustic to fast magnetoacoustic at the equipartition surface—where the sound and Aflvèn speeds are equal—for vertical magnetic fields. It has also been found that horizontal magnetic fields produce a phase speed-dependent perturbation to acoustic travel times in the ray path approximation (Jain, 2007). Furthermore, numerical simulations show that the fast magnetoacoustic mode displays resonant characteristics, such that it is reflected slightly above the equipartition surface and remains trapped beneath the chromosphere (Khomenko & Collados, 2006).

1.3.3 Sunquakes

Regarding the dynamical processes associated with existing active regions, it is commonly accepted that solar flares result from the reconfiguration of the coronal magnetic field towards a lower-energy state (Aschwanden, 2019; Ulyanov et al., 2019). While seemingly unrelated to other helioseismic studies, the distribution of the energy released in solar flares from coronal heights to regions lower in the atmosphere gives rise to impulsive seismic events which can be observed in the photosphere. Such events, known as sunquakes, are easily seen in observations and were first detected by the characteristic expanding ripples in MDI Dopplergrams (Kosovichev & Zharkova,

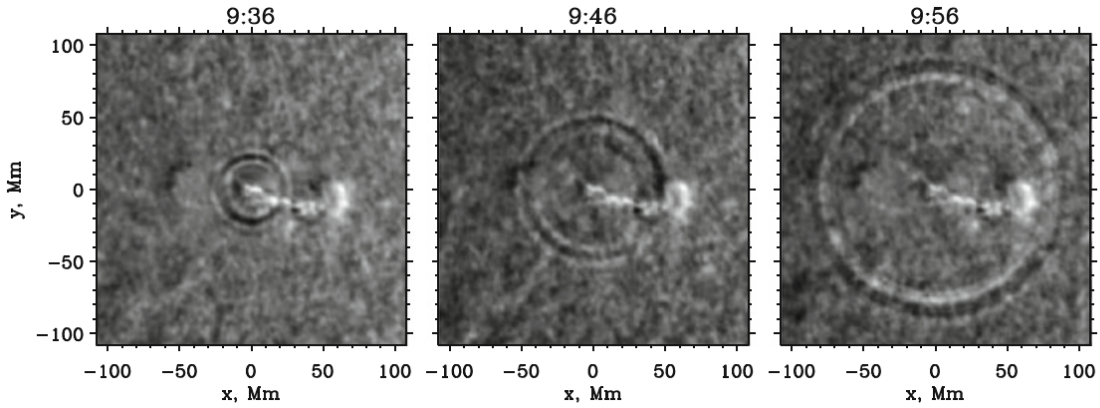

Figure 1.6 Time series of the sunquake following the solar flare of 1996 July 9. The sunquake wavefront has been amplified by a factor of four to be discerned from the background.
Source: Kosovichev (2011)

1998; Kosovichev, 2006), as in Figure 1.6. The mechanism by which these sunquakes are excited, however, has yet to be definitively identified.

Electron beams accelerated by magnetic reconnection have been suggested as a possible means of exciting sunquakes (Sharykin et al., 2017; Macrae et al., 2018; Pedram & Matthews, 2012). In particular, the thick-target model (e.g., Fisher et al., 1985) suggest that the electron beam strikes a stationary chromosphere, and the energy released by the electrons as they thermalize can be observed as a strong increase in hard X-ray (HXR) emission. Additionally, past studies of sunquakes have identified the photosphere or lower chromosphere as possible locations where sunquakes are excited Kosovichev & Zharkova (1995); Zharkova & Zharkov (2015); Sharykin et al. (2017); Chen (2019). It appears that heating in these regions, and the shocks produced by this heating, may provide enough energy to excite the observed acoustic waves (Kosovichev, 2015; Kosovichev & Zharkova, 1995).

Other beams aside from purely electron-based, such as proton or mixed-particle beams, also have the potential to provide the heating necessary to excite sunquakes. For example, Zharkova & Zharkov (2015) find that proton beams—which deposit significantly more momentum than electron beams—may penetrate up to 300 km

beneath the photosphere. Additional modeling has shown that the proton beams are more efficient at exciting sunquakes, and the temporal coincidence of high-energy emission and sunquake excitation in some events suggests a mixed electron-proton beam as a seismic source (Zharkova & Zharkov, 2007). Further studies reinforce the importance of the coincidence between HXR emission and sunquake excitation, and that the momentum flux required to compress the photosphere is more likely to originate from a proton-heated atmosphere, as opposed to electron-heated (Donea & Lindsey, 2005).

1.4 Dissertation Outline

In this dissertation, we present a comprehensive helioseismic analysis of active regions beginning with their pre-emergence properties up to their appearance on the solar surface and their associated dynamic processes. The structure of this dissertation is as follows.

Chapter 2 begins with a discussion on some of the finer details of phase speed filtering and how this is used to isolate oscillations in the upper convection zone. We apply our methodology to two simulations of subsurface sound speed perturbations, as a model for rising magnetic flux, and examine the evolution of phase travel time deviations for several active regions. Additionally, we present an idealized model for flux emergence and use this to evaluate the time delay between surface magnetic fields and mean phase travel time perturbations. We also discuss possible correlations with the surface properties of the active regions studied in the time-delay analysis.

In Chapter 3, we derive a novel technique for the assessment of subsurface magnetic fields. In particular, we show that the orientation of the horizontal magnetic field as well as a proxy for its magnitude can be determined from spatial anisotropies in mean phase travel time deviations. We validate this technique using a simulation of acoustic waves propagating in a plasma with uniform background magnetic field and

perform more comprehensive tests using a realistic simulation of a sunspot. Finally, we apply the technique to several active regions observed by HMI and compare the properties of the subsurface field with the surface counterparts.

Chapter 4 includes a derivation of the equations describing solar oscillations as linear perturbations which is used to construct a hydrodynamic simulation of sunquake excitation. We discuss the use of wavenumber damping and how the relevant parameters can be obtained from solar observations. The simulations are used in conjunction with HMI observations to provide estimates for the energy release and excitation height of several sunquake events in the context of both a time-dependent and instantaneous source function. We then move to more realistic mechanisms of sunquake excitation, using heating rates derived from RADYN simulations (Allred et al., 2020) of proton beams with varying low-energy cutoffs.

Chapter 5 summarizes the results of the previous chapters and discussion of what these results imply. We also discuss potential extensions of this thesis' results to future work, including the develop of new inversion of subsurface magnetic fields and improvements to sunquake simulations.

Appendix A describes the procedure for computing the theoretical helioseismic measurements presented in Chapters 2 and 3, as well as how oscillations penetrating to a desired depth can be identified from the acoustic dispersion relation.

Appendix B derives the central difference approximation to the first radial derivative on a non-uniform mesh, which is used in our simulations in Chapter 4.

CHAPTER 2

EARLY DETECTION OF EMERGING ACTIVE REGIONS

2.1 Data and Methods

For all active regions studied in this section, the Dopplergrams cover an area of 30.72 by 30.72 heliographic degrees with a spatial resolution of 0.12 degrees per pixel. While higher resolution data is available for Helioseismic and Magnetic Imager (HMI) data from the Solar Dynamics Observatory, the increased number of pixels leads to longer computation times without significant increases in the signal-to-noise ratio of the resulting measurements. The data obtained from the Michelson Doppler Imager (MDI) aboard the Solar and Heliospheric Observatory (SOHO) for NOAA ARs 07978 and 10488 have a cadence of 60 seconds, with 480 frames per eight-hour segment. The HMI Dopplergrams have a cadence of 45 seconds for a total for 640 frames in an 8-hour segment. The eight-hour segments are spaced closely together near the emergence time, with four hours separating the mid-times, and farther apart at other times with eight-hours separating the mid-times. Both of the HMI and MDI Dopplergrams are tracked at the Carrington rotation rate and remapped to a Postel's projection for the following helioseismic analysis. The data from the 3D hydrodynamic simulation developed by Hartlep et al. (2011), referred to here as Acoustic Model 1, has a spatial resolution of 0.7 degrees per pixel and 60-second cadence; the spatial resolution and cadence of the data from the 3D acoustic model developed by Stejko et al. (2021), referred to here as Acoustic Model 2, is identical to MDI Dopplergrams.

2.1.1 Selection of Active Regions for Statistical Analysis

To select the active regions to be used in our larger-scale analysis, we first search the NOAA Solar Region Summaries catalog for sunspots which eventually reach a maximum size of 150 millionths of disk area or greater, and which appear between

April 2011 and November 2020. This list is refined further by selecting the associated active regions which are first identified within 45 degrees of disk center. This excludes active regions whose pre-emergence coordinates would lead to distortions in the corresponding Dopplergrams from foreshortening. The Dopplergrams and Magnetograms of the resulting 91 active regions are obtained for the 96-hour time period beginning 72 hours before the respective emergence times. These time series are tracked and remapped to a Postel's projection with 0.12 degrees per pixel spatial resolution, and 45-second cadence for the Dopplergrams and 12-minute cadence for the Magnetograms. Finally, we examine the Dopplergrams and Magnetograms for any artifacts which may interfere with processing, including anomalous pixels and missing frames, where we find that the 20 of the initial 91 active region Dopplergram series were unsuitable for analysis. The remaining 71 time series are divided into eight-hour segments in increments of four hours, and the results of the first 46 active regions are presented in this work.

2.1.2 Phase-Speed Filtering

We next treat the data with two Fourier filters; the first filter (F_1) is a step-function in frequency which preserves oscillations only in the 2 to 5 mHz range, which is the resonant portion of the solar acoustic power spectrum. The second filter (F_2)is similar, though here we filter over phase speed $v_{\rm ph} = \omega/k$, with the parameters selected such that oscillations with turning points between 40 and 70 Mm beneath the photosphere are isolated. As discussed in Section 1.3 and Appendix A, the phase speed of a given oscillation mode is equal to the local sound speed at the corresponding turning point. Here, we use the Standard Solar Model (Christensen-Dalsgaard et al., 1996) to determine the sound speed at $z = -40$ Mm ($v_{\rm ph,1} = 92$ km s^{-1}) and at $z = -70$ Mm ($v_{\rm ph,2} = 127$ km s^{-1}). Oscillations which have phase speed less than $v_{\rm ph,1}$ are treated with a Gaussian filter centered at $v_{\rm ph,1}$ with width $\delta v = 8.7$ km s^{-1}, and oscillations

with phase speed greater than $v_{\mathrm{ph},2}$ receive a similar treatment. Oscillations with phase speed between $v_{\mathrm{ph},1}$ and $v_{\mathrm{ph},2}$ are unaffected. In other words, F_1 is given by

$$F_1(\nu) = \begin{cases} 1 & 2\mathrm{mHz} \leq \nu \leq 5\mathrm{mHz} \\ 0 & \text{otherwise} \end{cases} , \tag{2.1}$$

and F_2 by

$$F_2(v_{\mathrm{ph}}) = \begin{cases} \exp\left[-\dfrac{(v_{\mathrm{ph}} - v_{\mathrm{ph},1})^2}{2\delta v^2}\right] & v_{\mathrm{ph}} < v_{\mathrm{ph},1} \\ 1 & v_{\mathrm{ph},1} \leq v_{\mathrm{ph}} \leq v_{\mathrm{ph},2} \\ \exp\left[-\dfrac{(v_{\mathrm{ph}} - v_{\mathrm{ph},2})^2}{2\delta v^2}\right] & v_{\mathrm{ph},2} < v_{\mathrm{ph}} \end{cases} . \tag{2.2}$$

A typical acoustic power spectrum, along with the bounds of the Fourier filters, are shown in Figure 2.1.

2.1.3 Computing Cross-Correlations and Travel Time Deviations

After filtering the data to isolate oscillations with the desired turning points, we compute the cross-correlations as described in Duvall et al. (1993) with the following procedure. The spherical coordinates for each pixel within the tracked Dopplergram series are determined using the heliographic coordinates of the central pixel in the image, and concentric rings about a given pixel are identified which have radii equal to half the horizontal travel distance of the desired oscillations. The radius of the smallest ring, or annulus, is 4.56 heliographic degrees, which corresponds to the oscillations with the turning point at $z = -40$ Mm. Additional annuli are identified in increasing radius with increment 0.12 degrees up to the largest annulus with radius

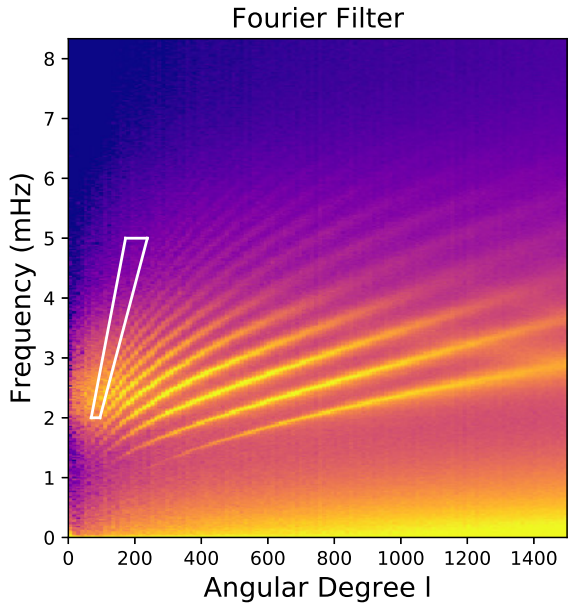

Figure 2.1 Acoustic power spectrum derived from an eight-hour Dopplergram series. The bounds of the step-function filter (F_1) are depicted by the horizontal white lines at 2 and 5 mHz. The bounds of the phase-speed filter (F_2) are depicted by the diagonal white lines. Oscillations within this bounding box are unaffected.
Source: Stefan et al. (2021)

8.16 degrees for the turning point at $z = -70$ Mm. We also consider five different configurations for averaging the Dopplergram signal where the annulus is divided into an increasing number of opposing arc segments, beginning with three opposing pairs up to seven opposing pairs. The Dopplergram signal is averaged within each arc for the point-to-point cross-correlation with the similarly averaged opposing arc, for a give turning point depth, spatial position, and arc configuration. Figure 2.2 shows an example of the measurement scheme for the case of five arc pairs.

The point-to-point cross-correlations are computed separately for the positive and negative phase travel times. For an arc labeled A correlated with the opposing arc labeled B, the positive phase travel time is associated with oscillations traveling from A to B and the negative phase travel time with oscillations traveling from B to A. The choice of reference arc is, of course, arbitrary and in our case, we are most

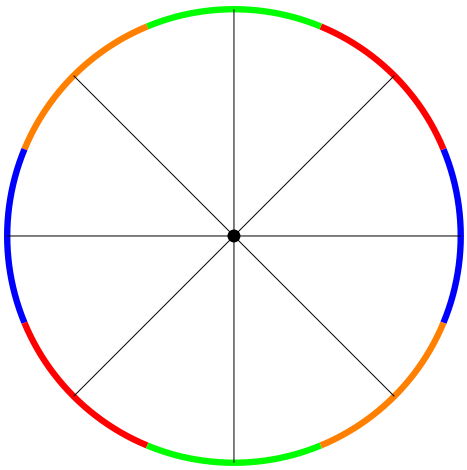

Figure 2.2 Example of a spatial averaging scheme used to measure phase travel times for the case of eight arc segments. Dopplergram signal within each arc is averaged and cross-correlated with the opposing arc.
Source: Stefan & Kosovichev (2022)

interested in the average of these phase travel times as described in the following section. The cross-correlations are given by

$$\Psi_{A\to B}(\tau) = \frac{1}{T}\int_0^T v_A(t)v_B(t-\tau)dt \tag{2.3}$$

and

$$\Psi_{B\to A}(\tau) = \frac{1}{T}\int_0^T v_A(t)v_B(t+\tau)dt, \tag{2.4}$$

where T is the duration of the Dopplergram time series, v_A is the Dopplergram signal of arc A, v_B is the Dopplergram signal for arc B, and τ is the time lag between the two signals.

The phase travel times can be extracted from the cross-correlations using several methods, though here we use Gabor wavelet fitting (Nigam et al., 2007) and the error-minimization method developed by Gizon & Birch (2002), which we refer to as the GB02 method. For the first method, the cross-correlations are fit to a Gabor wavelet of the form

$$\Psi(\tau) = A\cos\left(\omega_0(\tau - \tau_{\rm ph})\right)\exp\left[-\frac{1}{2}\gamma^2(\tau - \tau_{\rm g})^2\right], \tag{2.5}$$

where τ is the time lag, A is the amplitude, ω_0 is the angular frequency of a given mode, $\tau_{\rm ph}$ and $\tau_{\rm g}$ are the corresponding phase and group travel times respectively, and γ is related to the width of the wavepacket's Gaussian envelope. To supply an initial guess of the parameters for the curve-fitting algorithm, we fit the spatially averaged cross-correlation for each annulus radius and arc number using the travel times and frequency derived from ray theory (Gough, 1993). The resulting radius-dependent phase travel times are used as a reference to shift the pixel-by-pixel cross-correlations in time so that they can be averaged over arc radius. The averaged cross-correlations are then used to obtain a phase travel time deviation map for each arc segment case from a final Gabor wavelet fit.

The procedure for the GB02 method begins similarly, by obtaining reference phase travel times from the spatially-averaged Gabor wavelet fit to shift and average the pixel-by-pixel cross-correlations. However, we also define a reference cross-correlation, $C_{\rm ref}$, for the entire region by further averaging over the number of arc segments. We then define $X_{\pm}(\Psi, t)$, the squared error between the reference cross-correlation and a given pixel's cross-correlation $\Psi(x, y, n)$ for spatial position

(x, y) and number of arc segments n. This function is given by

$$X_{\pm}(\Psi, \tau) = \int_{-\infty}^{\infty} \left[\Psi(x, y, \tau') - C_{\mathrm{ref}}(\tau' \mp \tau)\right]^2 f(\pm\tau') d\tau', \tag{2.6}$$

where $f(\mp\tau)$ is a window function which isolates the positive or negative time lags. This function is defined to be unity for $|\tau_{\mathrm{ph}} - \tau_{\mathrm{ph,ref}}| \leq 5$ minutes and zero otherwise. The travel time deviations can be derived from the above function, where the backward travel time deviation $\delta\tau_{-}$ is given by the lag τ which minimizes the error function $X_{-}(\Psi, \tau)$ and similarly for the forward travel time deviation $\delta\tau_{+}$ and the error function $X_{+}(\Psi, \tau)$.

It can be shown—as in (Kosovichev & Duvall, 1997)—that the expected first order perturbation to the expected mean phase travel time deviation due to a change in the sound speed along the ray path is

$$\delta\tau_{\mathrm{mean}} = \int_{\Gamma} \frac{\delta c}{c} S ds, \tag{2.7}$$

where $\delta\tau_{\mathrm{mean}}$ is the mean phase travel time deviation, Γ is the unperturbed acoustic ray path, δc is the perturbation to the background sound speed c, $S = k/\omega$ is the phase slowness, and ds is the differential of the ray path. The mean phase travel time deviation, $\delta\tau_{\mathrm{mean}}$ is computed from the simple average of the forward and backward travel time deviations, derived directly in the GB02 method and computed in the Gabor wavelet method as $\delta\tau_{\mathrm{ph},\pm} = \tau_{\mathrm{ph},\pm} - \langle\tau_{\mathrm{ph},\pm}\rangle_{x,y}$.

2.2 Testing on Numerical Simulations: Acoustic Model 1

We first test the above time-distance method on simulated Dopplergram data from Model 1 (Hartlep et al., 2011), which contains two 5% reductions in sound speed of differing horizontal extent. Both perturbations have the following dependence on depth (z) and angular distance from the respective perturbation's center (α),

$$\delta c = \frac{A}{4}\left(1+\cos\left(\pi\frac{z-z_0}{\delta z}\right)\right)\left(1+\cos\left(\pi\frac{\alpha}{\delta\alpha}\right)\right). \tag{2.8}$$

The smaller perturbation has a horizontal width $2\delta\alpha = 180$ Mm and the larger perturbation has a horizontal width $2\delta\alpha = 360$ Mm; both perturbations are placed 50 Mm (z_0) beneath the model's surface with vertical radius $\delta z = 20$ Mm. While these perturbations, particularly the larger one, are significantly wider than is expected of an emerging concentration of magnetic flux, they provide some context on the maximum detectability of sound speed perturbations near the center of our vertical region of interest.

The large perturbation (Figure 2.3a) is very well-resolved, with strong mean travel time perturbations extending up to 100 Mm from the center of the perturbation. This strongly perturbed region, along with the entire map, is modulated by the inherent realization noise associated with helioseismic measurements. The smaller perturbation (Figure 2.3b) is distinguishable from the background, but the circular horizontal shape is less clear than for the large perturbation. Furthermore, the maximum travel time deviation at the center of the small perturbation is smaller than the maximum of the large perturbation, ≈ 29 s compared to ≈ 38 s. This difference is expected as less of a given oscillation's ray path travels through a perturbed region which reduces the overall shift in the phase travel time.

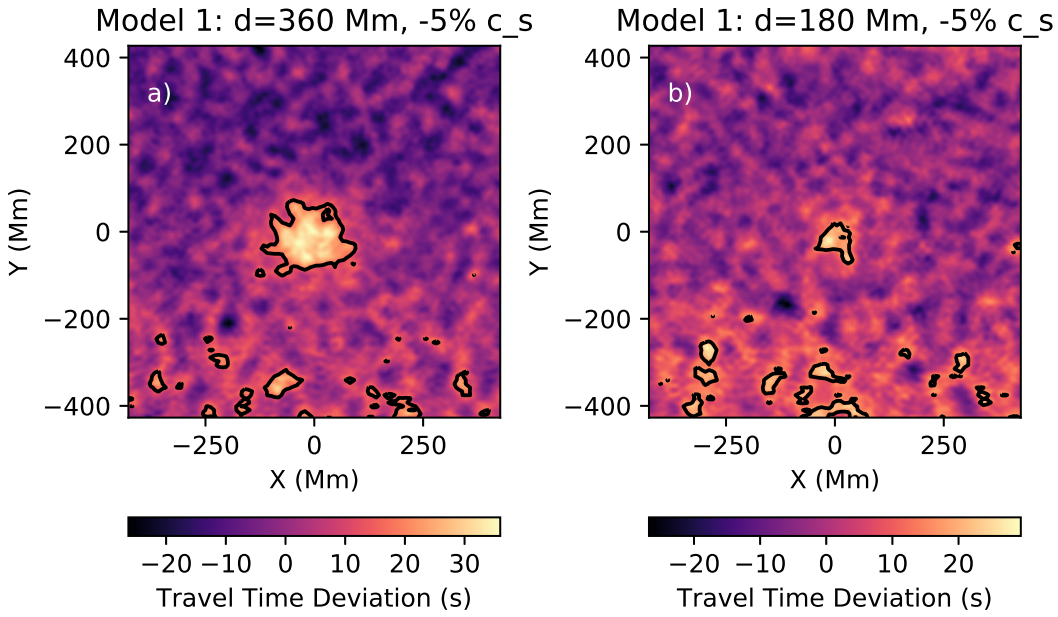

Figure 2.3 Measurements of phase travel time deviation for the sound speed perturbations in Acoustic Model 1. a) Mean phase travel time deviation map of the perturbation with horizontal width $2\delta\alpha = 360$ Mm; b) Mean phase travel time deviation map of the perturbation with horizontal width $2\delta\alpha = 180$ Mm. The solid black line marks the $2\sigma = 8.20$ threshold derived from the unperturbed regions of the model.
Source: Stefan et al. (2021)

To highlight significantly perturbed regions, we determine a 2σ threshold of 8.20 seconds and overlay this contour in Figures 2.3a and 2.3b, marked by the black line. The standard deviation is obtained from the mean phase travel deviations after those within 200 Mm of the map center for both the large and small perturbations. The shape of the contour differs in both cases from the prescribed horizontal circular symmetry, and this difference is more significant for the smaller sound speed which has a maximum travel time deviation closer to the background variation. This indicates that the overall shape of detected features may not necessarily coincide with *in-situ*

conditions, though the difference in the magnitudes of the measured mean travel time deviations are consistent with the size and strength of the sound speed perturbations. The 2σ contouring also reveals some anomalous travel time deviations in the lower portions of Figures 2.3a and 2.3b, which are not observed in Acoustic Model 2 in the following section. While there certainly may be some pixels not associated with the sound speed perturbations that exceed the threshold, both figures clearly show a latitudinal dependence as opposed to a random distribution. The background mesh of Acoustic Model 2 is uniform in latitude and it is suspected that these anomalies arise from the changing spatial resolution near the model's poles.

2.3 Testing on Numerical Simulations: Acoustic Model 2

Using Acoustic Model 2 (Stejko et al., 2021), we test both the sensitivity dependence on perturbation width and depth, as well as the accuracy of travel time measurements made with our time-distance method. We consider six variations of sound speed perturbations, the results of which are shown in Figure 2.4. For all perturbations, the vertical radius is equal to 20 Mm, while the left column contains perturbations with horizontal radius 50 Mm and the right column with horizontal radius of 20 Mm. The depth of the perturbations increases in descending order, with $z_0 = -40$, $z_0 = -50$, and $z_0 = -60$ Mm. The perturbations are Gaussian in all directions with amplitude equal to 5% of the background sound speed. As with Acoustic Model 1, we use the standard deviation of unperturbed regions highlight the strongly perturbed regions in the mean phase travel time maps using a $2\sigma = 9.58$ s threshold. However, the field of view is small enough in this case to necessitate the use of additional simulations lacking a sound speed perturbation, shown in Figure 2.5, to compute this threshold.

There is a surprising lack of spatial information in Figure 2.4, where one would expect circular mean phase travel time shifts given the Gaussian nature of the sound speed perturbations in the (x,y)-plane. Instead, we find that the spatial structure of

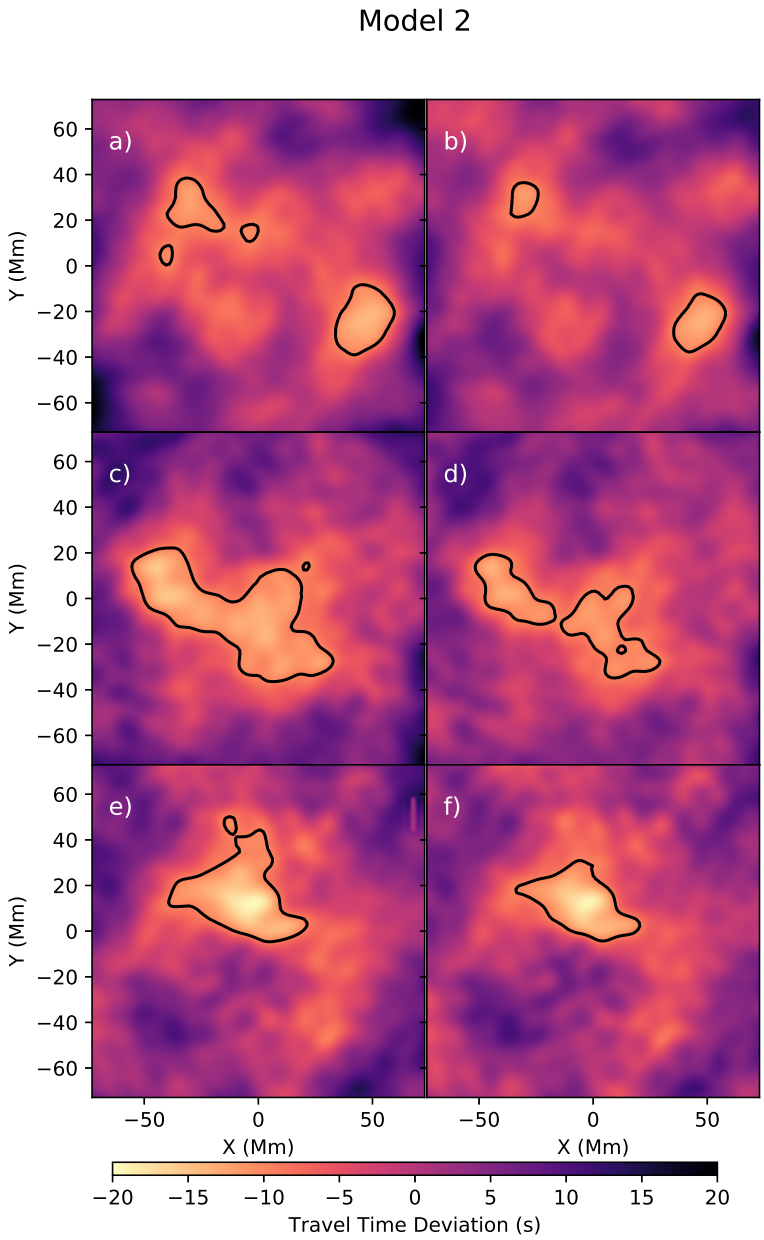

Figure 2.4 Travel time shifts measured in Acoustic Model 2 from a 5% increase in sound speed with a vertical radius of 20 Mm, at a depth of 40 Mm (a,b), 50 Mm (c,d), and 60 Mm (e,f). The horizontal radius is 50 Mm for (a,c,e) and 20 Mm for (b,d,f). The solid black line denotes the 2σ threshold of 9.58 seconds derived from empty model runs.

Source: Stefan et al. (2021)

the sound speed perturbations is convolved with the background noise and added to the underlying inhomogeneities. This is particularly true for the $z_0 = -40$ Mm perturbation, located at the upper range of our sampled region such that the entire perturbation is not within our vertical field of view. Additionally, we see little variation in the shape of the 2σ contours between the 20 Mm and 50 Mm perturbation for depths $z_0 = -50$ Mm and $z_0 = -60$ Mm. Some similarity is expected as the oscillation excitation functions of Acoustic Model 2 are the same for each case, however, the only distinguishing features between the two width cases are a slight increase in the maximum mean phase travel time deviation as well as a small increase in the area encircled by the 2σ contour. The increase in the maximum's magnitude between the 20 Mm and 50 Mm wide perturbations, around two to three seconds, is similar to that seen in Acoustic Model 1. Likewise, there is an increase of around eight seconds from the $z_0 = -40$ Mm and $z_0 = -60$ Mm cases; since the sound speed perturbation is proportional to the local sound speed which increases with depth, we should similarly expect the mean phase travel time deviation to increase as well.

Further testing is done with Acoustic Model 2 to asses the accuracy of the travel time measurements, where a 5% Gaussian sound speed reduction is placed 55 Mm beneath the model's surface and with radius 20 Mm in all directions. The expected travel time shift is computed using Equation (2.7), the Standard Solar Model (Christensen-Dalsgaard et al., 1996) as the background mesh, and the previously described parameters for the perturbed sound speed. The procedure for computing the expected travel time perturbation is described in Appendix A. The mean phase travel time deviations are sampled with the same method as in Acoustic Model 1, though only one ray is sampled per arc pair. We expect there to be no difference with the inclusion of additional rays as the sound speed perturbation is circularly symmetric. As with the actual measurements of the perturbation, the predicted map has the mean phase travel time subtracted to obtain the deviations. The measured

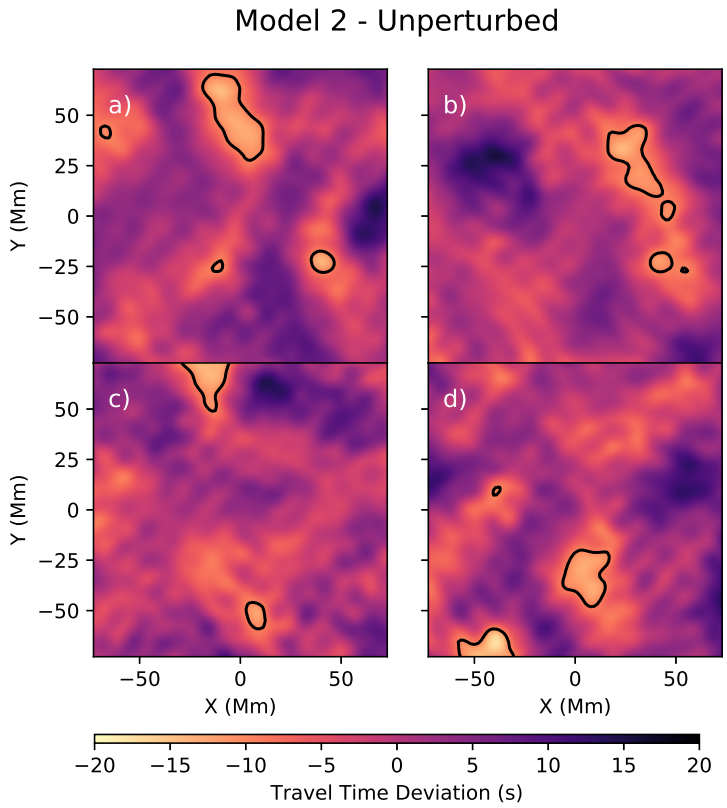

Figure 2.5 Travel time shifts measured in Acoustic Model 2 for the unperturbed case. These maps are used to determine the 2σ threshold (shown here by the black contours) of Figures 2.4 and 2.6.
Source: Stefan et al. (2021)

area of the perturbation in Figure 2.6 is roughly the same as what is predicted, however the 2σ-contoured region is strongly convolved with the background noise such that area is no longer entirely circular. Additionally, the maximum of the measured mean phase travel deviations is several seconds shorter than the predicted maximum. While the noise level—around 4.8 seconds—can explain this discrepancy, we observe far more reductions in the travel time magnitude than increases relative to the predicted deviation.

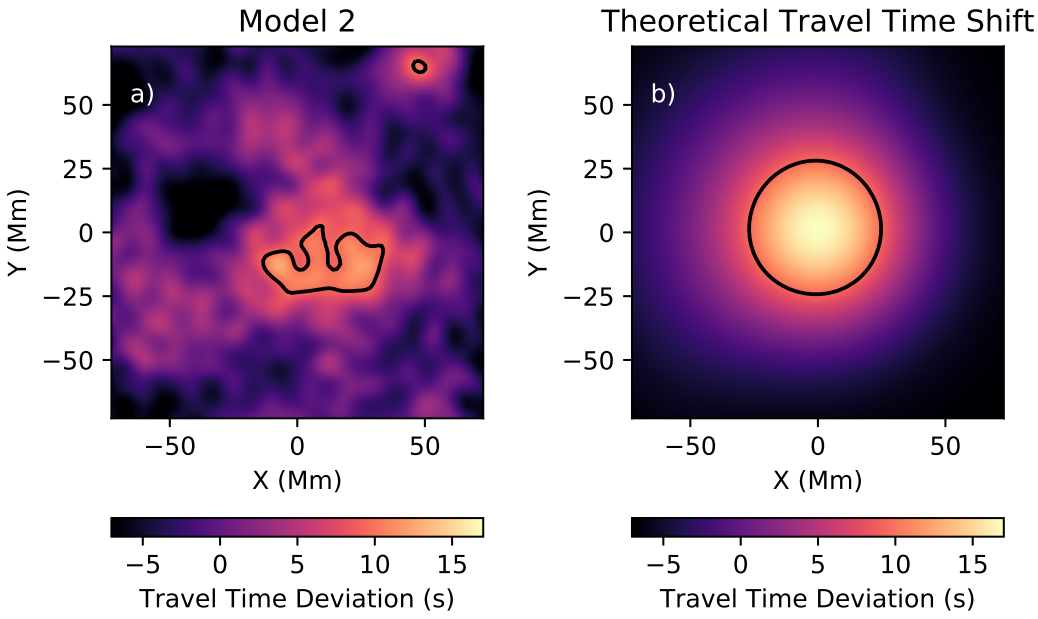

Figure 2.6 Comparison between the measured (a) and theoretical (b) travel time shifts for a 5% reduction in sound speed. The scale is adjusted to align with the maximum and minimum of the theoretical travel time shifts. The solid black line denotes the 2σ threshold of 9.58 seconds derived from empty model runs.
Source: Stefan et al. (2021)

2.4 Case Study of Select Active Regions and Comparison with Quiet Sun Measurements

In this section, we apply our time-distance method to five active regions using Dopplergrams obtained from HMI and MDI. Here, the travel time deviations are computed only with the Gabor wavelet fitting procedure. We begin with NOAA ARs 07978 and 10488 which were previously studied by Ilonidis et al. (2011), who measured strong travel time shifts several hours prior to the flux emergence. To provide a quantitative measure of the strength and significance of mean phase travel time shifts, we define the perturbation index in a fashion similar to Ilonidis et al. (2011). We take the perturbation index to be the sum of negative travel time shifts having amplitude greater than twice the standard deviation of the entire time series, multiplied by the area occupied by these travel time deviations. For example, a region of area 50 Mm^2 having a travel time deviation of -10 seconds will have a perturbation index of 500 s Mm^2. The perturbation index will therefore increase if either the magnitude of the travel time deviation or the occupied area increases.

With this in mind, we find that AR 10488 has a small increase in the perturbation index 25 hours prior to emergence, and a stronger increase which occurs five hours before the magnetic flux emerges, as shown in Figure 2.7a. Additionally, there is a large peak in the perturbation index 24 hours after the active region emerges. Extended observations by Ilonidis et al. (2011) show that the magnetic flux rate decreases one day after emergence before abruptly increasing, and we interpret this secondary peak as additional magnetic flux. We also see a strong peak in the perturbation index of AR 07978 (Figure 2.8a) 20 hours before its emergence, though the background perturbation index is slightly more noisy than that of AR 10488. The active regions magnetic flux increases slowly for about 15 hours after emergence followed by a strong increase in the flux in the remaining 15 hours of observation. We

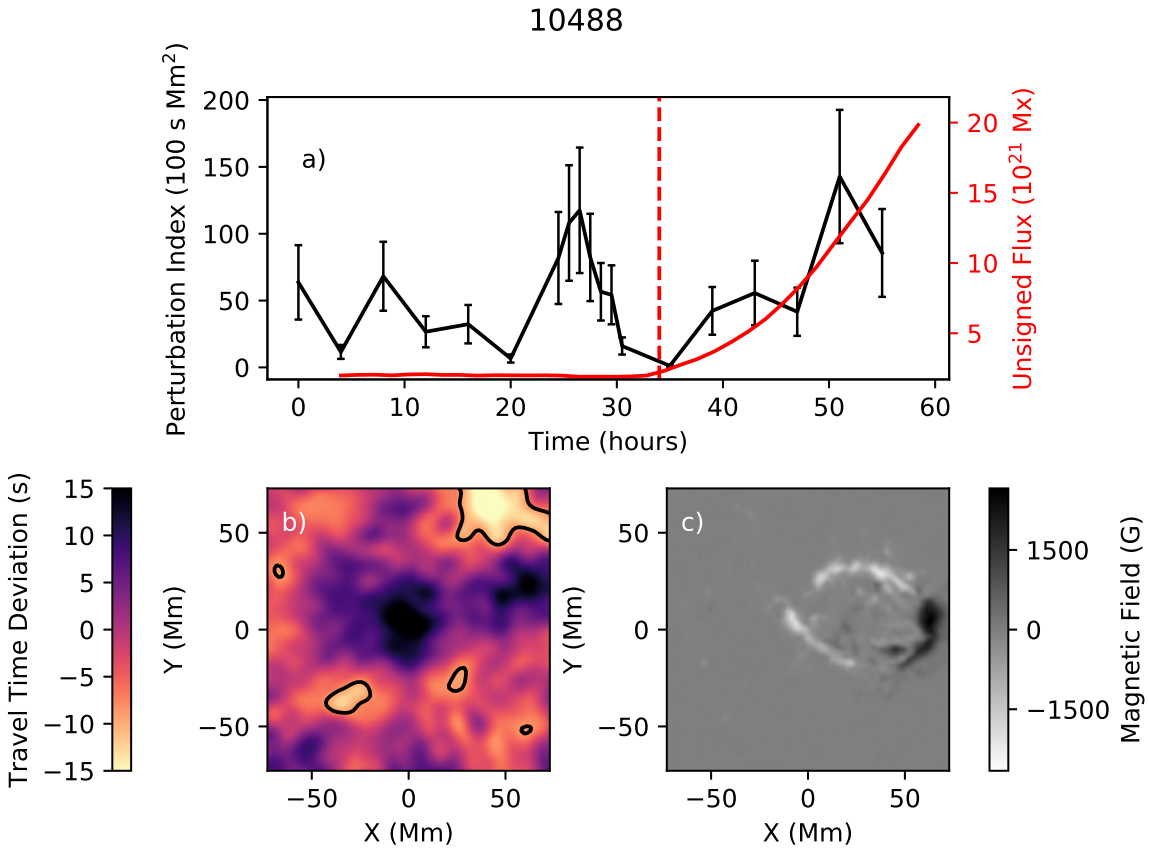

Figure 2.7 Analysis of AR 10488. a) Perturbation index over time (black) and the unsigned magnetic flux (red) where the vertical red dashed line indicates the approximate time of emergence; b) Travel time map at the time of peak perturbation index where the regions which meet the 2σ threshold are bounded by the solid dashed line; and c) Magnetogram of the active region at the end of the data series.
Source: Stefan et al. (2021)

observe a moderate peak near the emergence time which precedes this change in the flux rate by around 14 hours.

In contrast to ARs 07978 and 10488, AR 12772 is a relatively weak active region where the unsigned magnetic flux remains below 850 Gauss during our observations. We are, however, able to detect a peak in the perturbation index 20 hours prior to the active region's emergence, as seen in Figure 2.9a. AR 11158 is an active region of moderate strength, where the magnetic field does exceed 1000 Gauss by the end of our observations. Furthermore, the structure of the active region is significantly

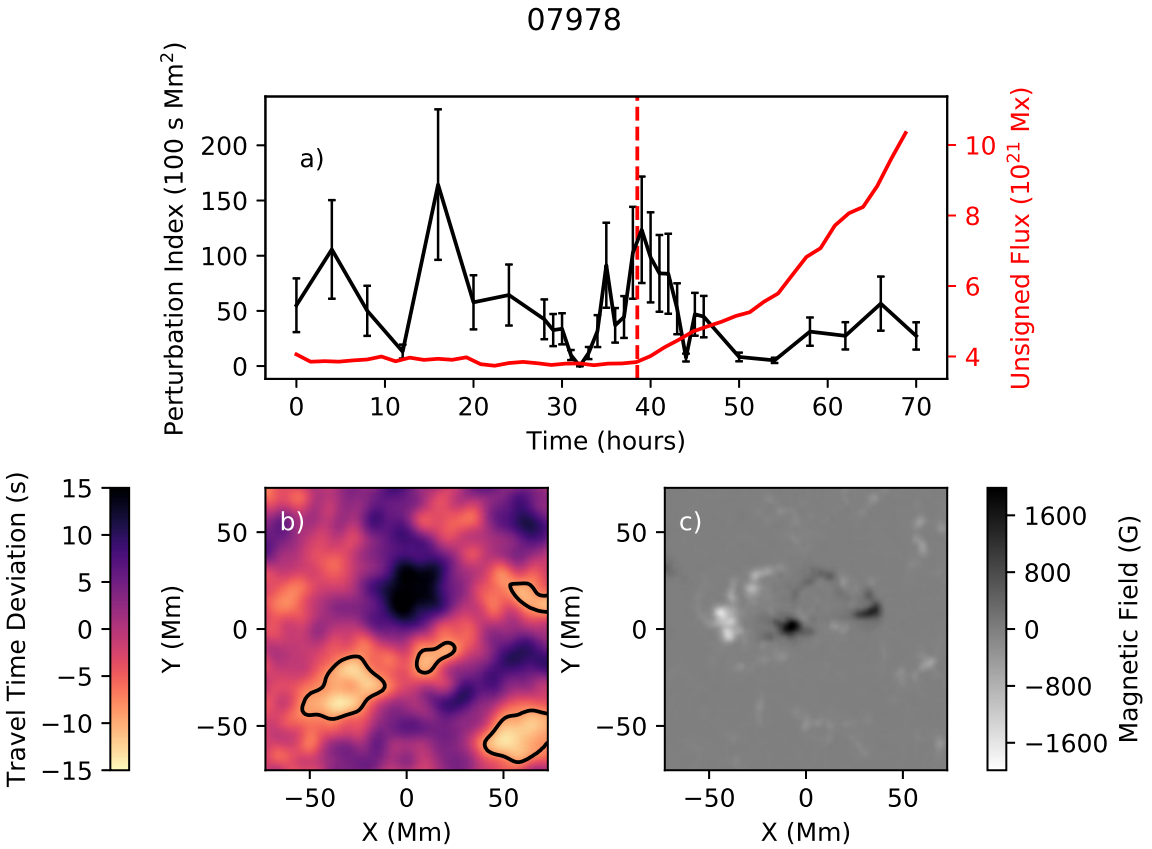

Figure 2.8 Analysis of AR 07978. a) Perturbation index over time (black) and the unsigned magnetic flux (red) where the vertical red dashed line indicates the approximate time of emergence; b) Travel time map at the time of peak perturbation index where the regions which meet the 2σ threshold are bounded by the solid dashed line; and c) Magnetogram of the active region at the end of the data series.
Source: Stefan et al. (2021)

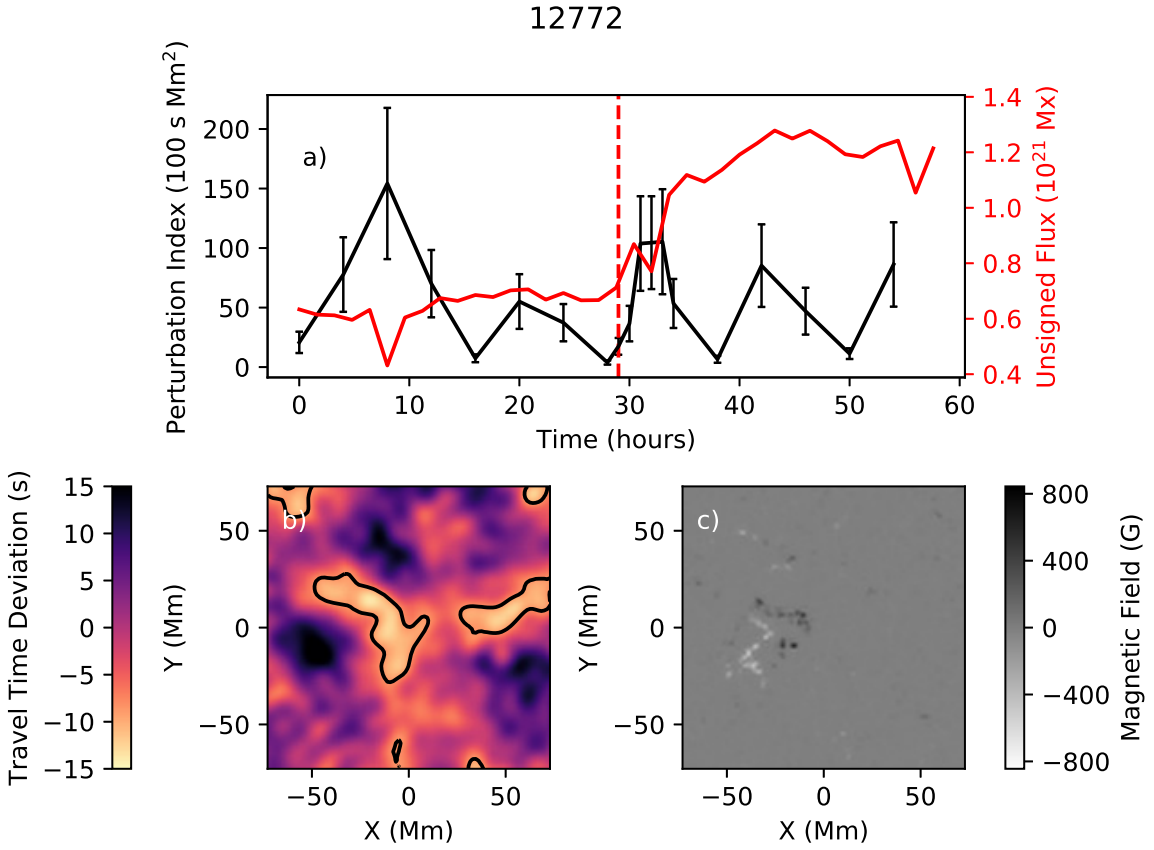

Figure 2.9 Analysis of AR 12772. a) Perturbation index over time (black) and the unsigned magnetic flux (red) where the vertical red dashed line indicates the approximate time of emergence; b) Travel time map at the time of peak perturbation index where the regions which meet the 2σ threshold are bounded by the solid dashed line; and c) Magnetogram of the active region at the end of the data series.
Source: Stefan et al. (2021)

more bipolar than AR 12772. For AR 11158 we observe a more gradual rise in the perturbation index (Figure 2.10a) beginning around 25 hours before the flux emerges, with some smaller changes in the perturbation index following emergence which appear to precede abrupt changes in the unsigned magnetic flux.

Whereas we observe gradual increases in the perturbation index of active regions, the perturbation index of quiet Sun regions (Figure 2.11) shows more abrupt changes as expected of background noise. While there is a rapid increase in the perturbation index of the quiet Sun region located at latitude +15° followed

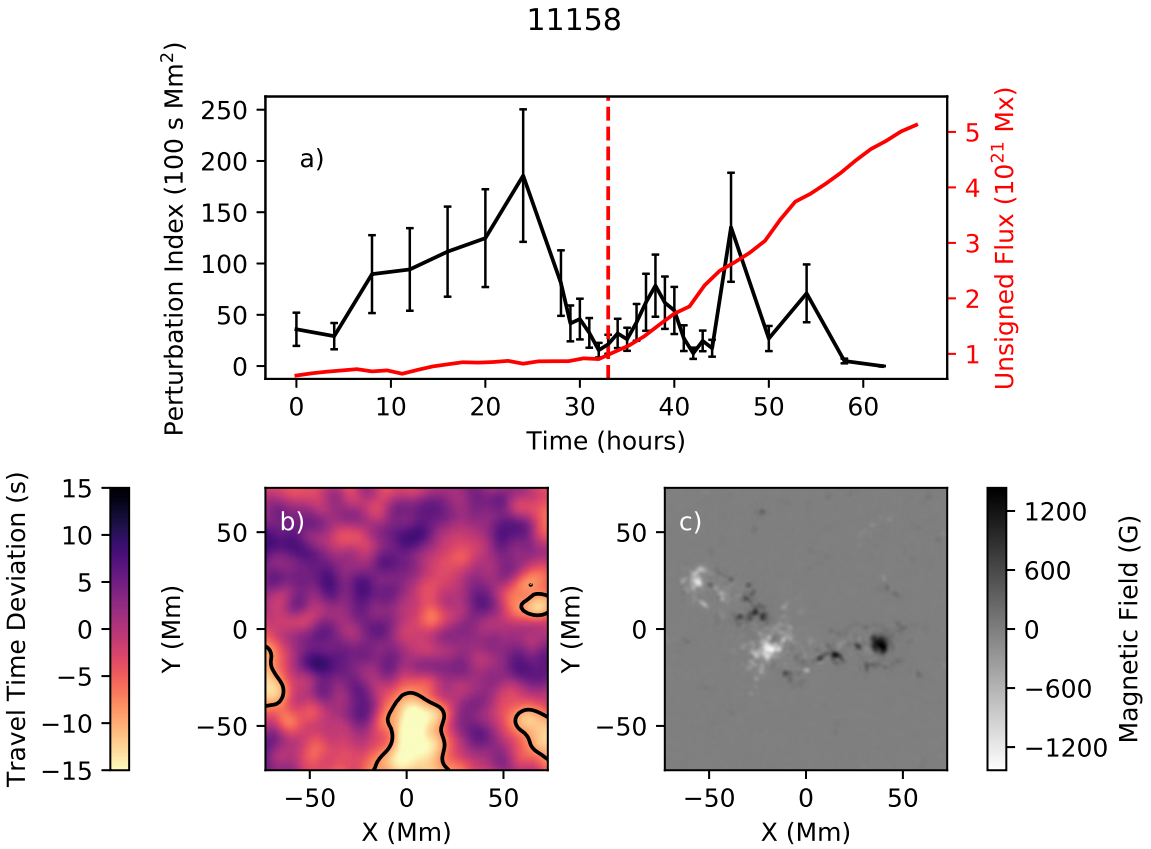

Figure 2.10 Analysis of AR 11158. a) Perturbation index over time (black) and the unsigned magnetic flux (red) where the vertical red dashed line indicates the approximate time of emergence; b) Travel time map at the time of peak perturbation index where the regions which meet the 2σ threshold are bounded by the solid dashed line; and c) Magnetogram of the active region at the end of the data series.
Source: Stefan et al. (2021)

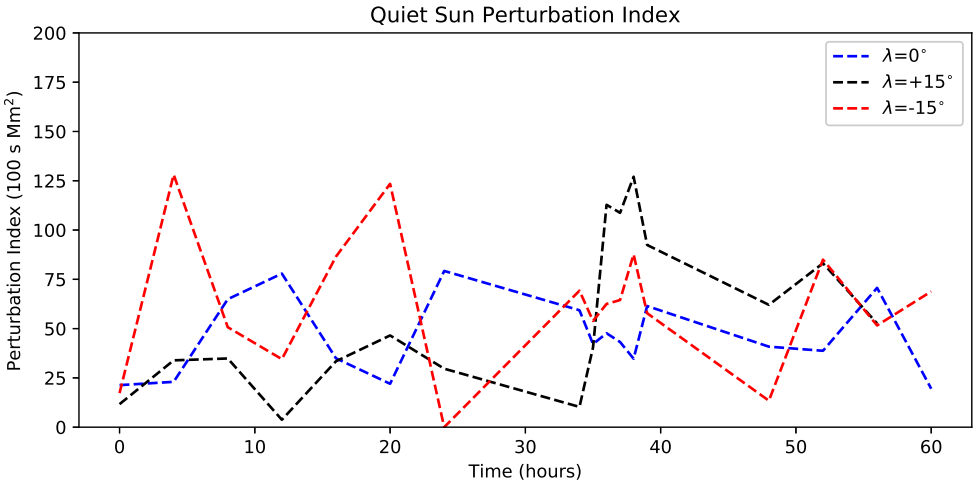

Figure 2.11 Perturbation index of 3 Quiet Sun regions with heliographic latitude +15° (black), 0° (blue), and -15° (red), and equal longitude.
Source: Stefan et al. (2021)

by a gradual decline, this isn't observed in either of the other quiet Sun regions. Furthermore, we expect—and observe in the case of ARs 11158 and 12772—the opposite trend, where perturbation index increases gradually before sharply falling.

The interpretation is the following, where a concentration of magnetic flux has risen into focus at $z = -70$ Mm, slightly perturbing the mean phase travel time. As the flux continues to rise, the mean phase travel time is further perturbed by introduction of more flux in our vertical field of view. Once the lower extent of the flux concentration crosses $z = -70$ Mm, we expect the perturbation index to begin to sharply decline. This asymmetrical development is expected as there is an uneven sensitivity which we use to probe the interior; as seen in Figure 2.4, deeper perturbations correspond to stronger shifts in the mean phase travel time. We also see that when the perturbation begins to rise out of focus, as in Figures 2.4a and 2.4b,

the size and magnitude of the travel time deviations decreases compared to deeper perturbations.

2.5 Statistics of Emerging Active Regions in Solar Cycle 24

In this section, we consider the mean phase travel time deviations obtained both through the Gabor wavelet fitting procedure as well as the GB02 method. We also adjust the threshold by which the perturbation index is computed. Where the perturbation index was previously computed using the 2σ value from the series of travel time maps of a given active region, we impose a more strict threshold here. Using the quiet Sun travel times obtained in the previous section, we set the threshold as the 99^{th} percentile of negative mean phase travel time deviations from the entire series for each arc segment case. These thresholds range from -7.1 to -10.2 seconds for the GB02 travel times, and from -7.1 to -8.5 for the Gabor-wavelet derived travel times.

We also consider the correlation lag time between changes in the mean phase travel time deviation and the unsigned surface magnetic field. Where the perturbation index has some predictive capability in that it can be computed from current data, the correlation lag time requires the entire sequence of travel time maps and Magnetograms. For each pixel, we subtract the mean and normalize both the mean phase travel time deviations and the unsigned surface magnetic field, and then compute the cross-correlation. The normalization ensures that an absolute correlation can be determined, i.e. a value between -1 and 1. The cross-correlations between the travel times and magnetic field are then averaged for pixels where the unsigned surface magnetic field eventually reaches 100 G or more, and we identify the correlation lag time from the maximum in the averaged cross-correlation.

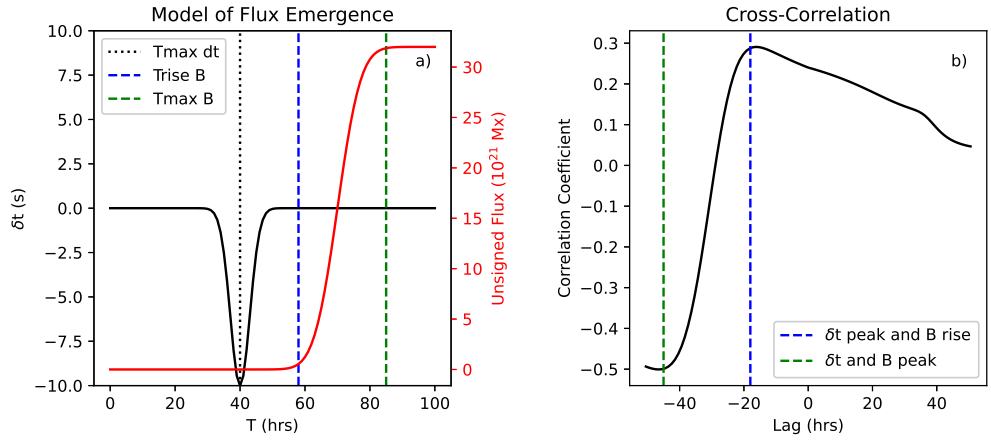

Figure 2.12 a) Simple model of flux emergence, with the magnetic field (red) increasing as an error function and the travel time deviation (black) peaking prior to emergence. b) Cross-correlation of the magnetic field and travel time deviation. The green dashed line in b) marks the minimum of the cross-correlation, with the lag equal to the separation of the travel time deviation and magnetic field peaks. The blue dashed line in b) marks the maximum of the cross-correlation, with the lag equal to the separation between the travel time deviation peak and onset of the magnetic field's rise.

2.5.1 Toy Model for Flux Emergence

In order to determine what features should be expected in the travel time - magnetic field cross-correlation, we consider a simple model for flux emergence. Here, the travel time deviation is Gaussian in time, with a FWHM of 8 hours and separated from the time of peak emergence by 30 hours. The magnetic field increases as an adjusted error function, taking around 20 hours to reach its peak. Both quantities are shown in Figure 2.12a, with the vertical green dashed line indicating when the magnetic field has saturated and the blue dashed line showing the onset of flux emergence. The peak in the travel time deviation is indicated by the black dotted line, which serves as a reference point for comparison with the rise and peak times of the magnetic field.

We find that the minimum of the cross-correlation, indicated by the green dashed line in Figure 2.12b, occurs at a lag equal to the time between the travel time deviation's peak and the increase of the magnetic field, i.e. the onset of flux

emergence. Intuitively, we should expect the cross-correlation to peak here, as the return of the travel time deviation to zero has a similar functional form to the rise of the magnetic field. The maximum of the cross-correlation, indicated by the blue dashed line in Figure 2.12b, occurs at a lag equal to the the time between the peak travel time deviation and peak magnetic field. This should also be expected, as the negative peak of the travel time deviation and the positive peak of the magnetic field contribute most strongly to the cross-correlation when the two are aligned, forming the indicated minimum. In this work, we are most interested in the delay between strong negative travel time deviations and the onset of flux emergence, so we will focus on the time lag associated with the minimum in the cross-correlation.

2.5.2 Observed Correlations

We first examine the distribution of correlation lag times for each of the arc segment cases and travel time procedures, as shown in Figure 2.13. In all cases, there are more negative lag times than positive, with the GB02-derived, 8 arc segment method yielding negative lag times in 36 of the 46 active regions; in fact, the GB02 procedure outperforms the Gabor wavelet procedure in every case. The median correlation lag time varies with the number of arc segments, though the 14 arc segment case performs most poorly with a median correlation lag time of -10 hours for the GB02 procedure and -12 hours for the Gabor wavelet procedure. The 8 arc segment case produces the greatest median correlation time lag of -16 hours for both procedures, and median correlation lag time decreases in both the GB02 and Gabor wavelet procedures as the number of arc segments increases.

The median lag time associated with the peak in the perturbation index does not follow this trend, however, and actually increases with the number of arc segments. The median lag time from the perturbation index in the 6 arc segment case is -10 hours for both travel time procedures, reaching a maximum of -14 hours for the

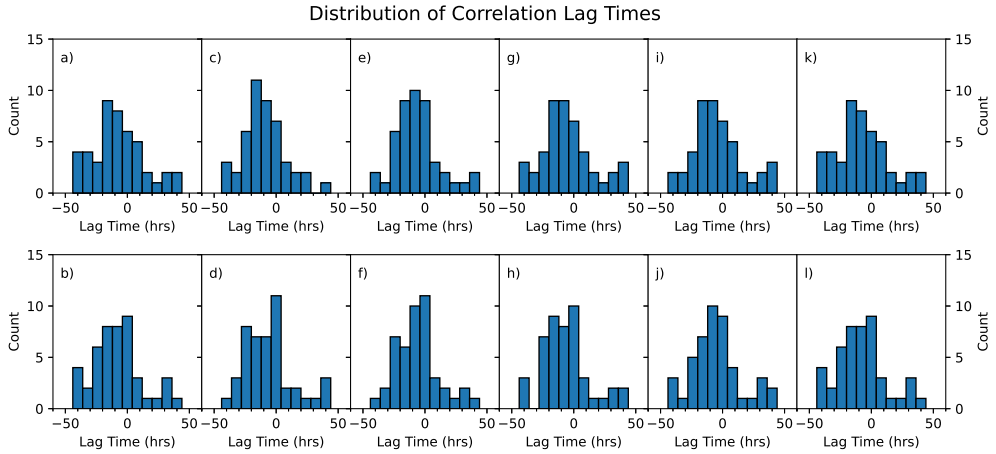

Figure 2.13 Distribution of correlation lag times for the travel times obtained with $n = 6$ arc segments (a,b), $n = 8$ arc segments (c,d), $n = 10$ arc segments (e,f), $n = 12$ arc segments (g,h), $n = 14$ arc segments (i,j), and by the average of the five cases (k,l). The first row is derived from the GB02 travel time procedure, and the second row from the Gabor wavelet fitting procedure.

GB02 procedure and -20 hours for the Gabor wavelet procedure, both with the 14 arc segment case. We next compare the perturbation index indicated lag time with the correlation lag time in Figure 2.14 and compute the Pearson correlation coefficient for each case. For the GB02 procedure, the two lag times are most correlated in the 8 arc segment case (Figure 2.14e) with a weak correlation coefficient of $r = 0.03$. The perturbation index and lag times derived from the Gabor wavelet procedure are also most correlated in the 8 arc segment case (Figure 2.14d), with $r = 0.21$. For both the GB02 and Gabor wavelet procedures, the greatest correlation between perturbation index and lag times are associated with the arc segment case which yields the greatest number of negative correlation lag times.

We now examine the relationship between the correlation lag times and relevant active region characteristics, and here we consider the case where the travel times are obtained through averaging the cross-correlations over the different number of arc segments. As opposed to the previous comparison, we do not necessarily expect a linear relationship with the active region characteristics, so here we use the Spearman

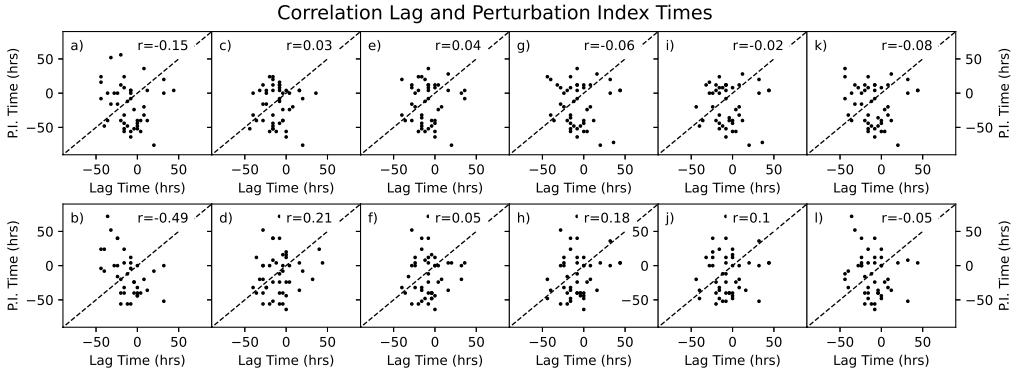

Figure 2.14 Comparison between the correlation lag times and the peak perturbation index times; the plots are organized as in Figure 2.13.

correlation coefficient instead of the Pearson correlation coefficient. The Spearman coefficient evaluates the monotonicity of a relationship, where the Pearson coefficient evaluates the linearity. The first quantity we examine is the maximum magnetic flux of an active region, Figures 2.15a and 2.15d, and find that there is a weak anti-correlation with the correlation lag time for the GB02 procedure, and far weaker for the Gabor wavelet procedure, with $\rho = -0.22$ and $\rho = -0.09$ respectively. There is a relationship of similar strength between the correlation lag times and the maximum flux rates, Figures 2.15b and 2.15e, with $\rho = -0.40$ for both the GB02 and the Gabor wavelet procedures. There is also a weak anti-correlation between the correlation lag times and sunspot sizes, Figures 2.15c and 2.15f, with $\rho = -0.16$ and $\rho = -0.22$ for the GB02 and Gabor wavelet procedures, respectively.

After removing the active regions with positive correlation lag times, which do not predict flux emergence, the probability that the sunspot sizes are uncorrelated with the lag times increases, from $p = 0.26$ to $p = 0.39$ for the GB02 procedure and $p = 0.14$ to $p = 0.50$ for the Gabor procedure. Reevaluating the relationship between the maximum fluxes also leads to a significant increase in the probability of no correlation, increasing from $p = 0.14$ to $p = 0.40$ for the GB02 procedure and from $p = 0.57$ to $p = 0.77$ for the Gabor wavelet procedure. There is also an increase in the

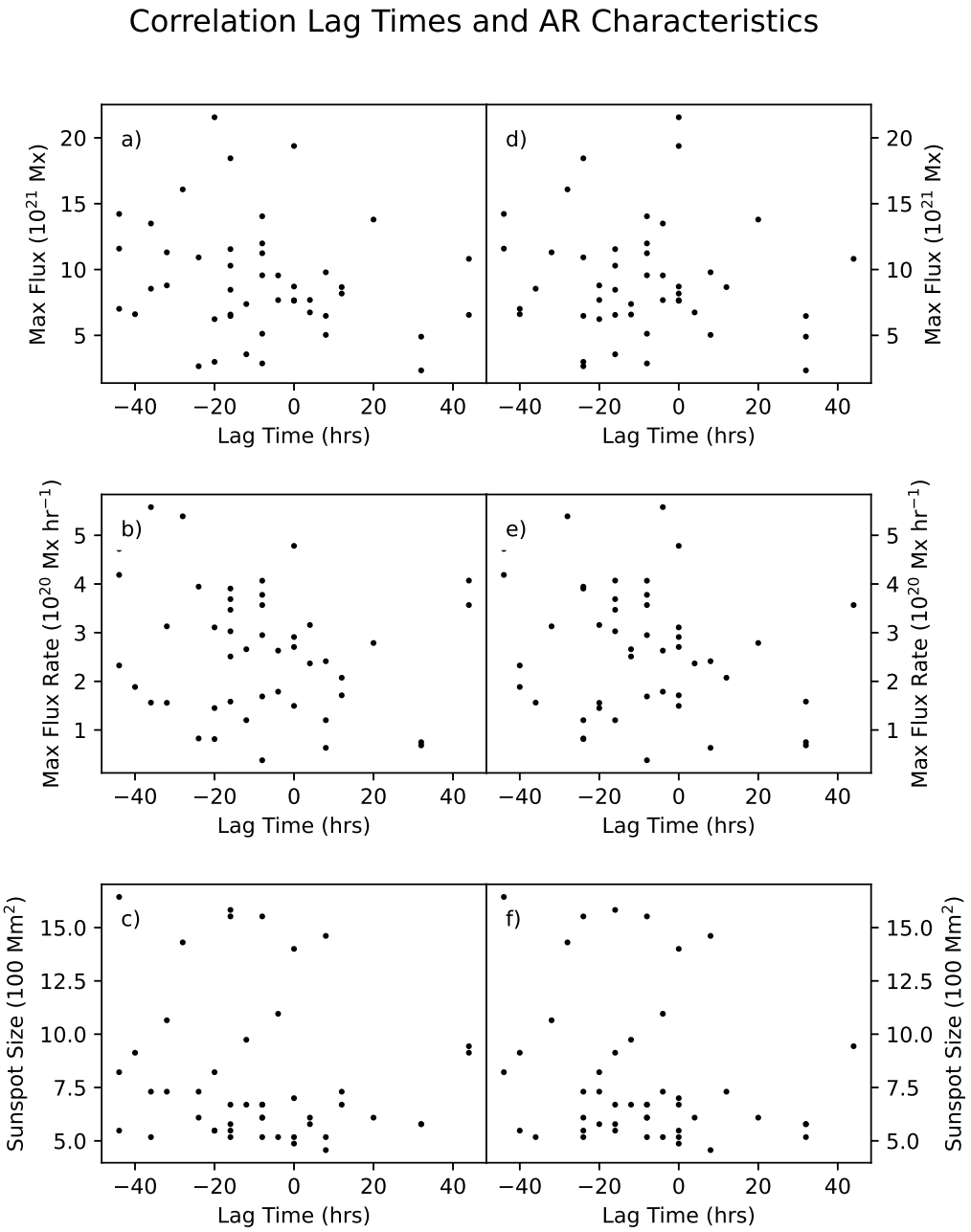

Figure 2.15 Comparison between the correlation lag times for the GB02 procedure (left column) and Gabor wavelet procedure (right column), and an active region's maximum magnetic flux (a,d); an active regions maximum flux rate (b,e); and an active region's size (c,f).

probability of no correlation for the maximum flux rates, from $p = 0.17$ to $p = 0.37$ for the GB02 procedure and $p = 0.18$ to $p = 0.91$ for the Gabor wavelet procedure.

CHAPTER 3

ASSESSMENT OF SUBSURFACE MAGNETIC FIELDS

3.1 Deriving the Wavenumber Perturbation from Magnetic Fields

The basis of our detection of subsurface magnetic fields is the perturbation to a given oscillation's wavenumber in the presence of a magnetic field. This change in the wavenumber is derived from the treatment of oscillations in an initially stationary plasma with an arbitrarily-oriented background magnetic field $\mathbf{B_0}$ as linear perturbations to the conservation of mass (Equation (3.1)) and momentum (Equation (3.2)), the induction equation (Equation (3.3)), and the adiabatic condition (Equation (3.4)). Denoting the perturbation to quantity a as a', the linearized equations are

$$\frac{\partial \rho'}{\partial t} = -\rho_0 \nabla \cdot \mathbf{v}, \tag{3.1}$$

$$\rho_0 \frac{\partial \mathbf{v}}{\partial t} = -\nabla \left(c_s^2 \rho' \right) + \frac{1}{4\pi} \left(\nabla \times \mathbf{B}' \right) \times \mathbf{B_0}, \tag{3.2}$$

$$\frac{\partial \mathbf{B}'}{\partial t} = \nabla \times \left(\mathbf{v} \times \mathbf{B_0} \right), \tag{3.3}$$

and

$$p' = c_s^2 \rho'. \tag{3.4}$$

For simplicity, we will consider Cartesian coordinates and plan wave solutions, and orient our coordinate system such that the direction of wave propagation is in the $\hat{\mathbf{z}}$-direction. This orientation leaves the possibility of the magnetic field

having some component in all three directions; however, we can further rotate our coordinate system about the $\hat{\mathbf{z}}$-axis so that horizontal component of the field lies entirely along the $\hat{\mathbf{y}}$-axis. With the background magnetic field now of the form $\mathbf{B_0} = (0, B_0 \sin\alpha, B_0 \cos\alpha)^{\mathrm{T}}$, where α is the angle between the $\hat{\mathbf{z}}$-axis and the magnetic field, and the following conditions

$$\frac{\partial}{\partial x} = \frac{\partial}{\partial y} = 0; \frac{\partial}{\partial z} = ik; \frac{\partial}{\partial t} = -i\omega, \tag{3.5}$$

Equation (3.2) reduces to

$$\begin{cases} \omega\rho_0 v_x + \dfrac{B_0}{4\pi} k B'_x \cos\alpha = 0 \\ \omega\rho_0 v_y + \dfrac{B_0}{4\pi} k B'_y \cos\alpha = 0 \\ \omega\rho_0 v_z - k c_s^2 \rho' - \dfrac{B_0}{4\pi} k B'_y \sin\alpha = 0 \end{cases}, \tag{3.6}$$

and Equation (3.3) to

$$\begin{cases} \omega B'_x + B_0 k v_x \cos\alpha = 0 \\ \omega B'_y + B_0 k v_y \cos\alpha - B_0 k v_z \sin\alpha = 0 \\ \omega B'_z = 0 \end{cases}. \tag{3.7}$$

Expansion of Equation (3.1) simply yields

$$\omega\rho' - k\rho_0 v_z = 0. \tag{3.8}$$

We can obtain the dispersion relation for Alfvén waves by solving for v_x in the momentum equation and substituting the result into the induction equation. This gives

$$\omega^2 \rho_0 - k^2 \frac{B_0^2}{4\pi} \cos^2 \alpha = 0 \rightarrow \omega = k c_A \cos \alpha \tag{3.9}$$

where $c_A = B_0/\sqrt{4\pi\rho_0}$ is the Alfvén speed. Alfvén waves propagate in the direction of the magnetic field, which is also their restoring force. The remaining four equations, two from the induction equation and two from the momentum equation, can be solved as a matrix equation to yield the dispersion relation for magnetoacoustic waves

$$\left(\frac{\omega}{k}\right)^2 = \frac{1}{2}\left(c_A^2 + c_s^2\right) \pm \frac{1}{2}\sqrt{c_A^4 + c_s^4 - 2c_A^2 c_s^2 \cos 2\alpha}, \tag{3.10}$$

which has two modes: the fast mode (+) and the slow mode (−). Both modes have pressure and the magnetic field as their restoring force, the contributions of which enhance each other for the fast mode and partially negate for the slow mode. Additionally, these waves do not necessarily need to propagate in the direction the magnetic field. We can simplify the above using the cosine double angle identity to

$$\left(\frac{\omega}{k}\right)^2 = \frac{1}{2}\left[c_A^2 + c_s^2 \pm \sqrt{c_A^4 + c_s^4 - 2c_s^2 c_A^2 (2\cos^2 \alpha - 1)}\right], \tag{3.11}$$

which facilitates the use of the dot product to make the interaction between the wavevector and the Alvén velocity more clear in the following form,

$$\left(\frac{\omega}{k}\right)^2 = c_{\mathrm{MHD}}^2 = \frac{1}{2}\left[c_A^2 + c_s^2 \pm \sqrt{\left(c_A^2 + c_s^2\right)^2 - 4c_s^2\left(\frac{\mathbf{k}\cdot\mathbf{c_A}}{|\mathbf{k}|}\right)^2}\right]. \tag{3.12}$$

Here, we have defined the magnetoacoustic wave speed c_{MHD} which takes the value $c_{\mathrm{f,MHD}}$ for the fast mode and $c_{s,\mathrm{MHD}}$ for the slow mode.

Considering some variable $x = c_A^2/c_s^2$, the above can be expressed in cosine form as

$$c_{\mathrm{MHD}}^2(x) = \frac{c_s^2}{2}\left[x + 1 \pm \sqrt{x^2 + 1 + 2x + 4xk^2\cos^2\alpha}\right]. \tag{3.13}$$

While this temporarily complicates our dispersion relation, we expect the Alfvén speed to be smaller than the local sound speed for sufficiently small magnetic field $\mathbf{B_0}$, such that we can consider small perturbations to the magnetoacoustic wave speed about $x = 0$. Specifically, we apply a first order Taylor expansion to the fast magnetoacoustic wave speed,

$$c_{\mathrm{f,MHD}}^2(x) \approx c_{\mathrm{f,MHD}}^2(x=0) + x\,\frac{d}{dx}\left(c_{\mathrm{f,MHD}}^2\right)\Big|_{x=0}, \tag{3.14}$$

which simplifies to

$$c_{\mathrm{f,MHD}}^2 \approx c_s^2 + \left(c_A^2 - \left(\frac{\mathbf{k} \cdot \mathbf{c_A}}{|\mathbf{k}|} \right)^2 \right). \tag{3.15}$$

We now derive the perturbation to a given oscillation mode's wavenumber by again Taylor expanding the fast magnetoacoustic speed to first order, though now using the relation $c_{\mathrm{f,MHD}}^2 = \omega^2/k^2$ and expanding about the unperturbed wavenumber k_0. We then have

$$\begin{aligned} c_{\mathrm{f,MHD}}^2(k) &= c_{\mathrm{f,MHD}}^2(k_0) + (k - k_0) \left. \frac{d}{dk} \left(c_{\mathrm{f,MHD}}^2 \right) \right|_{k=k_0} \\ &= c_{\mathrm{f,MHD}}^2(k_0) + \delta k \left. \frac{d}{dk} \left(c_{\mathrm{f,MHD}}^2 \right) \right|_{k=k_0} \\ &= \frac{\omega^2}{k_0^2} - 2\delta k \frac{\omega^2}{k_0^3} \\ &= c_s^2 - 2\delta k \frac{\omega^2}{k_0^3} \end{aligned} , \tag{3.16}$$

where the last equality makes use of the unperturbed dispersion relation $\omega = c_s k$. Finally, the above expression can be substituted in the previous Taylor expansion of $c_{\mathrm{f,MHD}}$ as

$$c_s^2 + \left(c_A^2 - \left(\frac{\mathbf{k} \cdot \mathbf{c_A}}{|\mathbf{k}|} \right)^2 \right) = c_s^2 - 2\delta k \frac{\omega^2}{k_0^3}. \tag{3.17}$$

Rearranging the above to solve for δk, the perturbation to the wavenumber, gives

$$\delta k = -\frac{1}{2}\frac{k_0^3}{\omega^2}\left(c_A^2 - \left(\frac{\mathbf{k}\cdot\mathbf{c_A}}{|\mathbf{k}|}\right)^2\right) \tag{3.18}$$

Note that perturbations to wavenumber produce perturbations to the wave travel time via the following relation,

$$\delta\tau = \frac{1}{\omega}\int_\Gamma \delta k ds, \tag{3.19}$$

so it can be expected that the perturbation to the wave travel time in the presence of sufficiently weak magnetic fields can be expressed as

$$\delta\tau = -\int_\Gamma \frac{1}{2}\left[\frac{c_A^2}{c_s^2} - \left(\frac{\mathbf{k}\cdot\mathbf{c_A}}{|\mathbf{k}|c_s}\right)^2\right] S ds. \tag{3.20}$$

As in Chapter 2, $S = k/\omega$ is the phase slowness and $\delta\tau$ is the perturbation to the phase travel time.

3.2 Isolating the Azimuth and Magnitude of the Horizontal Magnetic Field from Phase Travel Times

While we have neatly summarized how magnetic fields are expected to perturb the phase travel time of acoustic waves, these are not the only perturbations an acoustic wave may encounter in a realistic setting. We must also consider the effect that flows as well as changes in sound speed and acoustic cut-off frequency have, which together

provide a perturbation to the one-way phase travel time given by

$$\delta\tau = -\int_\Gamma \left[\frac{\mathbf{n}\cdot\mathbf{U}}{c^2} + \frac{\delta c}{c} S + \frac{\delta\omega_c}{\omega_c}\frac{\omega_c^2}{\omega^2 c^2 S} + \frac{1}{2}\left(\frac{|\mathbf{c_A}|^2}{c^2} - \frac{(\mathbf{k}\cdot\mathbf{c_A})^2}{|\mathbf{k}|^2 c^2} \right) S \right] ds, \tag{3.21}$$

where $\mathbf{n} = \mathbf{k}/|\mathbf{k}|$ is the direction of wave propagation, $\mathbf{U}$ is the flow velocity, δc is the perturbation to the sound speed, and $\delta\omega_c$ is the perturbation to the acoustic cut-off frequency ω_c. A more detailed discussion of the non-magnetic terms can be found in Kosovichev & Duvall (1997); for our purposes, it is enough to know that these additional perturbations exist and how they behave. On small enough scales, where the perturbations can be considered constant along the ray path Γ, the contribution to the travel time from sound speed and cut-off frequency perturbations is the same regardless of the direction the wave is propagating in. The contribution from flows can be isolated by taking the difference between the forward and backward phase travel time, while taking the mean of these phase travel times removes its contribution. This leaves

$$\delta\tau_{\text{mean}} = T_A - \frac{1}{2}\int_\Gamma \left(\frac{|\mathbf{c_A}|^2}{c^2} - \frac{(\mathbf{k}\cdot\mathbf{c_A})^2}{|\mathbf{k}|^2 c^2} \right) S ds, \tag{3.22}$$

where the sound speed and cut-off frequency terms are represented by T_A.

For a background magnetic field having radial component B_r and total horizontal component $B_h = \sqrt{B_\theta^2 + B_\phi^2}$, the mean phase travel time deviation along

the North-South axis, labeled by $\delta\tau^{(1)}_{\text{mean}}$, is given by

$$\delta\tau^{(1)}_{\text{mean}} = T_A - \frac{1}{2}\int_\Gamma \frac{1}{|\mathbf{k}|^2 c^2}\left[\frac{1}{4\pi\rho}\left(k_r^2+k_h^2\right)\left(B_r^2+B_h^2\right) - \frac{1}{4\pi\rho}\left(k_r B_r + k_h B_h\cos(\alpha)\right)^2\right] Sds. \tag{3.23}$$

For this particular configuration, the wave is traveling entirely along the $\hat{\theta}$-direction, such that only the polar-angle and radial terms remain in Equation (3.22). Here, α is the angle between the horizontal magnetic field and the North-South axis—the magnetic field's azimuth. We now assume that the magnetic field is uniform along the ray path, and the expected mean perturbation of a North-South traveling acoustic wave is

$$\delta\tau^{(1)}_{\text{mean}} = T_A - \frac{1}{2}\int_\Gamma \frac{1}{|\mathbf{k}|^2 c^2}\left(k_r^2 c_{A,h}^2 + k_h^2 c_{A,r}^2\right) Sds - \left(\frac{1}{2}\int_\Gamma \frac{1}{|\mathbf{k}|^2 c^2} k_h^2 c_{A,h}^2 Sds\right)\sin^2(\alpha) + \left(\int_\Gamma \frac{1}{|\mathbf{k}|^2 c^2} k_r k_h c_{A,r} c_{A,h} Sds\right)\cos(\alpha). \tag{3.24}$$

We can further reduce this expression by realizing that the last term is anti-symmetric along the ray path; the sign of k_r changes from negative to positive after the wave travels past the turning point, but we have assumed that the magnetic field is uniform. This then reduces to

$$\delta\tau^{(1)}_{\text{mean}} = T_A - \frac{1}{2}\int_\Gamma \frac{1}{|\mathbf{k}|^2 c^2}\left(k_r^2 c_{A,h}^2 + k_h^2 c_{A,r}^2\right) Sds - \left(\frac{1}{2}\int_\Gamma \frac{1}{|\mathbf{k}|^2 c^2} k_h^2 c_{A,h}^2 Sds\right)\sin^2(\alpha). \tag{3.25}$$

The above treatment is also applied to acoustic waves traveling along the Northeast-Southwest direction, ($\delta\tau^{(2)}_{\text{mean}}$), along the East-West direction ($\delta\tau^{(3)}_{\text{mean}}$), and along the Southeast-Northwest direction ($\delta\tau^{(4)}_{\text{mean}}$). For each increment, we re-orient our coordinate system so that the acoustic wave is always propagating along the local $\hat{\theta}$-direction which simplifies the corresponding expressions for the mean travel time perturbation. After accounting for the $\pi/4$ rotation in each additional increment, the expected mean phase travel time perturbations are

$$\begin{aligned}\delta\tau^{(2)}_{\text{mean}} = T_A - \frac{1}{2}\int_\Gamma \frac{1}{|\mathbf{k}|^2 c^2}\left(k_r^2 c_{A,h}^2 + k_h^2 c_{A,r}^2\right) Sds \\ - \left(\frac{1}{2}\int_\Gamma \frac{1}{|\mathbf{k}|^2 c^2} k_h^2 c_{A,h}^2 Sds\right)\sin^2\left(\alpha + \frac{\pi}{4}\right),\end{aligned} \tag{3.26}$$

$$\begin{aligned}\delta\tau^{(3)}_{\text{mean}} = T_A - \frac{1}{2}\int_\Gamma \frac{1}{|\mathbf{k}|^2 c^2}\left(k_r^2 c_{A,h}^2 + k_h^2 c_{A,r}^2\right) Sds \\ - \left(\frac{1}{2}\int_\Gamma \frac{1}{|\mathbf{k}|^2 c^2} k_h^2 c_{A,h}^2 Sds\right)\cos^2(\alpha),\end{aligned} \tag{3.27}$$

and

$$\begin{aligned}\delta\tau^{(4)}_{\text{mean}} = T_A - \frac{1}{2}\int_\Gamma \frac{1}{|\mathbf{k}|^2 c^2}\left(k_r^2 c_{A,h}^2 + k_h^2 c_{A,r}^2\right) Sds \\ - \left(\frac{1}{2}\int_\Gamma \frac{1}{|\mathbf{k}|^2 c^2} k_h^2 c_{A,h}^2 Sds\right)\cos^2\left(\alpha + \frac{\pi}{4}\right).\end{aligned} \tag{3.28}$$

Subtracting the East-West travel time perturbation (Equation (3.27)) from the North-South perturbation (Equation (3.25)), and similarly the Southeast-Northwest perturbation (Equation (3.28)) from the Northeast-Southwest perturbation (Equation

(3.26)), gives

$$\begin{aligned}\delta\tau^{(1)}_{\text{mean}} - \delta\tau^{(3)}_{\text{mean}} &= -\left(\frac{1}{2}\int_\Gamma \frac{1}{|\mathbf{k}|^2 c^2} k_h^2 c_{A,h}^2 S ds\right)\left(\sin^2(\alpha) - \cos^2(\alpha)\right) \\ &= \left(\frac{1}{2}\int_\Gamma \frac{1}{|\mathbf{k}|^2 c^2} k_h^2 c_{A,h}^2 S ds\right)\cos(2\alpha)\end{aligned} \tag{3.29}$$

and

$$\begin{aligned}\delta\tau^{(2)}_{\text{mean}} - \delta\tau^{(4)}_{\text{mean}} &= -\left(\frac{1}{2}\int_\Gamma \frac{1}{|\mathbf{k}|^2 c^2} k_h^2 c_{A,h}^2 S ds\right)\left(\sin^2\left(\alpha + \frac{\pi}{4}\right) - \cos^2\left(\alpha + \frac{\pi}{4}\right)\right) \\ &= -\left(\frac{1}{2}\int_\Gamma \frac{1}{|\mathbf{k}|^2 c^2} k_h^2 c_{A,h}^2 S ds\right)\sin(2\alpha).\end{aligned} \tag{3.30}$$

We can now combine Equations (3.29) and (3.30) to extract expressions for the magnetic field's azimuth

$$\alpha = \frac{1}{2}\tan^{-1}\left(-\frac{\delta\tau^{(2)}_{\text{mean}} - \delta\tau^{(4)}_{\text{mean}}}{\delta\tau^{(1)}_{\text{mean}} - \delta\tau^{(3)}_{\text{mean}}}\right), \tag{3.31}$$

and a quantity which we call the magnetic anisotropy parameter

$$A \equiv \int_\Gamma \frac{1}{|\mathbf{k}|^2 c^2} k_h^2 c_{A,h}^2 S ds = 2\sqrt{\left(\delta\tau^{(2)}_{\text{mean}} - \delta\tau^{(4)}_{\text{mean}}\right)^2 + \left(\delta\tau^{(2)}_{\text{mean}} - \delta\tau^{(4)}_{\text{mean}}\right)^2}, \tag{3.32}$$

which is directly proportional to the magnitude of the horizontal magnetic field.

3.3 Procedure for Measuring Characteristics of the Subsurface Magnetic Field

As described in Subection 2.1.2, it is necessary to apply phase speed filters to the oscillation data in order to isolate modes penetrating to a desired depth. Here, we are looking at much more shallow layers of the solar interior—between 5 and 13 Mm beneath the photosphere—for which there are standardized phase speed filters used by the Joint Science Operations Center (JSOC) of SDO for the processing of Dopplergrams in their time-distance pipeline (Zhao et al., 2012). We use these same phase speed filter parameters in this chapter for the sake of compatibility with other helioseismic data products. A complete description of the parameters is listed in Table 3.1, where the term annulus group denotes the collection of measurement annuli which reach the desired depth range.

The corresponding annulus groups for our desired vertical view are annulus group 4, with turning point depths $z = -5$ to -7 Mm; annulus group 5, with turning point depths $z = -7$ to -10 Mm; and annulus group 6, with turning point depths $z = -10$ to -13 Mm. The travel time perturbations for the very shallow layers probed by annulus groups 1, 2, and 3 ($z = 0$ to -3 Mm) are generally too noisy to extract useful magnetic field information. Additionally, annulus groups 7 ($z = -13$ to -17 Mm) to 11 ($z = -30$ to -35 Mm) require long time series to resolve the perturbations caused by the magnetic field. The effects of acoustic perturbations become much stronger than those from the magnetic field, as the ratio of Alfvén speed to sound speed becomes exceedingly small with increasing depth.

To perform the measurements of the mean phase travel time deviations, we employ a similar procedure as described in Section 2.1.3. We use three measurement annuli in each annulus group, one each for the minimum, mean, and maximum horizontal travel distances listed in Table 3.1. The cross-correlation is computed for opposing arcs, each of which covers 45° and is oriented with respect to the

Table 3.1 Parameters for Annulus Groups 4, 5, and 6

Annulus Group	Depth Range (Mm)	Horizontal Travel Distance (deg)	Phase Velocity (km s^{-1})	Gaussian Width (km s^{-1})
4	5-7	1.44-1.80	28.83	9.40
5	7-10	1.92-2.40	36.48	5.91
6	10-13	2.40-2.88	40.25	5.17

Source: Stefan & Kosovichev (2022)

desired travel time measurement, for example the North-South mean. The exact orientation of the arcs is shown in Figure 2.2, with green corresponding to the North-South measurement, orange to the Northeast-Southwest measurement, blue to the East-West measurement, and red to the Southeast-Northwest measurement.

Whereas in Chapter 2 we cross-correlated opposing arcs, here we cross-correlate each arc with the central pixel. This technique, known as surface-focusing, is better suited for observation of shallow features (Braun & Birch, 2008). Instead of intersecting at the respective turning points, the acoustic rays in this configuration have one terminus at the outer arc and a shared terminus at the central pixel, indicated by the black dot in Figure 2.2. An example of the average ray path for the annulus groups used here is shown in Figure 3.1.

We measure the travel time deviations with both the Gabor wavelet fitting and GB02 method exactly as in Chapter 2, though with two additional intermediate steps. We, in effect, have two cross-correlations for a given measurement direction; for example, the North-South direction is sampled both by the North-to-center ray and by the South-to-center ray. We can then average the forward North-to-center and backward South-to-center cross-correlations to obtain a less noisy travel time for waves traveling from North to South. Similarly, averaging the backward North-to-center and forward South-to-center cross-correlations yields a less noisy travel time for waves traveling from South to North. The average of the deviations of these two travel times is the mean perturbation described by Equation (3.25). Our first modification to the procedure outlined in Subsection 2.1.3 is the application of such averaging to all the directional cross-correlations, and for the GB02 method these resulting cross-correlations are averaged over space and direction to obtain the reference cross-correlation C_{ref}. The second modification is an additional 2x2 spatial average of cross-correlations to further reduce noise in resulting travel times. The spatial resolution of

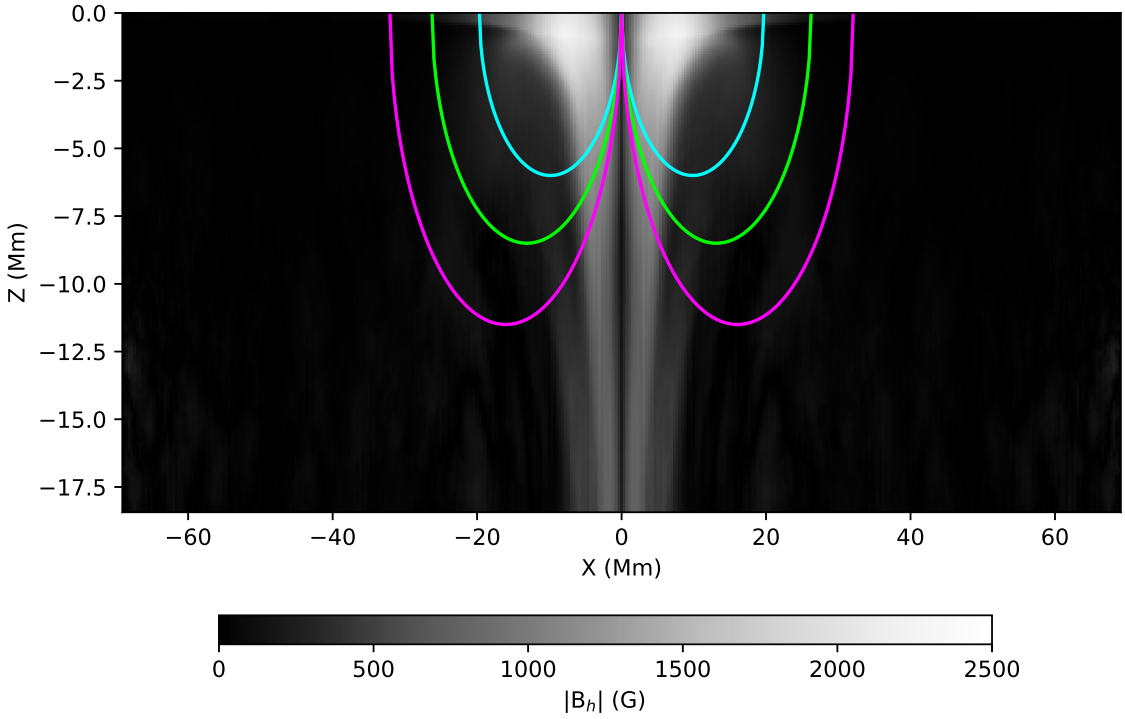

Figure 3.1 Mean path of acoustic waves in the surface-focus procedure, traveling through the simulated sunspot described in Subsection 3.4.2. The particular configuration shown here is for the measurement of the magnetic field at (x,y)=0 Mm. The mean path for oscillations in annulus group 4 is shown in cyan, for annulus group 5 in green, and annulus group 6 in magenta.
Source: Stefan & Kosovichev (2022)

our results is then increased by a factor of two and the number of pixels consequently reduced by a factor of two.

3.4 Validation of the Technique on Simulations

3.4.1 Simulation of Point-Source Acoustic Wave Propagation through a Uniform Magnetic Field

We first validate the time-distance technique by applying the measurement scheme to simulations developed by Parchevsky & Kosovichev (2009). Here, a point-source generates acoustic waves which propagate through a uniform, inclined background magnetic field. The model density and pressure stratification is derived from the Standard Solar Model (Christensen-Dalsgaard et al., 1996) such that the observed

p- and f-mode dispersion relations are reproduced. There are many simulations with various configurations of the background magnetic field, and we choose the simulation where the magnetic field has magnitude $B_0 = 1900$ G, making a 30° angle with the vertical and horizontal component oriented in $\hat{\mathbf{y}}$-direction. The amplitude and inclination of the field in this simulation closely resembles that of a sunspot umbra. While the authors make available all three components of the simulated photospheric velocity to study line-of-sight effects, this is beyond the scope of our investigation. We therefore assume the case of observations sufficiently close to disk center that use of only the radial component of the velocity is sufficient.

Using this simple model, we will show that the derived equations can be used to determine the magnetic field's azimuth, as well as provide a reliable measurement of the anisotropy parameter. The correct orientation of the subsurface horizontal field is already known from the simulation parameters, and the expected phase travel time anisotropy can be found by solving Equation (3.23) using the method described in Appendix A. Our secondary goal of using this model is to show that the magnetic field parameters can be extracted regardless of the orientation of our measurement scheme, i.e. that the measurement does not rely on a particular alignment with the magnetic field. This is accomplished by varying the orientation of the measurement annulus, Figure 2.2, in increments of 1° from the initial orientation along the North-South axis.

Figure 3.2 shows the results of this validation, with Figure 3.2a showing the raw mean travel times, Figure 3.2b showing the derived azimuth as a function of measurement orientation, and Figure 3.2c showing the measured anisotropy parameter (A) also as a function of measurement orientation. The mean phase travel times were computed using a Gabor wavelet fit to the time-dependent velocity located a distance 1.62 degrees—the average horizontal travel distance associated with annulus group 4—away from the excitation source. Since the excitation here is

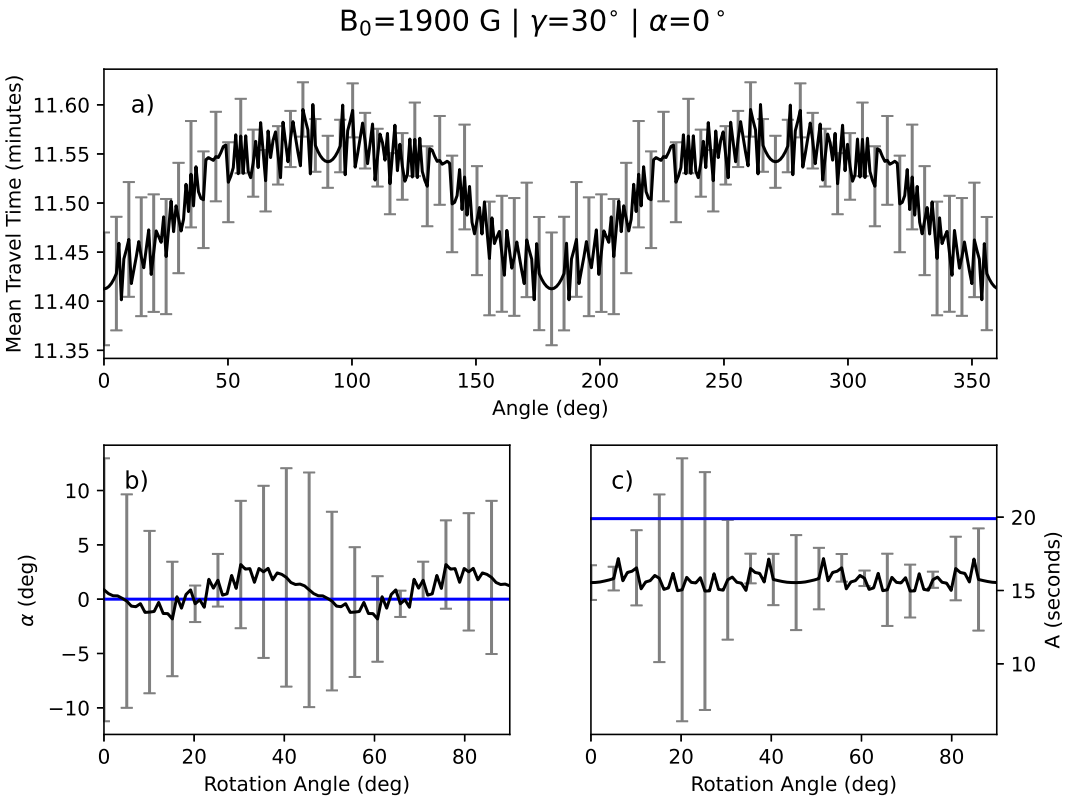

Figure 3.2 Validation of the measurement scheme. Panel a contains the mean phase travel times determined by the Gabor wavelet fit, panel b contains the field's inferred azimuth, and panel c contains the resulting travel time anisotropy. The blue line in panel b shows the field's true azimuth of 0° relative to the $+\hat{y}$- or NS-axis, and the blue line in panel c shows the expected travel time anisotropy from solving the ray equations for the specified field's parameters.
Source: Stefan & Kosovichev (2022)

impulsive and point-source, the resulting oscillations are essentially a Green's function and no cross-correlation is necessary.

We are able to measure the magnetic field's azimuth to within 2 to 3 degrees, as seen in Figure 3.2b. The small-scale variations in the azimuth originate from similar variations in the raw mean travel times, the larger variations with period 45° also originate from the variations in the raw mean travel times in increments of the same period. The anisotropy parameter in Figure 3.2c shows similar, but less extreme, variations. The average derived anisotropy is about 15.5 seconds compared to the

predicted value of 19.9 seconds. This discrepancy is likely due more to errors in predicted value's computation, which is strongly dependent on the density of grid points near the oscillation turning point. Furthermore, the computation in the ray approximation assumes plane-parallel waves which may not necessarily be true for the simulated oscillations at short travel distances. Additionally, the uncertainties reported in Figures 3.2b and 3.2c are selected from the maximum of four cases where the mean travel time uncertainties are either added or subtracted from the differences in Equations (3.31) and (3.32).

3.4.2 Realistic Sunspot Simulation with Solar-like Oscillations

We now test the measurement technique using a more realistic simulation of a sunspot developed by Rempel (2012), which is itself a modified version of *MURaM* radiative MHD code (Vögler et al., 2005). The numerical domain of the simulation is 98.304 Mm in both horizontal directions, which reduces our observational field of view to around 45 Mm in each direction. This restriction takes into account the additional space in each direction required for the measurement scheme of annulus group 4, which requires a maximum separation of ≈ 20 Mm between the arcs and central observation pixel because of oscillation travel distance. The vertical extent of the domain is 12.432 Mm, which is deep enough to accommodate measurements with annulus group 4 without encountering any numerical effects from the bottom boundary. The simulation is initialized with an axisymmetric flux concentration of 9×10^{21} Mx which eventually produces a sunspot with flux 6×10^{21} Mx. The data used in our analysis are the time series of the model's photospheric ($\tau = 0.01$) vertical velocity, which begins 50 hours after the simulation is initiated. The time series has duration 25 hours and cadence of 45 seconds with horizontal resolution 0.384 Mm per pixel.

In this case, the known parameters of the subsurface magnetic field are the azimuthally-averaged magnitude of the horizontal component and the orientation

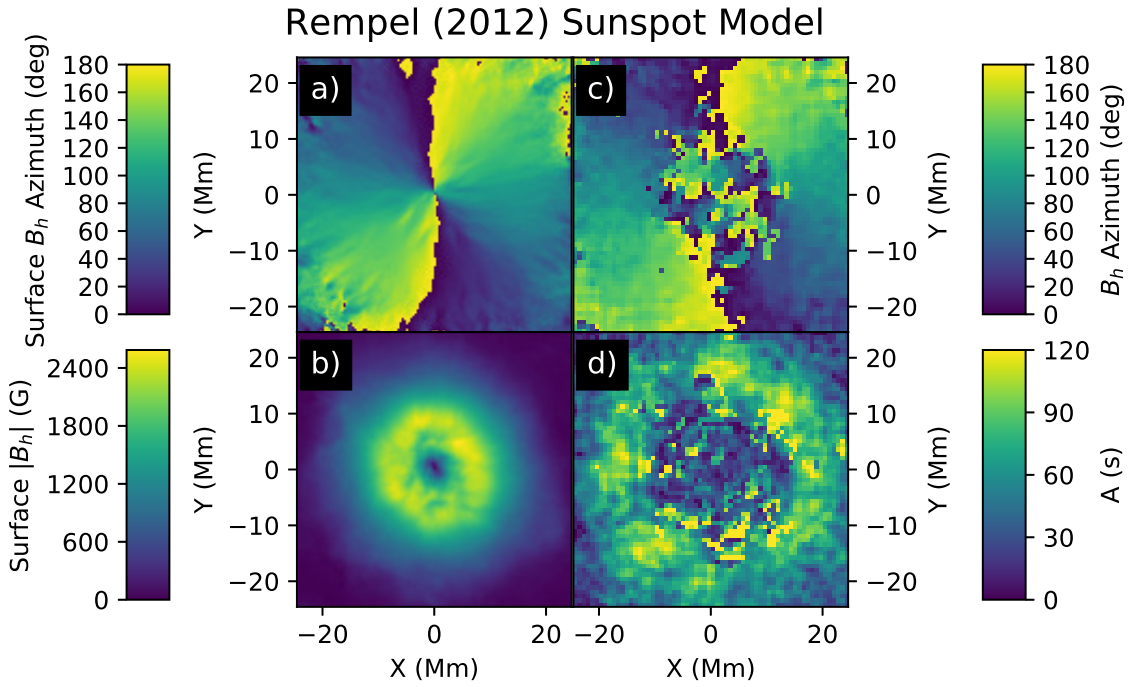

Figure 3.3 Comparison of the model's surface magnetic field azimuth (a) and magnitude (b) with the measured subsurface azimuth (c) and travel time anisotropy (d).
Source: Stefan & Kosovichev (2022)

of the field is taken to be the same as the surface orientation. The horizontal component's magnitude is shown in Figure 3.1 along with the average ray path of annulus groups 4, 5, and 6. The results of our analysis are shown in Figure 3.3, with Figures 3.3a and 3.3b showing the surface magnetic field azimuth and magnitude of the horizontal component, respectively. Here, the measured azimuth, Figure 3.3c, and anisotropy, Figure 3.3d, are derived from the GB02 mean travel time deviations, which were less noisy in this case than the Gabor wavelet derived travel times. The outer 10 Mm of the measured azimuth correspond very well to the surface azimuth, though additional noise is present closer to the center of the sunspot. The inner 10 Mm of the measured azimuth is rotated 90° relative to the true azimuth and the measurements near the outer edge of the sunspot. This region also shows a significant lack of travel time anisotropy (Figure 3.3d) than would be expected from the spatial

structure of the horizontal magnetic field. Instead, we see that the greatest anisotropy occurs around 10 Mm from the true maximum of the horizontal field.

3.5 Assessing the Subsurface Magnetic Fields in Observed Sunspots

We proceed now to apply our measurement technique on sunspots observed by HMI. The input data sets here are tracked Dopplergrams which are remapped to a Postel's projection with a spatial resolution of 0.12 degrees per pixel. The time series has duration 24 hours with 45 second cadence, and each image in the series is 256 by 256 pixels in size. Taking into account the additional space needed for the measurement annuli and our 2x2 binning, the final map size is 64 by 64 pixels with spatial resolution 0.24 degrees per pixel.

The sunspots are selected based on the following criteria: that the size and shape of the sunspot, along with the magnitude and orientation of the magnetic field, remain approximately constant over the observation period, and that the area surrounding the sunspot is free of significant magnetic features which might contaminate the travel time measurements. The sunspots which satisfy these criteria are those associated with ARs 12218, 12786, and 12794, which are unipolar and roughly axisymmetric. We compute the unsigned magnetic flux of each sunspot with a minimum threshold of 200 G, to ensure that the computed flux corresponds to the sunspot itself and not the background. We compute the azimuth and anisotropy parameter from the travel times of annulus groups 4, 5, and 6 derived from both the Gabor wavelet fitting and GB02 methods. The observations of the respective sunspot's magnetic field azimuth, horizontal magnitude, and line-of-sight magnitude originate from a time series averaged over the duration of the Dopplergram measurements, with spatial resolution 0.12 degrees per pixel.

We first examine the subsurface magnetic field for AR 12218 (Figure 3.4), with a sunspot of unsigned flux 2.11×10^{22} Mx. We note that the measurements

here are much more noisy than those of the sunspot model (Figure 3.3), especially for the measurements between $z = -5$ to -7 Mm using annulus group 4 (Figures 3.4f,g,i,j). Additionally, the size of the detected features increase slightly in size with depth between annulus groups 4 and 5 (Figures 3.4k,l,n,o), and between annulus groups 5 and 6 (Figures 3.4p,q,s,t). As in the sunspot model, there is an offset between the location of greatest anisotropy and the maximum horizontal magnitude at the surface for annulus groups 5 (Figure 3.4n,o) and 6 (Figure 3.4s,t). Such an assessment is difficult to make for annulus group 4 considering the low SNR, though there appears to be no such offset for these measurements. There are no significant differences between the azimuth derived from the GB02 travel times (Figure 3.4f,k,p) and the Gabor wavelet travel times (Figure 3.4g,l,q). There is, however, slightly less noise in the GB02-derived measurements of the anisotropy parameter, particularly for annulus group 5 (Figure 3.4n). The feature seen in the annulus group 5 anisotropy measurements does suggest some degree of connection with the magnetic feature of opposite sign to the left of the sunspot in Figure 3.4c.

The magnetic field configuration of the sunspot associated with AR 12786 is unique, showing significant asymmetry in the magnitude and extent of the horizontal field between the North and South sectors. The field azimuth also shows a similar degree of asymmetry. AR 12786's sunspot is somewhat weaker than AR 12218's, with an unsigned magnetic flux of 1.37×10^{22} Mx. In contrast to the azimuth measurements in AR 12218, neither the GB02-derived (Figure 3.5f,k,p) nor the Gabor wavelet-derived (Figure 3.5g,l,q) are particularly well-aligned with the surface azimuth. Additionally, while ARs 12218 and 12786 have similar maximum horizontal field magnitudes, the anisotropy measured from AR 12786 is much weaker than in AR 12218.

Comparing the mean in-out travel time deviations between the two active regions (Figures 3.4h,m,r and 3.5h,m,r), we find that the magnitudes are similar,

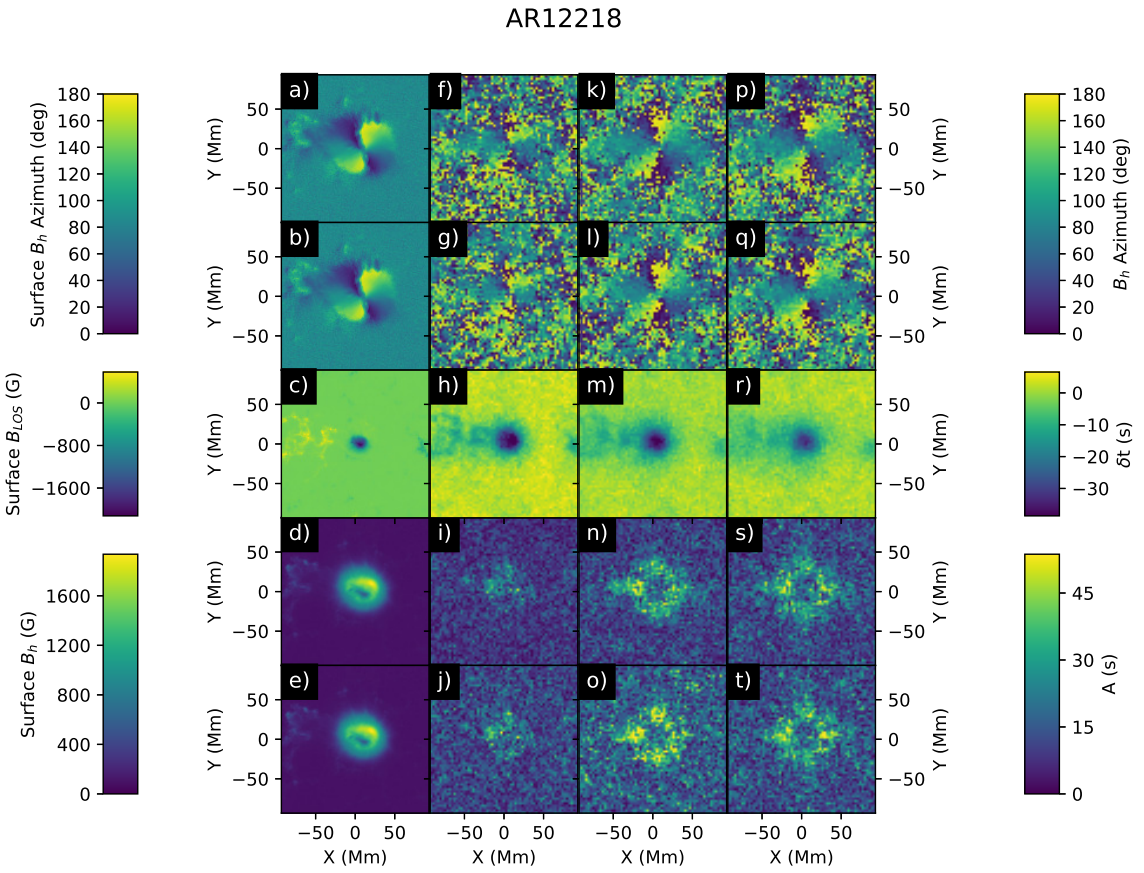

Figure 3.4 Comparison of AR 12218's surface magnetic field with measurements of the subsurface field. The active region's surface azimuth is shown in panels a and b, the line-of-sight magnetic field in panel c, and the magnitude of the horizontal surface magnetic field is shown in panels d and e. The measured subsurface azimuth is shown in rows 1 and 2 and travel time anisotropy in rows 4 and 5. Measurements in rows 1 and 4 are derived from the GB02 travel time method, and measurements in rows 2 and 5 are derived from the Gabor wavelet phase travel time method. Row 3 shows the mean in-out travel time difference, from which wave speed perturbations can be obtained through inversion. Column 2 corresponds to annulus group 4, column 3 to annulus group 5, and column 4 to annulus group 6.
Source: Stefan & Kosovichev (2022)

though the perturbation is larger for AR 12218. The mean in-out travel time deviation is produced both by sound speed perturbations and acoustic cut-off frequency perturbations, and to some extent measures changes in temperature and pressure. This, coupled with the smaller B_{LOS} feature and reduced magnitude, may indicate that the overall subsurface field is weaker in AR 12786 and therefore explains the weaker measured anisotropy. As with AR 12218, the anisotropy measurements derived

from the Gabor wavelet fitting (Figures 3.5j,o,t) are more noisy than those derived from the GB02 method (Figures 3.5i,n,s). Additionally, there is no noticeable change in the size of the anisotropy feature with increasing depth in either the GB02 or Gabor wavelet methods.

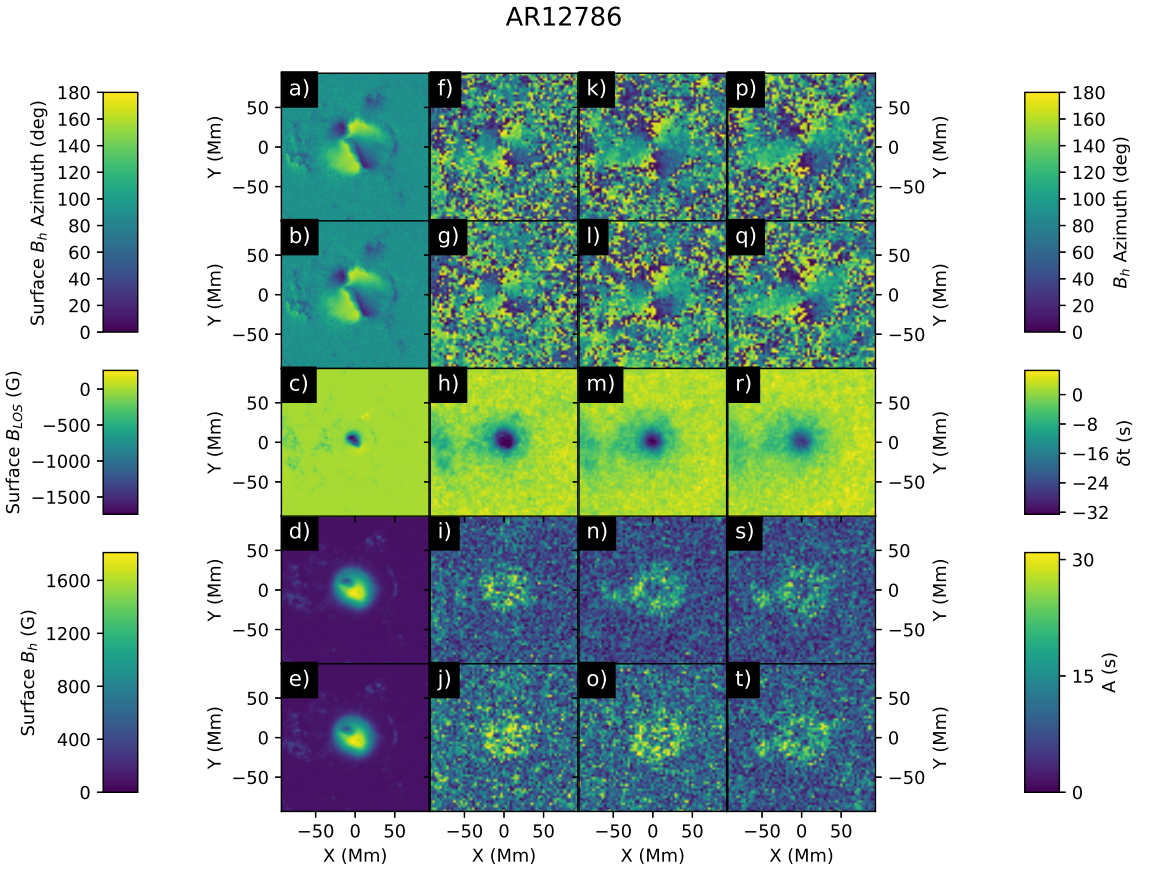

Figure 3.5 Comparison of AR 12786's surface magnetic field with measurements of the subsurface field, with the same format as Figure 3.4.
Source: Stefan & Kosovichev (2022)

The final active region we study is AR 12794, with an unsigned flux of 2.51×10^{22} Mx. This sunspot is more similar to AR 12218 than to AR 12786, with a more axisymmetric configuration of the horizontal magnetic field. The features detected in the travel time anisotropy do not appear to grow in size between annulus groups 4 (Figures 3.6i,j) and 5 (Figures 3.6n,o), and in fact, there is some contraction in size between annulus groups 5 and 6 (Figures 3.6s,t). Along with this contraction,

the magnitude of the anisotropy measured with both the Gabor wavelet and GB02 methods increases with depth. As with ARs 12218 and 12786, the GB02 travel times produce less noisy measurements than the Gabor wavelet travel times, in general, though the noise level for the two methods are similar in annulus group 6 (Figures 3.6s,t). While not completely aligned with the surface azimuth, the subsurface azimuth (Figures 3.6f,g,k,l,p,q) is reasonably well-resolved. In annulus groups 5 and 6 in particular, there appears to be a unidirectional concentration of magnetic flux in the lower left corner. This concentration is most visible in the azimuth maps for annulus group 5 (Figure 3.6k,l) and there is a corresponding, albeit weak, enhancement of the anisotropy in the same location for annulus groups 5 (Figure 3.6n,o) and 6 (Figures 3.6s,t).

We now examine how the measured anisotropy for each active region changes with depth, shown in Figure 3.7. Here, the anisotropy is averaged over an annulus with and inner radius of 10 Mm and outer radius of 30 Mm, roughly the same size and shape as the detected features. The noise floor, as indicted by the dotted lines in Figure 3.7, is computed from the weighted mean of travel time anisotropy in a quiet Sun region. The weights are the inverse chi-squared residuals for the Gabor wavelet method and the inverse of the least-squared error for the GB02 method. As seen in Figure 3.7, there is little to no similarity between the depth-dependent anisotropies in the observed active regions. The anisotropy measured in AR 12218 increases between annulus groups 4 and 5, then slightly decreases from annulus group 5 to 6. Conversely, the anisotropy measured in AR 12786 shows almost no variation with depth. Similarly for AR 12794, the anisotropy is nearly constant between annulus groups 4 and 5, and increases significantly at annulus group 6. For ARs 12218 and 12794, the variation of anisotropy with depth is greater than the noise floor, indicating a strong dependence of the anisotropy on local conditions.

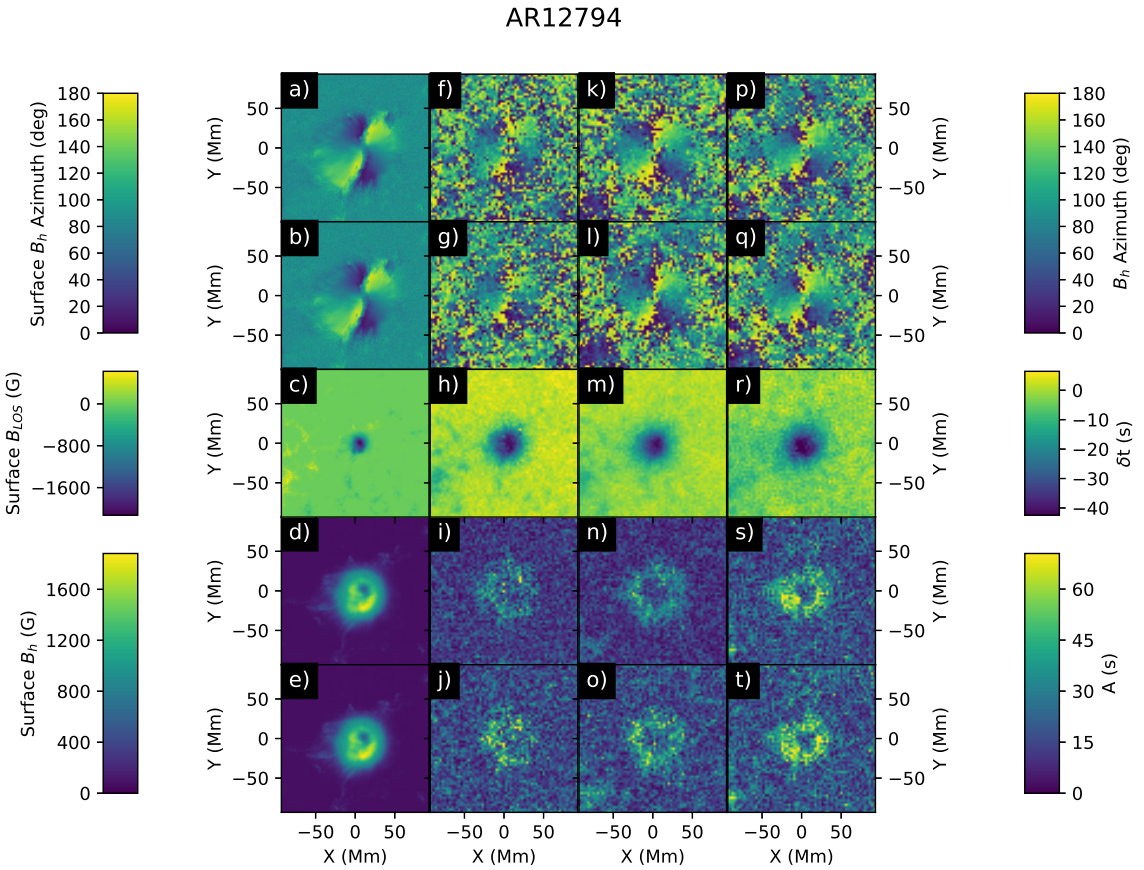

Figure 3.6 Comparison of AR 12794's surface magnetic field with measurements of the subsurface field, with the same format as Figure 3.4.
Source: Stefan & Kosovichev (2022)

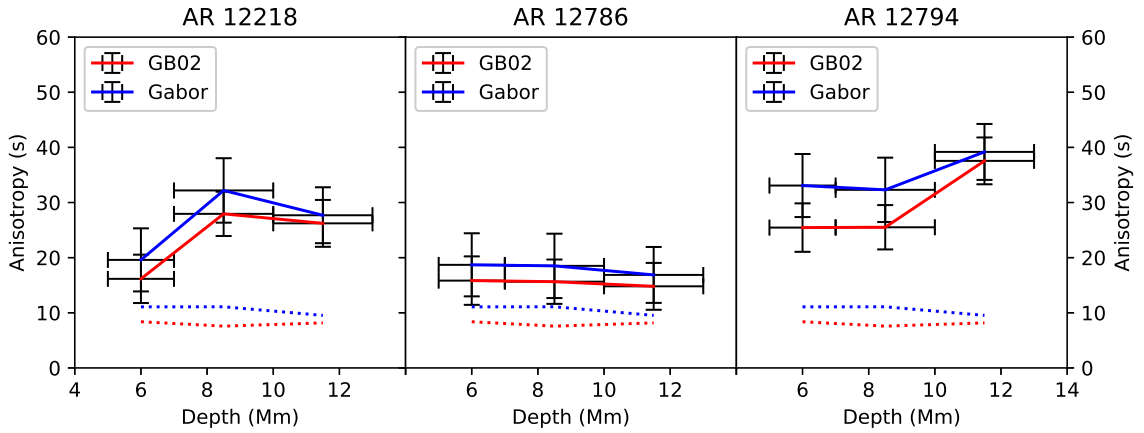

Figure 3.7 Spatially averaged anisotropy as a function of depth. The measurements from each annulus group are assumed to sample the center of the re respective depth ranges.
Source: Stefan & Kosovichev (2022)

CHAPTER 4

ACOUSTIC MODEL OF SUNQUAKE EXCITATION

4.1 Governing Equations and Methods

4.1.1 Derivation of the Governing Equations

To construct our acoustic model, we begin with the compressible form of the mass and momentum conservation equations,

$$\frac{D\rho}{Dt} + \rho\nabla \cdot \mathbf{v} = 0 \tag{4.1}$$

and

$$\rho\frac{D\mathbf{v}}{Dt} = -\nabla P + \rho\mathbf{g} + \mathbf{F}_{\text{ext}}, \tag{4.2}$$

where $\mathbf{F}_{\text{ext}}$ is the net external force and D/Dt is the material derivative, equivalent to

$$\frac{D}{Dt} = \frac{\partial}{\partial t} + \mathbf{v} \cdot \nabla, \tag{4.3}$$

which accounts for changes in time and also gradients advected by the velocity field. We assume that wavefront travels quickly enough that there is no exchange of any heat generated by compression. In other words, the wave propagation is adiabatic

such that the entropy of the system is unchanged, yielding the following condition

$$\frac{DS}{Dt} = \frac{D}{Dt}\left(\frac{P}{\rho^\gamma}\right) = 0. \tag{4.4}$$

We now consider linear perturbations to Equations (4.1), (4.2), and (4.4), with the static background state dependent only on radius: $\rho \to \rho_0(r) + \rho'(r, \vartheta, \varphi, t)$. In the unperturbed state, the plasma is in hydrostatic balance with no background flows. The plasma velocity itself is then a perturbation: $\mathbf{v} \to \mathbf{v}(r, \vartheta, \varphi, t)$. The velocity is further separated into a radial and a horizontal component, with the horizontal component contained both the $\hat{\theta}$ and $\hat{\phi}$ components. We separate the radial and angular dependence of any variable a using the spherical harmonics Y_l^m, such that

$$a(r, \vartheta, \varphi) = \sum_{l,m} a_{l,m}(r) Y_l^m(\vartheta, \varphi). \tag{4.5}$$

Starting with the mass conservation equation, Equation (4.1), each variable is expanded in terms of the background and perturbed quantities. Keeping only terms which contain at most one perturbed quantity, we have

$$\frac{\partial \rho'}{\partial t} + \mathbf{v} \cdot \nabla \rho_0 + \rho_0 \nabla \cdot \mathbf{v} = 0. \tag{4.6}$$

We now introduce the horizontal velocity $\mathbf{v_h}$, the vector component of the velocity in the $\hat{\theta}$ and $\hat{\phi}$ directions. Furthermore, we separate the radial and horizontal components of the divergence operator, such that $\nabla \cdot = \frac{1}{r^2}\frac{\partial}{\partial r} + \nabla_h \cdot$. Applying this

formulation to the above perturbed mass conservation equation yields

$$\frac{\partial \rho'}{\partial t} + v_r \frac{\partial \rho_0}{\partial r} + \rho_0 \left(\frac{1}{r^2} \frac{\partial}{\partial r} \left(r^2 v_r \right) + \frac{1}{r} \nabla_h \cdot \mathbf{v_h} \right) = 0. \tag{4.7}$$

It is convenient to choose the case where the angular dependence of the horizontal velocity can be expressed as horizontal gradients of the spherical harmonics as opposed to the spherical harmonics themselves. The horizontal velocity is then expressed as $\sum_{l,m} v_{h,l}(r,t) \nabla_{\mathbf{h}} Y_l^m(\vartheta, \varphi)$, where $\nabla_{\mathbf{h}}$ contains the angular components of the gradient and $v_{h,l} = A_l v_h$ is the scalar horizontal velocity. Expressing Equation (4.7) with all dependences, and the summation over l and m begin implicit, we have

$$\begin{aligned} \left[\frac{\partial \rho'(r,t)}{\partial t} + v_{r,l}(r,t) \frac{\partial \rho_0(r)}{\partial r} + \rho_0(r) \, \frac{1}{r^2} \frac{\partial}{\partial r} \left(r^2 v_{r,l}(r,t) \right) \right] \cdot Y_l^m(\vartheta, \varphi) \\ + \rho_0(r) \left[\frac{v_{h,l}(r,t)}{r} \right] \nabla_h^2 Y_l^m(\vartheta, \varphi) = 0. \end{aligned} \tag{4.8}$$

We restrict ourselves to the situation where any provided excitation mechanism is azimuthally symmetric. In this case, we can place the excitation over the pole at $\vartheta = 0$ such that wave propagation is also azimuthally symmetric and there is no longer any dependence on φ. The spherical harmonics then reduce to the ordinary Legendre polynomials $P_l(\cos\vartheta)$, which satisfies $\nabla_h^2 P_l = -L^2 P_l = -l(l+1) P_l$ for positive integer l. The angular derivatives can then be spectrally computed via the previous relationship rather than being explicitly computed with finite differences. Keeping the shorthand from the horizontal velocity, we express any variable x with its associated Legendre coefficient A_l as x_l, where $x_l = A_l x$. The linearized mass

conservation equation can finally be reduced to

$$\frac{\partial \bar{\rho}_l}{\partial t} + v_{r,l}\frac{\partial \ln \rho_0}{\partial r} + \frac{1}{r^2}\frac{\partial}{\partial r}\left(r^2 v_{r,l}\right) - \frac{L^2}{r}v_{h,l} = 0, \tag{4.9}$$

where $\bar{\rho} = \rho'/\rho_0$ is the normalized perturbation to density.

Moving now to the adiabatic condition (Equation (4.4)), we expand the material derivative and express the variables in terms of their background and perturbed quantities

$$\frac{1}{\gamma P_0}\left[\frac{\partial P'}{\partial t} + \mathbf{v}\cdot\nabla P_0 + \mathbf{v}\cdot\nabla P'\right] = \frac{1}{\rho_0}\left[\frac{\partial \rho'}{\partial t} + \mathbf{v}\cdot\nabla\rho_0 + \mathbf{v}\cdot\nabla\rho'\right]. \tag{4.10}$$

Since, in general, $P' \ll P_0$ and $\rho' \ll \rho_0$, we make the approximations $1/\gamma(P_0 + P') \approx 1/\gamma P_0$ and $1/(\rho_0 + \rho') \approx 1/\rho_0$. Removing the non-linear terms gives

$$\frac{1}{\gamma P_0}\frac{\partial P'}{\partial t} + v_r\left(\frac{1}{\gamma P_0}\frac{\partial P_0}{\partial r} - \frac{1}{\rho_0}\frac{\partial \rho_0}{\partial r}\right) = \frac{1}{\rho_0}\frac{\partial \rho'}{\partial t}. \tag{4.11}$$

An important parameter lies within Equation ((4.11)), the Brunt-Väisälä frequency (N), or buoyancy frequency (Vallis, 2006), which is defined as

$$N^2 = g\left(\frac{1}{\gamma P_0}\frac{\partial P_0}{\partial r} - \frac{1}{\rho_0}\frac{\partial \rho_0}{\partial r}\right). \tag{4.12}$$

The stability and frequency of g-modes is determined by the buoyancy frequency, which is real-valued in the solar core and is expected to produce stable g-modes. In the convective zone, however, this frequency is imaginary which indicates an unstable density-pressure stratification. Since our simulation does not include a detailed model for heat transport, we are unable to counteract the runaway convection caused by this stratification, and instead set N^2 to be zero where it would otherwise be negative. Making the buoyancy frequency substitution in Equation (4.11), we have

$$\frac{1}{\gamma}\frac{\partial \bar{P}}{\partial t} + v_r \frac{N^2}{g} = \frac{\partial \bar{\rho}}{\partial t}, \tag{4.13}$$

where $\bar{P} = P'/P_0$ is the normalized perturbation to pressure. Substituting the time derivative of the normalized density from Equation (4.9) along with the Legendre polynomials, we arrive at the final form for the pressure equation,

$$\frac{\partial \bar{P}_l}{\partial t} + \gamma \left[v_{r,l} \left(\frac{N^2}{g} + \frac{\partial \ln \rho_0}{\partial r} \right) + \frac{1}{r^2}\frac{\partial}{\partial r}\left(r^2 v_{r,l}\right) - \frac{L^2}{r} v_{h,l} \right] = 0. \tag{4.14}$$

We now separate the radial and horizontal components of the momentum equation and perform the same linearization and spherical harmonic expansion as in Equations (4.9) and (4.14). Applying this to the radial momentum equation, we have

$$\rho_0 \frac{\partial v_r}{\partial t} = -\frac{\partial P_0}{\partial r} - \frac{\partial P'}{\partial r} + \rho_0 g + \rho' g + F_{\text{ext},r}. \tag{4.15}$$

The background state is assumed to be in hydrostatic equilibrium, such that the relation $\partial P_0/\partial r + \rho_0 g = 0$ is satisfied, and the corresponding terms are removed from the equation. We isolate the time derivative by dividing by ρ_0, and substituting the Legendre polynomials yields

$$\frac{\partial v_{r,l}}{\partial t} = -\frac{1}{\rho_0}\frac{\partial P'_l}{\partial r} + \bar{\rho}_l g + \frac{F_{\text{ext},r,l}}{\rho_0}. \tag{4.16}$$

The linearized form of the horizontal momentum equation is

$$\rho_0 \frac{\partial v_h}{\partial t} = \frac{1}{r}\nabla_h P' + F_{\text{ext},h}. \tag{4.17}$$

Here, the radial and horizontal dependence of P' can be separated with the Legendre polynomials as $P' = \sum_l P'_l(r) P_l(\vartheta)$. The horizontal gradient ∇_h does not affect P'_l and instead is applied to the Legendre polynomial. Assuming that the horizontal component of the external forces can also be decomposed into the horizontal gradient of Legendre polynomials, $F_{\text{ext},h} = \sum_l F_{\text{ext},h,l}(r,t)\nabla_h P_l(\vartheta)$, each term in the horizontal momentum then contains $\nabla_h P_l$ which can be neglected. The final form for the horizontal momentum equation, obtained by again dividing through by ρ_0, is

$$\frac{\partial v_{h,l}}{\partial t} = \frac{P'_l}{r\rho_0} + \frac{F_{\text{ext},h,l}}{\rho_0}. \tag{4.18}$$

Together, the system of equations solved in our model is

$$\begin{cases} \dfrac{\partial \bar{\rho}_l}{\partial t} + v_{r,l}\dfrac{\partial \ln \rho_0}{\partial r} + \dfrac{1}{r^2}\dfrac{\partial}{\partial r}\left(r^2 v_{r,l}\right) - \dfrac{L^2}{r} v_{h,l} = 0 \\ \dfrac{\partial \bar{P}_l}{\partial t} + \gamma\left[v_{r,l}\left(\dfrac{N^2}{g} + \dfrac{\partial \ln \rho_0}{\partial r}\right) + \dfrac{1}{r^2}\dfrac{\partial}{\partial r}\left(r^2 v_{r,l}\right) - \dfrac{L^2}{r} v_{h,l}\right] = 0 \\ \dfrac{\partial v_{r,l}}{\partial t} = -\dfrac{1}{\rho_0}\dfrac{\partial P'_l}{\partial r} + \bar{\rho}_l g + \dfrac{F_{ext,r,l}}{\rho_0} \\ \dfrac{\partial v_{h,l}}{\partial t} = \dfrac{P'_l}{r\rho_0} + \dfrac{F_{ext,h,l}}{\rho_0} \end{cases} . \tag{4.19}$$

4.1.2 Boundary Conditions

In the Sun, acoustic waves with frequency equal to or greater than the acoustic cut-off frequency, ω_c, travel beyond the surface and are mostly damped in the atmosphere (Christensen-Dalsgaard, 2002). Waves which have frequency less than the acoustic cut-off frequency are reflected near the surface and are trapped in the interior. It is necessary to choose our boundary conditions carefully so that this selective resonance is replicated in our model, otherwise high frequency oscillations will reflect off of the upper boundary. To this end, we derive non-reflecting boundary conditions through an eigendecomposition of the matrix representation of the system's radial derivatives, $B = Q\Lambda Q^{-1}$.

We consider only Equations (4.14) and (4.16) to simplify calculations, as ρ' can be derived from P' via Equation (4.4) and Equation (4.18) has no radial derivatives. The matrix form of this reduced system is

$$A\frac{\partial \mathbf{X}}{\partial t} + B\frac{\partial \mathbf{X}}{\partial r} = \mathbf{C}, \tag{4.20}$$

where A is the matrix of time derivative coefficients, $\mathbf{X} = [P_l', v_{r,l}]^T$ are the relevant variables, and $\mathbf{C}$ is the vector containing any non-derivative terms. We use the form of Equation (4.14) where the pressure perturbations are not normalized such that the matrix A is simply the identity matrix. The matrix containing the radial derivatives is

$$B = \begin{bmatrix} 0 & \gamma P_0 \\ \dfrac{1}{\rho_0} & 0 \end{bmatrix}, \tag{4.21}$$

with eigenvalues $\lambda_+ = +c_s$ and $\lambda_- = -c_s$, where $c_s = \sqrt{\gamma P_0/\rho_0}$ is the adiabatic sound speed, corresponding to outward and inward propagating waves, respectively. Using these eigenvalues, we obtain the following decomposition for the system

$$B = Q\Lambda Q^{-1} = \frac{1}{2}\begin{bmatrix} \rho_0 c_s & -1 \\ 1 & \dfrac{c_s}{\gamma P_0} \end{bmatrix}\begin{bmatrix} +c_s & 0 \\ 0 & -c_s \end{bmatrix}\begin{bmatrix} \dfrac{c_s}{\gamma P_0} & 1 \\ -1 & \rho_0 c_s \end{bmatrix}. \tag{4.22}$$

Keeping track of terms associated with λ_- during the matrix multiplication enables us to determine the derivatives corresponding to the inward propagating waves. We enforce hydrostatic equilibrium for the inward propagating terms, such that $\partial P_l'/\partial r] = -\rho' g$ and $[\partial v_{r,l}/\partial r] = 0$, while outward propagating waves travel as

normal. The system of equations solved at the upper boundary $R = R_{\max}$ is

$$\begin{cases} \dfrac{\partial \bar{\rho}_l}{\partial t} + v_{r,l}\left(\dfrac{\partial \ln \rho_0}{\partial r} + \dfrac{2}{r}\right) - \dfrac{L^2}{r} v_{h,l} + \dfrac{1}{2}\left(c_s \dfrac{\partial \bar{\rho}_l}{\partial r} + \dfrac{\partial v_{r,l}}{\partial r} + \dfrac{\bar{\rho}_l g}{c_s}\right) = 0 \\ \dfrac{\partial \bar{P'}_l}{\partial t} + \gamma\left(v_{r,l}\dfrac{\partial \ln \rho_0}{\partial r} + v_{r,l}\dfrac{N^2}{g} - \dfrac{L^2}{r} v_{h,l}\right) \\ \qquad\qquad + \dfrac{1}{2}\left(c_s \dfrac{\partial \bar{\rho}_l}{\partial r} + \dfrac{\partial v_{r,l}}{\partial r} + \dfrac{\bar{\rho}_l g}{c_s}\right) = 0 \\ \dfrac{\partial v_{r,l}}{\partial t} + \bar{\rho}_l g + \dfrac{1}{2}\left(c_s^2 \dfrac{\partial \bar{\rho}_l}{\partial r} + c_s \dfrac{\partial v_{r,l}}{\partial r} - \bar{\rho}_l g\right) = 0 \\ \dfrac{\partial v_{h,l}}{\partial t} + \dfrac{P'_l}{r\rho_0} = 0 \end{cases}, \tag{4.23}$$

where we use the substitution $P'_l = c_s^2 \rho'_l$.

4.1.3 Numerics

We solve the governing equations along a radial mesh which contains values for radius, the unperturbed pressure and density, adiabatic exponent, and gravitational acceleration. The background model is derived from the Standard Solar Model (Christensen-Dalsgaard et al., 1996) which is computed up to $r = 696.841$ Mm. The time derivatives are approximated by a simple first-order forward difference

$$\frac{\partial y}{\partial t} \approx \frac{y_i^{n+1} - y_i^n}{\tau}, \tag{4.24}$$

where τ is the time step. The time step is chosen to satisfy the CFL condition (Courant et al., 1967) $\tau_{CFL} \leq \min[\Delta r / c_s]$, the travel time for an acoustic wave between the smallest grid-point separation Δr with speed c_s. Here, we choose $\tau = 0.6\tau_{CFL}$ to ensure stability.

The radial derivatives are evaluated using a fourth-order central difference, with the following form on a uniform grid

$$\frac{\partial f}{\partial r}(t = t_n, r = r_i) \approx \frac{f^n_{i-2} - 8f^n_{i-1} + 8f^n_{i+1} - f^n_{i+2}}{12\Delta r}. \tag{4.25}$$

However, the grid we use is not uniform in radius, and the appropriate form of the difference is derived in Appendix B. Additionally, we use a staggered mesh scheme, where the horizontal velocity, pressure, and density variables are placed on body points and the radial velocity variable placed on edge points located halfway between neighboring body points; i.e. given r_b as the radius of the body point and r_e as the radius of the edge point, $r_{b,i} < r_{e,i} < r_{b,i+1}$. For each time step, the density and pressure are computed first, then the radial and horizontal velocities using the updated values for pressure and density. The variables are linearly interpolated where they need to be explicitly evaluated, as opposed to the radial derivatives. For example, the radial velocity is linearly interpolated from neighboring edge points to be used in Equation (4.14) at a body point.

At the upper boundary's body point, the radial velocity is computed using a second-order central difference, since edge points exist both above and below the body point. For a non-uniform grid, this central difference has the form

$$\frac{\partial f}{\partial r}(t = t_n, r = r_i) \approx \frac{f^n_{i+1} - f^n_{i-1}}{\Delta r_{i+1} + \Delta r_{i-1}}. \tag{4.26}$$

For the perturbed density radial derivative to be evaluated at the upper boundary's edge point, a ghost point is implemented above the edge point so that the central difference in Equation (4.26) can be used. The perturbed pressure and density at the

ghost body point are evolved in time with the boundary conditions, and the radial derivative is evaluated with a second-order one-sided difference of the form

$$\frac{\partial f}{\partial r}(t = t_n, r = r_i) \approx \frac{3f_i^n - 4f_{i-1}^n + f_{i-2}^n}{2\Delta x}. \tag{4.27}$$

Here, we've chosen the grid spacing to be uniform and the above formulation does not need to be adjusted.

The discretized governing equations and accompanying algorithm are written in Fortran, and parallelized using the MPI (Message-Passing Interface) library. The code can be run on an arbitrary number of CPUs, taking approximately four minutes per angular degree l for one hour of solar time. We compute solutions to the governing equations up to angular degree $l = 6000$. This corresponds to a smallest resolvable distance of 0.36 Mm in the $\hat{\theta}$-direction, approximately twice the resolution of HMI measurements. The data are stored as functions of radius, time, and angular degree l, which allows for damping of individual wavenumbers to reproduce the damping seen on the Sun, as described in the following Subsection 4.1.5.

4.1.4 Stability Analysis of the Finite-Difference Method

Keeping in mind that half-grid variables are interpolated onto a given grid point, i.e.

$$v_{r,i}^n = v_{r,i-\frac{1}{2}}^n + \frac{v_{r,i+\frac{1}{2}}^n - v_{r,i-\frac{1}{2}}^n}{\Delta r_i}\frac{\Delta r_i}{2} = v_{r,i-\frac{1}{2}}^n + \frac{v_{r,i+\frac{1}{2}}^n - v_{r,i-\frac{1}{2}}^n}{2}, \tag{4.28}$$

we express the discretized governing equations in terms of each variables associated error, denoted by the symbol, as

$$\begin{cases} v_{h,i}^{n+1} = v_{h,i}^{n} - \dfrac{\Delta t}{r\rho_0} P_i^{n+1} \\ \dfrac{\rho_i^{n+1} - \rho_i^n}{\Delta t} = -\dfrac{1}{2} x_1 \left(v_{r,i+\frac{1}{2}}^n + v_{r,i-\frac{1}{2}}^n \right) - \dfrac{1}{12\Delta r} \left(v_{r,i-\frac{3}{2}}^n \right. \\ \qquad\qquad \left. -8v_{r,i-\frac{1}{2}}^n + 8v_{r,i+\frac{1}{2}}^n - v_{r,i+\frac{3}{2}}^n \right) + \dfrac{L^2}{r} v_{h,i}^n \\ \dfrac{v_{r,i}^{n+1} - v_{r,i}^n}{\Delta t} = -\dfrac{1}{12\rho_0 \Delta r} \left(P_{i-\frac{3}{2}}^{n+1} - 8P_{i-\frac{1}{2}}^{n+1} + 8P_{i+\frac{1}{2}}^{n+1} \right. \\ \qquad\qquad \left. - P_{i+\frac{3}{2}}^{n+1} \right) + \dfrac{1}{2} \left(\bar{\rho}_{i-\frac{1}{2}}^{n+1} + \bar{\rho}_{i+\frac{1}{2}}^{n+1} \right) g \\ \dfrac{P_i^{n+1} - P_i^n}{\Delta t} = \gamma P_0 \left[-\dfrac{1}{2} \left(v_{r,i+\frac{1}{2}}^n + v_{r,i-\frac{1}{2}}^n \right) x_2 - \dfrac{1}{12\Delta r} \left(v_{r,i-\frac{3}{2}}^n \right. \right. \\ \qquad\qquad \left. \left. -8v_{r,i-\frac{1}{2}}^n + 8v_{r,i+\frac{1}{2}}^n - v_{r,i+\frac{3}{2}}^n \right) + \dfrac{L^2}{r} v_{h,i}^n \right] \end{cases}, \quad (4.29)$$

where we have defined $x_1 = \partial \ln \rho_0 / \partial r + 2/r$ and $x_2 = x_1 + N^2/g$ for convenience. For simplicity, we've assumed the case of a uniform grid; to ensure stability for our non-uniform grid, we will evaluate the stability criteria for several grid spacings. The error associated with a particular variable can be expressed in terms of the corresponding Fourier components; for example, v_h can be expressed as

$$v_{h,i}^n = \sum_m D_m e^{a_m t_n} e^{i k_m r_i}, \quad (4.30)$$

where D_m is the error amplitude of the m^{th} mode, k_m is the m^{th} wavenumber of the error's propagation in the radial direction, a_m is the corresponding growth rate of the error. The errors associated with $\bar{\rho}$, P', and v_r can be expressed similarly with coefficients A, B, and C, respectively. Considering a particular Fourier mode and

dividing through by $e^{ikr_i}e^{at_n}$, where we drop the subscript m, we have

$$\begin{cases} GD = D - G\dfrac{\Delta t B}{r\rho_0} \\ GA = A + \Delta t\left[-\dfrac{C}{2}x_1\left(e^{\frac{ik\Delta r}{2}} + e^{-\frac{ik\Delta r}{2}}\right) - \dfrac{C}{12\Delta r}\left(e^{-\frac{3ik\Delta r}{2}} - 8e^{-\frac{ik\Delta r}{2}}\right.\right. \\ \qquad\qquad \left.\left. + 8e^{\frac{ik\Delta r}{2}} - e^{\frac{3ik\Delta r}{2}}\right) + \dfrac{DL^2}{r}\right] \\ GC = C + G\Delta t\left[-\dfrac{B}{12\rho_0\Delta r}\left(e^{-\frac{3ik\Delta r}{2}} - 8e^{-\frac{ik\Delta r}{2}} + 8e^{\frac{ik\Delta r}{2}} - e^{\frac{3ik\Delta r}{2}}\right)\right. \\ \qquad\qquad \left. + \dfrac{A}{2}\left(e^{\frac{ik\Delta r}{2}} + e^{-\frac{ik\Delta r}{2}}\right)g\right] \\ GB = B + \Delta t\gamma P_0\left[-\dfrac{C}{2}\left(e^{\frac{ik\Delta r}{2}} + e^{-\frac{ik\Delta r}{2}}\right)x_2 - \dfrac{C}{12\Delta r}\left(e^{-\frac{3ik\Delta r}{2}} - 8e^{-\frac{ik\Delta r}{2}}\right.\right. \\ \qquad\qquad \left.\left. + 8e^{\frac{ik\Delta r}{2}} - e^{\frac{3ik\Delta r}{2}}\right) + \dfrac{DL^2}{r}\right] \end{cases} . \quad (4.31)$$

Here, $G = e^{a(t_{n+1}-t_n)}$ is the growth factor of the error between successive time steps, which we've assumed to be the same for each variable. The assumption of identical error growth rates is justified since our system of equations is coupled.

For convenience, we define the following variables

$$x_3 = \frac{1}{2}\left(e^{\frac{ik\Delta r}{2}} + e^{-\frac{ik\Delta r}{2}}\right) = \cos\left(\frac{k\Delta r}{2}\right) \quad (4.32)$$

and

$$\begin{aligned} x_4 &= \frac{1}{12}\left(e^{-\frac{3ik\Delta r}{2}} - 8e^{-\frac{ik\Delta r}{2}} + 8e^{\frac{ik\Delta r}{2}} - e^{\frac{3ik\Delta r}{2}}\right) \\ &= \frac{i}{6}\left(8\sin\left(\frac{k\Delta r}{2}\right) - \sin\left(\frac{3k\Delta r}{2}\right)\right). \end{aligned} \quad (4.33)$$

We will evaluate the stability at the shortest wavelength, $\lambda = 2\Delta r$, $k = \pi/\Delta r$, which is generally the most unstable mode; substituting this value for k yields $x_3 = 0$ and $x_4 = 3i/2$. It is beneficial to express the stability of the system in terms of dimensionless parameters, and we begin this process by defining new Fourier amplitudes A', B', C', and D', given by

$$\begin{cases} A' = Ac \\ B' = \dfrac{B}{\rho_0 c} \\ C' = C \\ D' = D \end{cases} . \tag{4.34}$$

The corresponding dimensionless parameters the system will be expressed in are

$$\begin{cases} N_c = \dfrac{c\Delta t}{\Delta r} \\ N_s = \dfrac{c\Delta t}{r} \\ N_g = \dfrac{g\Delta t}{c} \\ N_\rho = \dfrac{c\Delta t}{H_\rho} = -c\Delta t \dfrac{\partial \ln \rho_0}{\partial r} \\ N_N = \dfrac{c\Delta t N^2}{g} \end{cases} . \tag{4.35}$$

Here, N_c is the Courant number (Courant et al., 1967), the ratio between the time step and the travel time of a wave passing between two grid points. N_s is the ratio of a radially propagating wave's travel distance and its radial position. The quantity N_s multiplied by L^2, which appears in some of the error equations, describes a similar ratio but for horizontally propagating waves. N_g is the ratio between the

change in velocity experienced by a fluid element due to gravity in unit time and the sound speed. N_ρ is the ratio of the travel distance of a radially propagating wave relative to the density scale height, and N_N is a stability parameter for gravity waves.

Starting with the perturbed density's error and multiplying everywhere by c, we recover

$$\begin{aligned} c\left[GA = A - \Delta t x_1 x_3 C - \frac{\Delta t}{\Delta r} C x_4 + \frac{\Delta t L^2}{r} D\right] \\ GA' = A' - \left(2\frac{c\Delta t}{r} - \frac{c\Delta t}{H_\rho}\right) C x_3 - \frac{c\Delta t}{\Delta r} C x_4 + \frac{c\Delta t}{r} L^2 D \ . \\ \boxed{GA' = A' - (2N_s - N_\rho)\, C x_3 - N_c C x_4 + N_s L^2 D} \end{aligned} \tag{4.36}$$

Multiplying everywhere in the perturbed pressure error equation by $1/\rho_0 c$, we have

$$\begin{aligned} \frac{1}{\rho_0 c}\left[GB = B - \gamma P_0 \Delta t x_2 x_3 C - \gamma P_0 \frac{\Delta t}{\Delta r} x_4 C + \gamma P_0 \frac{\Delta t}{r} L^2 D\right] \\ GB' = B' - c\Delta t \left(\frac{2}{r} - \frac{1}{H_\rho} + \frac{N^2}{g}\right) x_3 C - \frac{c\Delta t}{\Delta r} x_4 C + \frac{c\Delta t}{r} L^2 D \ . \\ \boxed{GB' = B' - (2N_s - N_\rho + N_N)\, x_3 C - N_c x_4 C + N_s L^2 D} \end{aligned} \tag{4.37}$$

Finally, substituting the new Fourier coefficients A' and B' into the radial and horizontal momentum error equations yields

$$\begin{aligned} GC = C - \frac{G}{\rho_0}\frac{\Delta t}{\Delta r} x_4 B - G x_3 g \Delta t A \\ GC = C - G\frac{c\Delta t}{\Delta r} x_4 B' - G\frac{g\Delta t}{c} x_3 A' \\ \boxed{G\left(C + N_c x_4 B' + N_g x_3 A'\right) = C} \end{aligned} \tag{4.38}$$

and

$$\begin{aligned} GD &= D - G\frac{\Delta t}{r}\frac{1}{\rho_0}B \\ GD &= D - G\frac{\Delta t}{r}\frac{1}{c}B' \quad . \\ \boxed{G\left(D + N_s B'\right) = D} & \end{aligned} \tag{4.39}$$

The above derived conditions form a matrix equation $GY\mathbf{x} = Z\mathbf{x}$, or

$$\begin{aligned} & G\begin{bmatrix} 1 & 0 & 0 & 0 \\ 0 & 1 & 0 & 0 \\ x_3 N_g & x_4 N_c & 1 & 0 \\ 0 & N_s & 0 & 1 \end{bmatrix}\begin{bmatrix} A' \\ B' \\ C \\ D \end{bmatrix} \\ = & \begin{bmatrix} 1 & 0 & -\left(2N_s - N_\rho\right)x_3 - x_4 N_c & L^2 N_s \\ 0 & 1 & -\left(2N_s - N_\rho + N_N\right)x_3 - x_4 N_c & L^2 N_s \\ 0 & 0 & 1 & 0 \\ 0 & 0 & 0 & 1 \end{bmatrix}\begin{bmatrix} A' \\ B' \\ C \\ D \end{bmatrix} \quad . \end{aligned} \tag{4.40}$$

The above system can be solved for G, the error growth factor, where we find the amplitudes are bounded by 1 for all angular degrees up to $l = 6000$. Figures 4.1 (a,b,c), (d,e,f), and (g,h,i) show how the error growth factors change with the Courant number for $l = 0$, $l = 100$, and $l = 1000$ respectively. The dimensionless parameters are evaluated based on local values, for $r = 562$ Mm (Figures 4.1 a,d,g), $r = 673$ Mm (Figures 4.1 b,e,h), and $r = 696$ Mm (Figures 4.1 c,f,i). Though it would appear that the $l = 1000$ mode is unstable at $r = 562$ Mm for the Courant number used in our simulations, $N_c = 0.6$, this instability is physical and not numerical. Oscillations with

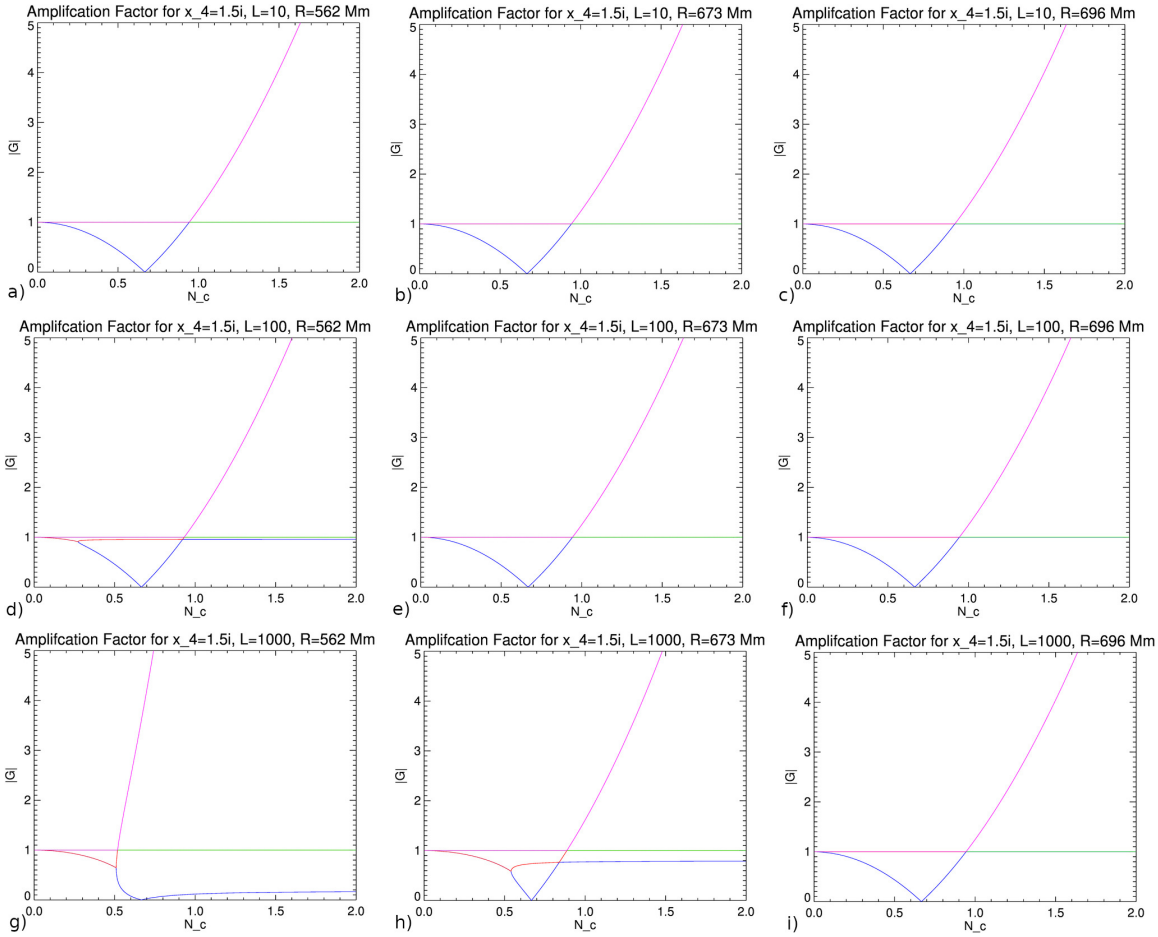

Figure 4.1 Amplitude of the error growth factors for our governing equations, for $l = 0$ at $r = 562$ Mm (a), at $r = 673$ Mm (b), and at $r = 696$ Mm (c); for $l = 100$ at $r = 562$ Mm (d), at $r = 673$ Mm (e), and at $r = 696$ Mm (f); for $l = 1000$ at $r = 562$ Mm (g), at $r = 673$ Mm (h), and at $r = 696$ Mm (i).
Source: Stefan & Kosovichev (2020)

this high of angular degree do not penetrate very deeply, and in fact the $l = 1000$ mode has a lower turning point at $r = 664$ Mm, well above $r = 562$ Mm. In other words, we require only that our system of equations is stable for a given angular degree in its region of propagation, which is indeed true. Below the lower turning point and outside the propagation region, all perturbations for a particular angular degree are identically zero.

4.1.5 Damping by Wavenumber

We have so far neglected the effects of viscous damping, as the plasma viscosity depends strongly on degree of ionization, magnetic field strength, and temperature (Vranjes, 2014). Instead, we apply exponential damping over each angular degree with appropriate parameters derived from observation. We will assume that the time dependence of an acoustic wave traveling with frequency ω_0 has the form $\Psi(t) = A\exp[i\omega_0 t]\exp[-\alpha_l t]$, where α_l is the l-dependent damping parameter. Any wave is expected to have a wavenumber-dependent rate of damping in a dispersive medium, and the angular degree and wavenumber are closely related by $k_h = \sqrt{l(l+1)}/r$. We've chosen to express the damping parameter as a function of angular degree l as the governing equations are expressed similarly.

The power spectrum, evaluated at a particular wavenumber, is dependent on frequency as

$$P = \frac{A}{4\pi^2}\frac{1}{(\omega_0-\omega)^2+\alpha_l^2}, \tag{4.41}$$

and the power is maximized at frequency ω_0 such that $P_{\max} = A/(4\pi^2\alpha_l^2)$. Substituting the upper frequency corresponding to the half-maximum $P_{\max}/2$ into the above equation, where the full-width half-maximum is given by $FWHM = 2(\omega_0 - \omega_+$ with ω_+ as the upper frequency, the damping parameter can be found as $\alpha_l = (1/2)(FWHM)$. We assume that the damping time varies as a power law with angular degree l, as

$$\tau_l = \tau^\star\left(\frac{l}{l^\star}\right)^\gamma, \tag{4.42}$$

where $\tau^\star$ is the damping time associated with the base angular degree $l^\star$, and γ is the power law exponent derived from observations.

We consider three different damping scenarios: quiet Sun damping, active region damping, and no damping. For quiet Sun damping, we use p-mode data made available by Rhodes et al. (2011), which is obtained from the azimuthally-averaged power spectrum of a three-day full-disk Dopplergram series. The damping times are derived from the provided FWHMs and fit to a power law using a least-squares algorithm. We find $\gamma = -0.723$, and the damping time associated with the chosen base angular degree $l = 1000$ is 643 seconds. For the active region damping scenario, we compute a power spectrum from a three-hour Dopplergram series of AR 11598 (Figure 4.2a) from which the damping time of the $l = 800$ mode is computed. We choose the base angular degree of $l = 800$ here instead of $l = 1000$ as the latter mode is not well-resolved in the power spectrum. We find two discernible peaks in the power spectrum at $l = 800$ (Figure 4.2b), and a Gaussian fit yields damping times of 408 seconds and 422 seconds for the first and second peaks, respectively. We use the average, 415 seconds, as the corresponding damping time $\tau^\star$ of the base angular degree. The damping is applied to the simulated radial velocity, which is stored as a function of angular degree l, before applying the Legendre transformation to return the data as a function of angular distance ϑ.

4.2 Analysis of Observed Sunquake Events

4.2.1 Form of the Simulated Excitation Mechanisms

Here, we consider two types of excitations, an instantaneous transfer of momentum and an applied external force. The momentum excitation is time-independent, whereas the external force excitations are time-dependent to simulate more gradual processes. Both excitation mechanisms are directed in the downward radial direction with Gaussian radial and angular dependences. The applied external force has

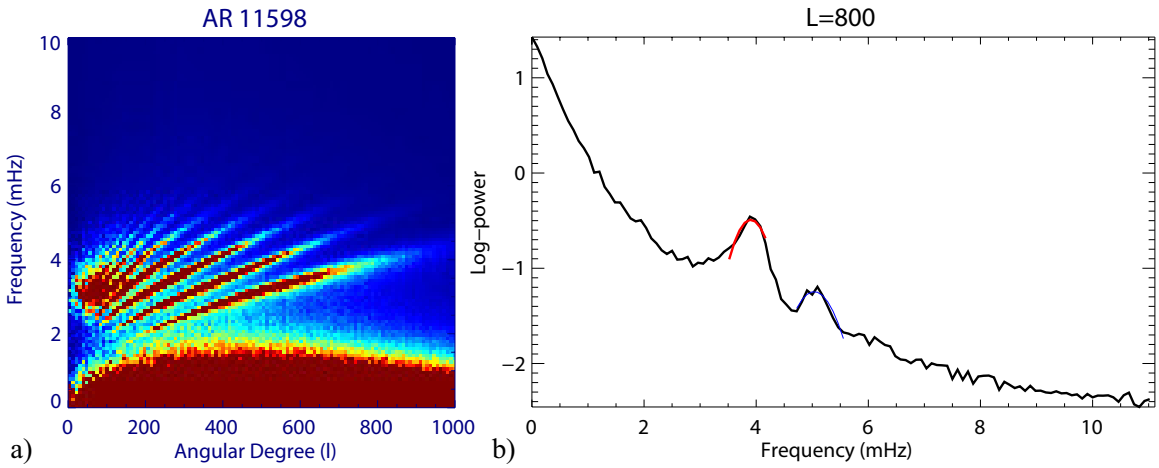

Figure 4.2 (a) Power spectrum obtained from the Dopplergram series of AR 11598. Redder colors indicate greater power, bluer colors indicate lesser power. (b) Power spectrum of angular degree $l = 800$. The first peak (in red) corresponds to $\tau_{800} = 408$ seconds, and the second peak (in blue) corresponds to $\tau_{800} = 422$ seconds.
Source: Stefan & Kosovichev (2020)

Gaussian time-dependence and is expressed per unit volume with the form

$$F_r(r, \vartheta, t) = A \exp\left[-\frac{(r - r_0)^2}{2\sigma_r^2}\right] \exp\left[-\frac{\vartheta^2}{2\sigma_\vartheta^2}\right] \cdot \exp\left[-\frac{(t - t_0)^2}{2\sigma_t^2}\right], \tag{4.43}$$

with r_0 as the radial center of the source, $t_0 = T/2$ is the mid-time of the total source duration, and σ_r, σ_ϑ, and σ_t are the Gaussian widths for the radial, angular, and time dependence, respectively. The amplitude of the force density A is arbitrary as the model is linear, though it must be negative for it be downard-directed, and we choose $A = -0.001$ dyn cm^{-3}. The transfer of momentum is modeled as an initial condition expressed as

$$v_r\left(r, \vartheta, 0\right) = \frac{A}{\rho_0\left(r\right)} \exp\left[-\frac{(r - r_0)^2}{2\sigma_r^2}\right] \exp\left[-\frac{\vartheta^2}{2\sigma_\vartheta^2}\right]. \tag{4.44}$$

As with the applied force, the amplitude of the momentum excitation is arbitrary, though we choose the momentum density to be $A = -\rho_0(r) \times 10^4$ g cm^{-2} s^{-1} so that the initial velocity at the center of the source is 100 m s^{-1}. Here, $\rho_0(r)$ is the background density. The horizontal Gaussian width is fixed at $\sigma_\vartheta = 8.6 \times 10^{-4}$ radians corresponding to a circular area on the surface of radius 0.6 Mm, and the radial Gaussian width is $\sigma_r = 0.2$ Mm.

4.2.2 Differences Between Momentum and Force Mechanisms

We find that the appearance of two mechanisms' wave fronts in time-distance diagrams are completely distinct (Figure 4.3). The time-distance diagram displays the radial velocity as a function of horizontal distance on the x-axis and time on the y-axis; for time-distance diagrams derived from observations, the line-of-sight velocity is used and azimuthally-averaged about the source location. For this comparison, the force and momentum excitations are centered approximately 100 km above the photosphere at $R = 696.119$ Mm. The first bounce wave front appears to have a longer duration than the momentum excitation by around five minutes and has a more complicated structure.

In both undamped time-distance diagrams, we are able to identify three different modes of wave propagation: pressure waves, or p-modes; the f-mode; and atmospheric acoustic-gravity waves. The p-modes (indicated by the red arrows in Figure 4.3d) form the main wavepacket of a sunquake, and these waves travel downwards before reflecting off the sound speed gradient and returning to the surface. The f-mode (indicated by the magenta arrow in Figure 4.3d) is a surface traveling wave whose dispersion relation occupies the intermediate space between p-modes and gravity waves in the solar power spectrum and is regularly observed on the Sun (Singh et al., 2016). The f-mode is characterized by its distinctive discontinuous ridge pattern and a phase velocity exactly twice the group velocity (Gizon, 2006).

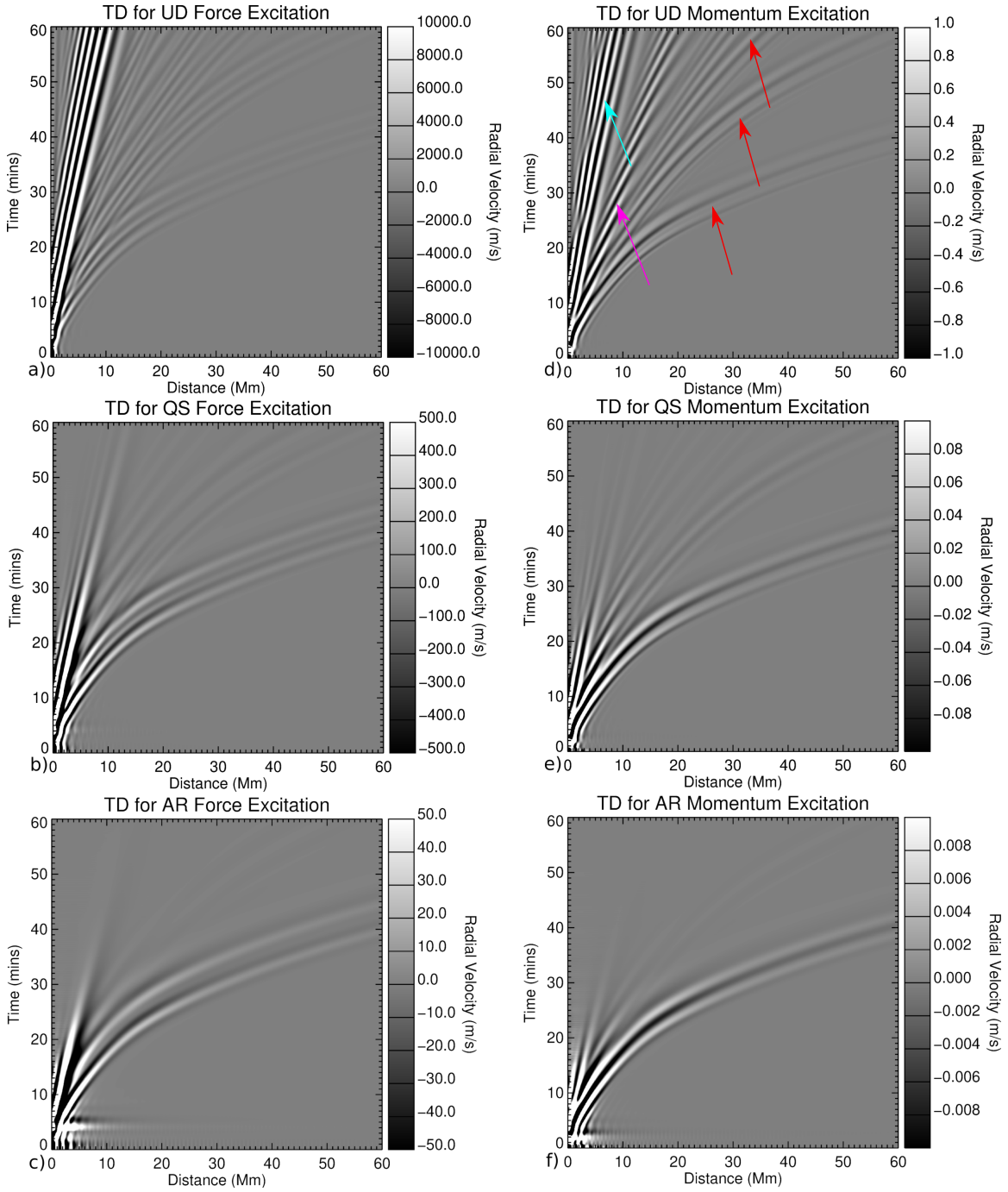

Figure 4.3 Time-distance diagrams of radial velocity on the solar surface (R=696 Mm) for force excitations with no damping (a), quiet Sun damping (b), and active region damping (c). Time-distance diagrams of radial velocity on the solar surface (R=696 Mm) for momentum excitations with no damping (d), quiet Sun damping (e), and active region damping (f). The different wave modes are highlighted in panel d, with p-modes indicated by red arrows, the f-mode indicated by the magenta arrow, and atmospheric acoustic-gravity waves indicated by the cyan arrow.
Source: Stefan & Kosovichev (2020)

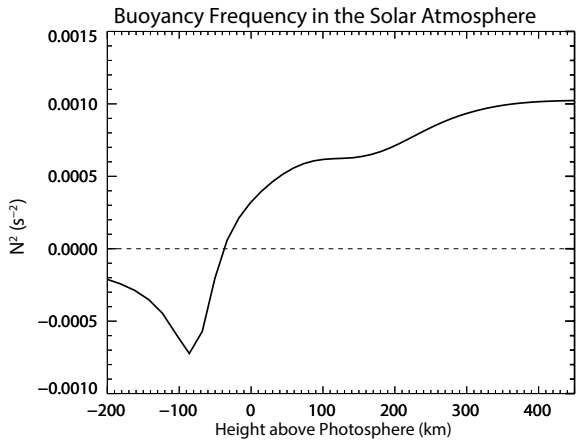

Figure 4.4 Square of the buoyancy frequency in the solar atmosphere, with the base of the photosphere denoted by $z = 0$. Negative values indicate regions of unstable gravity wave propagation and positive values indicate stable propagation.
Source: Stefan & Kosovichev (2020)

We also observe surface-propagating acoustic-gravity waves in the simulation, indicated by the cyan arrow in Figure 4.3d. Both excitation mechanisms produce these waves, which propagate similarly to atmospheric gravity waves on Earth (e.g. Row (1967)), though they are stronger for the force mechanism than the momentum mechanism. The solar atmosphere is technically stable to gravity wave (or g-mode) propagation in linear acoustics, with a real-valued buoyancy frequency (Figure 4.4). Such waves haven't been observed on the Sun however, and it's likely that convective flows, which oscillate with similar frequencies to gravity waves, either mask or break up any generated acoustic-gravity waves.

The acoustic-gravity waves are affected more strongly than the p-mode wave packet as the damping is increased, though the successive bounces of the sunquake and f-mode both show decreased in amplitude. In general, the phase relationship of the momentum-excited sunquakes is preserved and shorter-wavelength features appear to be smoothed. There is similar smoothing apparent in the force-excited sunquakes, though the first-bounce signal appears to have split into two separate wave packets. As the damping increases from quiet Sun to active region, the f-mode and acoustic-gravity waves are almost entirely damped, and successive bounces of the

p-mode wave packet are barely measurable. Additionally, there is some introduction of an artifact near the origin for both excitation mechanisms in the active region damping scenario, caused by the loss of small-scale resolution from the strong damping on high wavenumbers.

4.2.3 Comparison with Observations

We now compare our results with several observed sunquakes, including the events associated with the X1.8 flare in October 2012, the X9.3 flare in September 2017, the X3.3 flare in November 2013, the X1.0 flare in March 2014, and the M1.1 flare in September 2015 (Table 4.1). The initial time and location of these events are derived from the sunquake catalog produced by Sharykin & Kosovichev (2020).

Table 4.1 Sunquake Events and Relevant Times

GOES Flare Class	Date	T_{start} (UT)	Lon.[a] (deg)	Lat.[a] (deg)	T_{G1} (s)	T_{G3} (s)	T_{BP} (s)
X1.8	2012 Oct 23	03:16:30	110.3	-12.7	+85	+141	+45
X9.3	2017 Sep 6	11:57:00	122.6	-9.1	-82	-49	-60
X3.3	2013 Nov 5	22:10:19	175.5	-12.6	+34	+76	+56
X1.0	2014 Mar 29	17:45:00	132.5	+32.0	+17	+48	+135
M1.1	2015 Sep 30	13:15:00	108.0	-21.0	+86	+48	N/A

Source: Stefan & Kosovichev (2020)

[a]Latitude and longitude are given in Carrington heliographic coordinates.

We produce time-distance diagrams for these events using Dopplergrams obtained by HMI, which are filtered with a Gaussian function in frequency. The width of the filter and the central frequency vary between events, and these parameters are chosen to enhance the contrast between the sunquake wave packet and background noise. We produce corresponding time-distance diagrams for our simulation runs, which are treated with the same filter after the resolution and cadence have been

adjusted to match the particular observed event. We generate two sets of simulations, for the momentum and force excitation mechanisms, with each set containing 46 sunquakes of fixed radial width and centered along the grid points of our background mesh in the range of $r = 695.788$ Mm to $r = 696.422$ Mm.

To quantify how closely an observed sunquake event corresponds with a particular simulation, we evaluate the cross-correlation between the two time-distance diagrams as a function of offsets in both time (τ) and distance from the source (ξ). The signal from an observed sunquake, denoted by S, is dependent on time, t, and distance from the source d, and the sets of simulated sunquakes also have these dependences along with the additional dependence on source depth, z. The cross-correlation between the observed and modeled sunquake signals is then computed as

$$\Xi(\tau, \xi, z) = \frac{1}{N_d} \sum_t \sum_d S(t, d) S'(t + \tau, d + \xi, x), \tag{4.45}$$

where N_d is the number of pixels in the horizontal direction. We then identify the distance shift which maximizes the cross-correlations such that function $\Xi^\star(\tau, z)$ is dependent only on the offset in time and excitation depth, expressed as

$$\Xi^\star(\tau, z) = \max_\xi \left(\Xi(\tau, \xi, z)\right) \tag{4.46}$$

The simulation of best fit is found depending on which time offset and excitation depth maximize the cross-correlation $\Xi^\star(\tau, z)$, and the ratio of the maximum velocities of the simulated and observed sunquake wave fronts are used to determine the total kinetic energy necessary to excite the observed sunquake. For the momentum excitation mechanism, the kinetic energy is computed by the volume integral of the

kinetic energy density,

$$\mathrm{KE} = \int_V \rho_0(r) v_r^2(r, \vartheta) dV, \tag{4.47}$$

using the form of v_r described in Subsection 4.2.1. For the force excitation mechanism, we consider the kinetic energy deposited to be equal to the net work done by the force over the duration of excitation. This is given by

$$\mathrm{KE} = \int_V \int_t F_r(r, \vartheta, t) \cdot v_r(r, \vartheta, t) dt dV. \tag{4.48}$$

The time shift indicated by the maximum of the cross-correlation is examined in the context of three important times: 1) when the time derivative of soft X-ray (SXR) emission is maximized; 2) the time when the hard X-ray (XHR) emission is maximized; and 3) the start time of the sunquake as determined from the appearance of so-called HMI bad pixels. Bad pixels occasionally appear in Dopplergram images which have wildly different values from their neighbors and are a result of the failure of algorithms to correctly interpret raw observations in Level 1 processing. These pixels generally indicate extreme values of Doppler velocity, magnetic field, and other observables, which are associated with flare impacts in the low atmosphere (Couvidat et al., 2016). We interpret these pixels as the source location of observed sunquake events, and identify the first appearance of bad pixels (T_{BP}) as the start time of the sunquake.

Based on models of thick-target heating of the chromosphere, for example as described in Fisher et al. (1985), strong HXR emission should be expected from the impact of particles accelerated by the sunquake's originating flare (Brown, 1971).

After the particles have heated the impacted plasma, SXR emission is expected from thermal bremsstrahlung radiation (Veronig et al., 2002). The so-called Neupert effect (Neupert, 1968) posits that the total HXR fluence is related to SXR emission through the previously described mechanism. Equivalently, the time-derivative of the SXR emission should be related to the HXR emission. We therefore examine how the timing of these two quantities relates to the excitation of sunquakes using data obtained from the KONUS instrument aboard the Wind spacecraft (Aptekar et al., 1995; Lysenko et al., 2018). Observations by KONUS are made in three bands: G1 in the 21-82 keV range (the upper range of the X-ray spectrum considered to be soft); G2 in 82-331 keV range; and G3 in the 331-1252 keV range (the upper range of the X-ray spectrum considered to be hard). Here, we use the time derivative of the G1 band as a proxy for the dSXR/dt peak (T_{G1}) and the G3 band's peak as the HXR peak (T_{G3}). These times, and the bad pixel times, are listed in Table 4.1 relative to the start time of Dopplergram observations; for the M1.1 sunquake, bad pixels could not be identified.

The best-fit parameters derived from the cross-correlations using the momentum and force excitation mechanisms are detailed in Tables 4.3 and 4.3, respectively, and a visual comparison between the X1.8 sunquake and best fit simulations as well as a comparison for the X9.3 sunquake are provided in Figure 4.5. The cross-correlation functions $\Xi^{\star}(\tau, z)$ for the quiet Sun damped momentum and force mechanisms are shown in Figures 4.6 and 4.7, respectively. Since the sunquake wave front oscillates with a period of several minutes, more than one band of best fit is often present in the cross-correlations. For the momentum mechanism, Table 4.3, a majority of the simulated undamped sunquakes have energies bounded by 10^{28} ergs and initial velocities on the order of 10 km s^{-1}. While there is not a common height at which the observed sunquakes are excited, the excitation is consistently decreased as the damping is increased.

Table 4.2 Best Fit Parameters for Sunquake Events - Force Mechanism

		Force Case			
Flare	Damping	T_{shift} (s)	Height (km)	Amp. (dyn cm^{-3})	Energy (ergs)
X1.8	Undamped	-146.25	-203	1.38×10^{-2}	1.01×10^{28}
	Quiet Sun	-157.5	-203	1.01×10^{-1}	5.58×10^{28}
	Active Region	-157.5	-203	6.59×10^{-1}	2.58×10^{29}
X9.3	Undamped	+135	+129	2.19×10^{-3}	2.27×10^{27}
	Quiet Sun	-33.75	-203	2.29×10^{-1}	1.27×10^{29}
	Active Region	-45	-203	1.57	6.17×10^{29}
X3.3	Undamped	+135	+181	5.65×10^{-4}	6.44×10^{26}
	Quiet Sun	+157.5	+255	1.30×10^{-2}	1.32×10^{28}
	Active Region	0	-33	4.24×10^{-1}	2.07×10^{29}
X1.0	Undamped	-157.5	+327	3.59×10^{-3}	4.56×10^{27}
	Quiet Sun	-157.5	+155	5.34×10^{-2}	4.73×10^{28}
	Active Region	-11.25	+432	6.52×10^{-1}	3.73×10^{29}
M1.1	Undamped	+146.25	-203	4.04×10^{-2}	2.93×10^{28}
	Quiet Sun	-78.5	-203	2.59×10^{-1}	1.44×10^{29}
	Active Region	-90	-203	1.45	5.68×10^{29}

Source: Stefan & Kosovichev (2020)

When comparing the observed sunquake events with the set of simulations using the force mechanism, the same relationship between excitation height and damping strength is preserved. The amount of kinetic energy necessary to reproduce observations is similar in the undamped case to the momentum mechanism, with energies also on the order of 10^{28} ergs (Table 4.2). As the damping is increased in the active region damping scenario, the energy estimates vary much less widely than for the momentum mechanism with similar damping, with energies for all observed events on the order of 10^{29} ergs.

Table 4.3 Best Fit Parameters for Sunquake Events - Momentum Mechanism

		Momentum Case				
Flare	Damping	T_{shift} (s)	Height (km)	Amp. (g cm s^{-1})	Max. V (km s^{-1})	Energy (ergs)
X1.8	Undamped	-45	-17	1.95×10^{22}	11.1	6.39×10^{27}
	Quiet Sun	-45	-104	3.31×10^{23}	141.8	1.39×10^{30}
	Active Region	-56.25	-142	1.76×10^{24}	675.6	3.53×10^{31}
X9.3	Undamped	+112.5	+432	5.40×10^{21}	32.5	3.05×10^{27}
	Quiet Sun	+112.5	-33	1.54×10^{23}	82.3	3.74×10^{29}
	Active Region	+112.5	-68	1.54×10^{24}	785.8	3.82×10^{31}
X3.3	Undamped	+135	+386	2.68×10^{21}	11.5	5.88×10^{26}
	Quiet Sun	+67.5	+386	2.83×10^{22}	121.2	6.57×10^{28}
	Active Region	-123.75	-162	1.65×10^{24}	599.8	2.94×10^{31}
X1.0	Undamped	+67.5	+87	2.87×10^{22}	24.0	1.94×10^{28}
	Quiet Sun	+78.75	-86	9.48×10^{23}	430.2	1.21×10^{31}
	Active Region	+78.75	-123	6.96×10^{24}	2825.6	5.85×10^{32}
M1.1	Undamped	+101.25	-182	4.60×10^{22}	15.8	2.15×10^{28}
	Quiet Sun	+135	-203	7.34×10^{23}	238.8	5.19×10^{30}
	Active Region	+123.75	-203	5.47×10^{24}	1780.1	2.88×10^{32}

Source: Stefan & Kosovichev (2020)

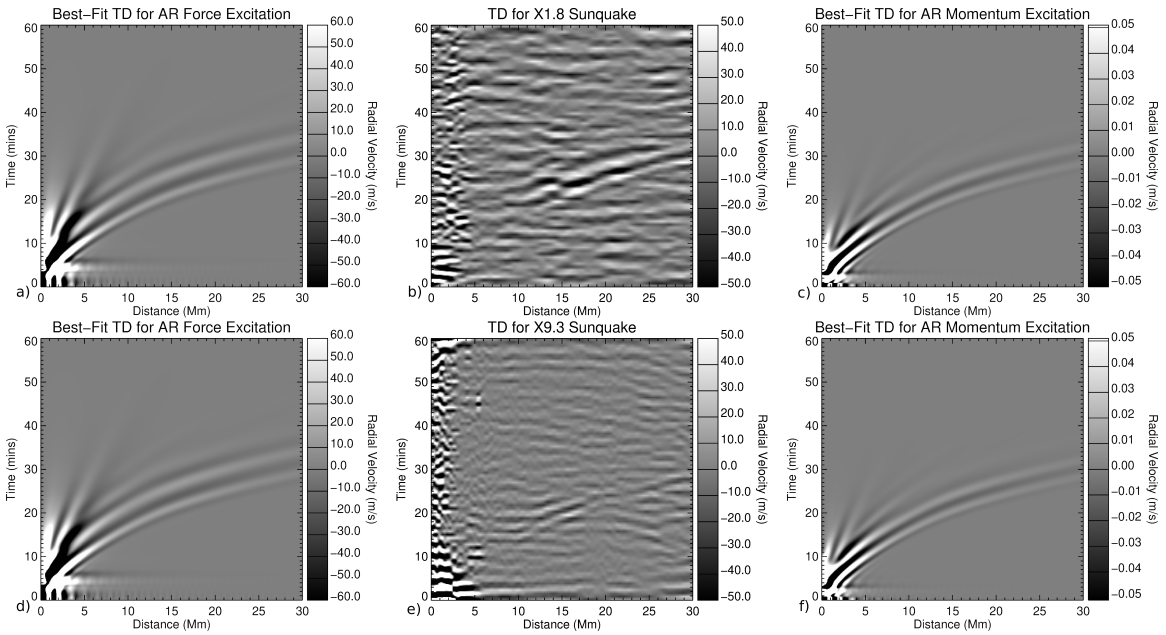

Figure 4.5 Time-distance diagrams of: a) the best fit force case for the sunquake of the X1.8 flare; b) the sunquake produced by the X1.8 flare; c) the best fit momentum case for the sunquake of the X1.8 flare; d) the best fit force case for the sunquake of the X9.3 flare; e) the sunquake produced by the X9.3 flare; f) the best fit momentum case of the X9.3 flare. Darker pixels correspond to more negative velocities, lighter pixels correspond to more positive velocities.
Source: Stefan & Kosovichev (2020)

For some of the observations, the maxima of the cross-correlations does appear close to previously described flare-relevant times. For example, in two of the five sunquake events evaluated with the undamped momentum mechanism, the M1.1 and X1.0 events, the timing of the best-fit case immediately follows the HXR peak. As the damping is increased, this count increases to three for quiet Sun damping—the previous two events and the X3.3 event—but reduces back to two in the active region damping scenario. For the force mechanism, only two best-fit cases are identified close to the HXR peak, which reduces to one in both the quiet Sun and active region scenarios.

In general, it should be expected that the best-fit excitation depth moves downwards as the damping strength is increased, since excitation in the denser layers leads to larger amplitude waves higher in the atmosphere from a conservation of

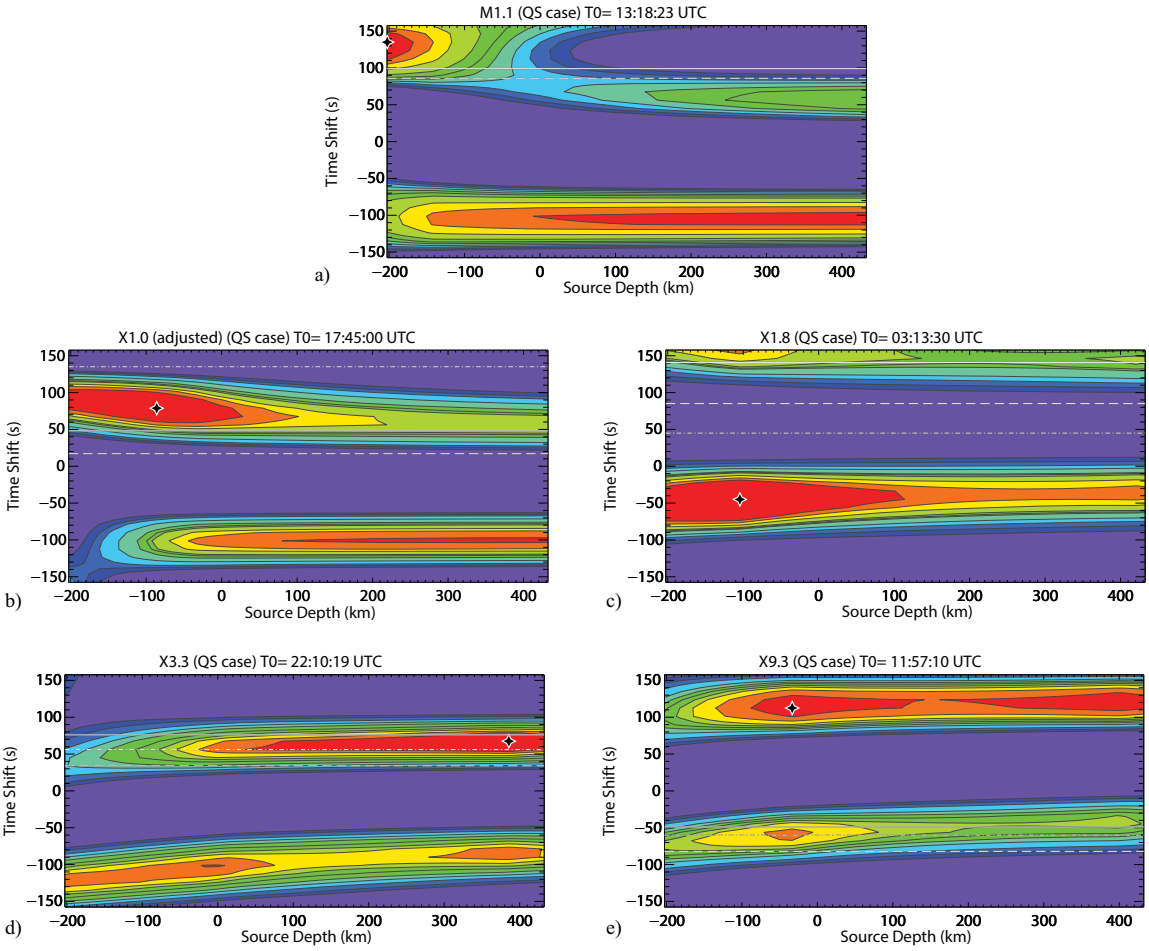

Figure 4.6 Cross-correlation functions with the quiet sun damped momentum mechanism set for the sunquake associated with the M1.1 flare (a), with the X1.0 flare (b), with the X1.8 flare (c), with the X3.3 flare (d), and with the X9.3 flare. The contours begin at the median value, and each successive contour represents an increase in 5 percentile points. The solid horizontal line shows the HXR peak time, the dashed horizontal line shows the dSXR/dt peak time, and the dot-dashed horizontal line shows the suspected sunquake start time based on bad pixel count. The white and black diamond indicates where the parameters produce the greatest cross-correlation. Redder colors indicate greater correlation, green representing intermediate correlation, and purple representing low correlation.
Source: Stefan & Kosovichev (2020)

momentum perspective. Consequently, the estimated energy required to excite the observed sunquakes increases with depth, as more energy is required to move the denser material. However, the active region damping scenario is not necessarily representative of *in situ* conditions of sunquake propagation, which assumes that the sunquake wavefront is traveling through a strongly magnetized region. In fact, the sunquakes observed here are excited at the edge of the corresponding active regions and propagate mostly in regions of moderate magnetic field.

Furthermore, the estimates of excitation energy can only be relied upon when the identified best-fit time shift, τ, follows or coincides with the HXR peak or bad pixel times which are both clear indications of energy deposition. The M1.1, X1.0, and X3.3 events satisfy this criteria for the momentum mechanism, while only the M1.1 and X9.3 events satisfy this criteria for the force mechanism. The X1.8 event has strong correlations near the HXR, dSXR/dt, and bad pixel times for both mechanisms (Figures 4.6c and 4.7c), but these time shifts do not maximize the cross-correlations. For the events which correspond well with a momentum mechanism, the undamped excitation energy is on the order of 10^{28} ergs, consistent with energy estimates made by Chen (2019) using acoustic holography. And though the X1.8 event does not produce strong correlations in the undamped momentum mechanism, the quiet Sun and active region damping scenarios return a time shift very close to the peak HXR time and excitation energies on the order of 10^{28} ergs and 10^{29} ergs, respectively. Similarly for the X9.3 event with a force mechanism, the undamped case is not temporally coincident with flare-relevant times but the quiet Sun damping scenario indicates an excitation time just after the HXR peak time. The energy estimate for this excitation is around 10^{29} ergs which is not unreasonable for strong X-class flare that may release up to 10^{32} ergs (Hudson, 2011).

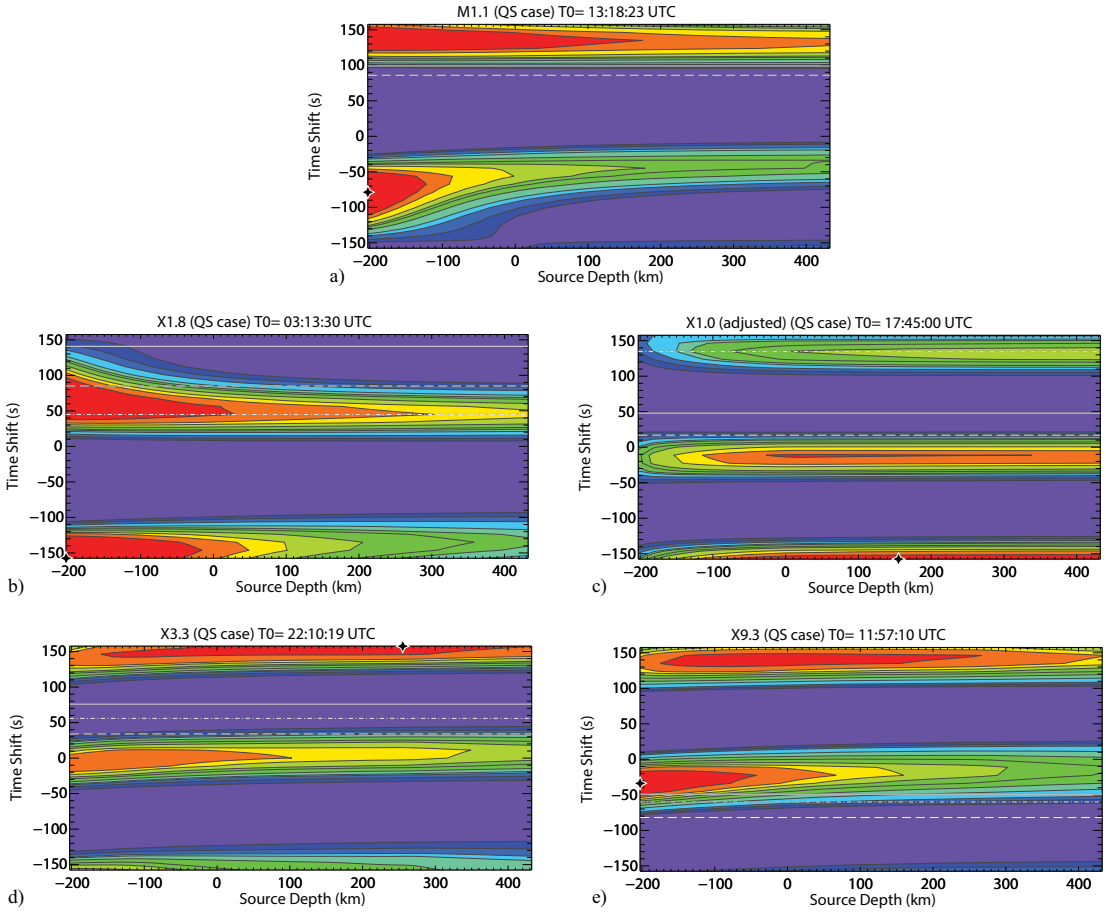

Figure 4.7 The same as in Figure 4.6 for the force mechanism.
Source: Stefan & Kosovichev (2020)

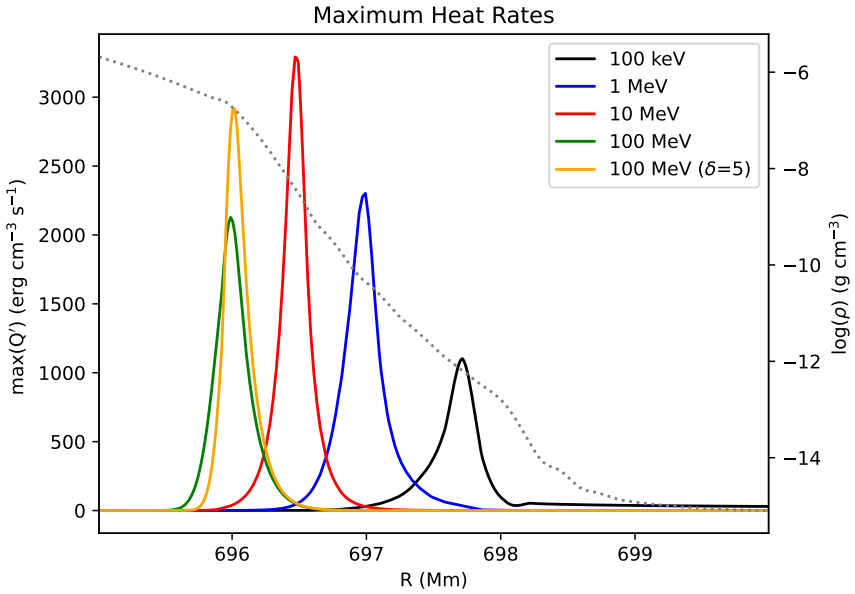

Figure 4.8 Maximum heating rates derived from the proton beam simulations, used to excite sunquakes in the hydrodynamic model. For all beams but the 100 MeV (δ=5), the spectral index is 3. The gray dotted line represents the background density.

4.3 Atmospheric Heating Derived from FP Simulations

4.3.1 Description of Simulations

In this section, we use radially-dependent heating rates derived from FP proton beam simulations (Allred et al., 2020) to excite acoustic waves. The Fokker-Planck proton beams all have identical energy flux, 10^{11} erg cm^{-2}, with increasing low energy cut-off varying from 100 keV to 100 MeV. Except where explicitly stated, the proton beams have spectral index $\delta = 3$. The volumetric heating rates are shown in Figure 4.8, along with the acoustic model's background density profile in gray. The subsurface background profile is still the Standard Solar Model (Christensen-Dalsgaard et al., 1996), though the VAL-C atmosphere (Vernazza et al., 1981) has been carefully appended where the original background profile ends. This extends the total height of the background profile to $r = 711$ Mm, which accommodates the strong heating of the upper chromosphere from the 100 keV beam as well as the corresponding weak heating in the low corona.

4.3.2 Deriving the Modeled Perturbations

Since our model does not have an explicit term for heating, we treat the energy deposition of the proton beams as a pressure perturbation. This pressure perturbation is directly derived from the FP-provided volumetric heating rates Q'_{vol} in the following manner. For a fixed amount of heat transferred in a fixed volume, we have

$$dQ = C_V dT \tag{4.49}$$

with the corresponding time dependence

$$\frac{dQ}{dt} = C_V \frac{dT}{dt}, \tag{4.50}$$

where C_V is the heat capacity of the plasma at constant volume. Assuming the plasma behaves as an ideal gas, such that $C_P - C_V = NK$ and $PV = NKT = (C_P - C_V)T$, the change in temperature can be expressed in terms of a pressure perturbation P' as

$$\frac{Q'}{C_V} - \frac{d}{dt}T = \frac{d}{dt}\left(\frac{P'V}{(C_P - C_V)}\right), \tag{4.51}$$

where Q' is the heating rate in erg s^{-1} and C_P is the heat capacity of the plasma at constant pressure. Since the volume element under consideration is constant, the

above can be simplified by

$$\frac{Q'}{C_V} = \frac{V}{(C_P - C_V)} \frac{dP'}{dt}, \tag{4.52}$$

which reduces to

$$\frac{dP'}{dt} = \frac{Q'}{V} \frac{(C_P - C_V)}{C_V} = Q'_{\text{vol}}(\gamma - 1) \tag{4.53}$$

with γ being the adiabatic index and Q'_{vol} in erg cm^{-3} s^{-1}. Since we consider the normalized pressure perturbations $\overline{P} = P'/P_0$, the source term used in Equation (4.14) is

$$\frac{d\overline{P}}{t} = \frac{Q'_{\text{vol}}}{P_0}(\gamma - 1). \tag{4.54}$$

We assume that the area heated by the proton beams is constant over height, and the horizontal profile of the volumetric heating rate is considered to be Gaussian with a FWHM of 1.5 Mm. Where the lower end of the supplied heating functions end, slightly below $R = 696$ Mm, the volumetric heating rates are appended by a Gaussian with drop-off closely matching existing data. This is only strictly necessary for the 100 MeV $\delta = 3$ and $\delta = 5$ beams which penetrate deeply into the solar atmosphere, but is also applied to the other beams to ensure a smooth transition to zero heating in the acoustic model.

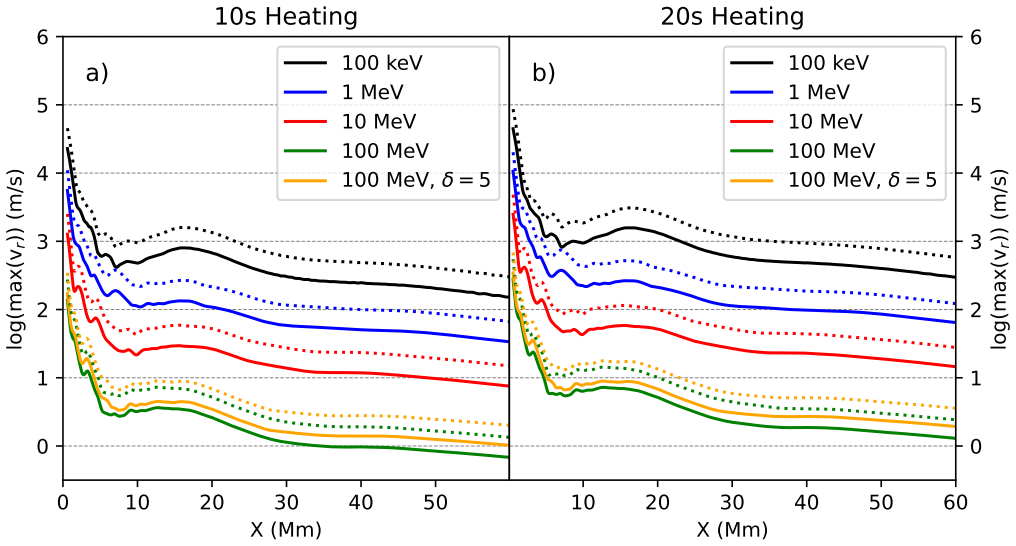

Figure 4.9 Log of the sunquake wavefront maximum vertical velocity amplitude over horizontal distance, for a 10 second beam duration (a) and 20 second beam duration (b). The dotted curves represent amplitudes for the square heating rate case, and the solid lines represent the triangular heating rate case.

4.3.3 Sunquake Amplitudes

Using the volumetric heating rates as a maximum, we consider heating durations of 10 and 20 seconds with square and triangular temporal profiles. We then examine the resulting photospheric wavefront, with maximum radial velocity for each case shown as a function of horizontal distance from the beam target in Figure 4.9. Surprisingly, the lowest cut-off energy beam, 100 keV, produced the highest amplitude wavefront. This wavefront has minimum amplitude of nearly 1 km s^{-1} at a horizontal distance of 17 Mm for the 10 s triangular profile, and 3 km s^{-1} at the same distance in the case of a 20 s square profile.

As the low energy cut-off increases, the amplitude of the photospheric wavefront decreases; taking the 10 s triangular profile as an example, from 800 m s^{-1} for the 100 keV low energy cut-off to 3 m s^{-1} for the 100 MeV cut-off. This decrease in wavefront amplitude is exponential with low energy cut-off, with log-10 spectral index $\epsilon = -0.779 \pm 0.001$ for all temporal profiles.

The somewhat paradoxical relationship between the low energy cut-off and maximum photospheric wavefront amplitude—that the 100 keV beam deposits the least energy yet produces the highest amplitude wavefront—can be explained by examining the expected acceleration rates produced from each beam. The acceleration rates shown in Figure 4.10 are derived from the gradient in the pressure perturbations which the model is supplied and the local background density. While the pressure gradient in the 100 keV beam is moderately smaller than the other beams, this gradient acts in a region of relatively low density which leads to the high acceleration of the local plasma. As the beam cut-off energy increases, the corresponding acceleration rate decreases as the beams deposit energy in gradually deeper layers of the solar atmosphere.

We, therefore, expect that the exponential decrease in wavefront amplitude is caused not by the amount of energy deposited, but by where that energy is deposited. That is, the local density of the beam target is significantly more important than the amount of energy deposited; however, the height of maximum energy deposition is of course strongly constrained by the energy content of the proton beam. This height dependence is further supported by the comparison between the $\delta = 3$ and $\delta = 5$ 100 MeV beams. Both beams deposit energy at nearly the same depth, and despite the $\delta = 5$ beam depositing almost 50% more energy than the $\delta = 3$ beam, both produce wavefronts of similar magnitude, separated by about 4 m s^{-1} at the X=17 Mm peak.

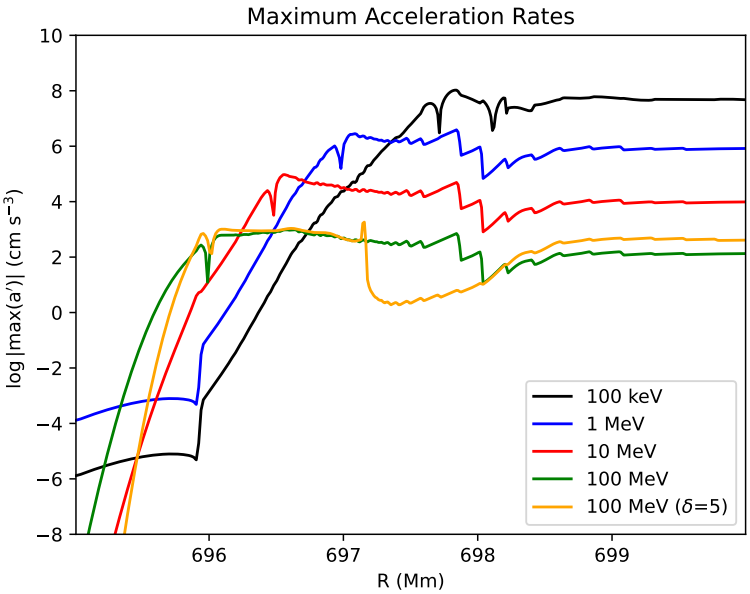

Figure 4.10 Log of the expected acceleration rates derived from the heating rates.

CHAPTER 5

DISCUSSION

5.1 The Detectability of Emerging Flux

In Chapter 2, we presented a method for detecting emerging magnetic flux from mean phase travel time deviations 40 to 70 Mm beneath the photosphere. In particular, Section 2.4 presents the perturbation index for several active regions and how this compares to the perturbation index of quiet Sun regions. It is found that in the quiet Sun, the perturbation index can occasionally reach values as large as 13000 s Mm^2, though it mostly fluctuates between 4000 and 6000 s Mm^2. Choosing this maximum as the criteria for positive emerging flux detection, three of the four active regions presented in Section 2.4 are able to be identified 24-36 hours before emergence.

Detailed spatial features, however, cannot be observed using our time-distance method, and likely not through any other helioseismic method. The average wavelength of oscillations penetrating 40 to 70 Mm beneath the photosphere is 3 Mm, which significantly reduces the resolution of any detected features. While we are limited in the resolution of phase travel time maps, the location of the positive and negative travel time shifts relative to the eventual location of the magnetic flux concentration is interesting. At the time of peak emergence, we find areas of strong positive mean travel time shifts—which may be caused by diverging flows that reduce the local wave speed—spatially coincident with the later development of active regions. The strong negative travel time shifts used to compute the perturbation index are generally adjacent to these positive travel time shifts.

Prior studies have found that travel time perturbations due to flows induced by the magnetic field should be stronger than the field's direct perturbation to the wave speed (Braun, 2012); specifically, that radial flows are strongest above the rising

magnetic flux and that stronger horizontal flows dominate the regions adjacent to the rising magnetic flux (Birch et al., 2010). This may explain our observations of strong negative travel time shifts adjacent to the eventual location of active regions, as the convergence and divergence of these flows relative to the background plasma may also induce shifts in the wave travel time.

In our larger-scale analysis of active region emergence in Section 2.5, we found that the peak correlation time between the mean phase travel times and the surface magnetic flux for most active regions occurs prior to the flux emergence is not particularly strong. Some pixels may have a cross-correlation amplitude as strong as 0.35—close to the theoretical value from the simplified model presented in Section 2.5.1—though the spatial average is generally much lower, on the order of 0.02. Considering only pixels where the corresponding magnetic field is greater than 100 G increases the spatial average by slightly more than a factor of two, to on the order of 0.05. However, the non-uniformity of the correlation lag times about $T = 0$ does indicate that there is some degree of connection between the mean phase travel times and the emergence of active regions.

Examining the relationship between the correlation lag times and peak perturbation index times shows that, at least for the thresholds used in this work, the perturbation index itself is not a strong indicator of emerging magnetic flux. Of the 46 active regions studied, only 28 of these regions, on average, have the maximum perturbation index prior to the emergence of the magnetic flux. Additionally, only 30 of the active regions, on average, have the time of peak perturbation index preceding the correlation lag time. There is also no significant relationship between the time of peak perturbation index and maximum magnetic flux, maximum flux rate, or sunspot size, with the Spearman correlation coefficient ρ on the order of 10^{-2}.

We find that for a majority of active regions, the peak correlation between the surface magnetic field and the mean phase travel time deviations occurs before the

active region emerges, with a median time lag in the best case of −16 hours prior to emergence. Separating the measurement annuli into additional arc segments does not necessarily increase the sensitivity of the measurements, and our results suggest that eight arc segments is optimal. While the median correlation lag time for the Gabor wavelet procedure is slightly greater than that of the GB02 procedure, the GB02 procedure has a greater number of active regions with a correlation lag time preceding the emergence of the active regions in every arc segment case. Additionally, we find no strong correlation between the lag times and sunspot size or maximum flux, though there is a noticeable correlation between the lag times and the maximum flux rate.

5.2 Properties of Sunspot Subsurface Magnetic Fields

One of the more surprising features in the measurements made in the sunspot simulation developed by Rempel (2012) is the apparent 90° counter-clockwise rotation of the magnetic field's azimuth in Figure 3.3c, relative to the true azimuth. While the outer 10 Mm of the subsurface azimuth aligns very well with the true subsurface state, the inner feature likely develops as a failure of our assumption of a uniform magnetic field since the magnetic field quickly changes direction in the center of the sunspot. The spatial coincidence of suppressed travel time anisotropy (Figure 3.3d) seems to support this, where the size of the suppression is larger than the corresponding region of low horizontal field magnitude. In both the azimuth and travel time anisotropy, the anti-symmetric term in Equation (3.24) may provide an opposing contribution to the travel time perturbation where the magnetic field is non-uniform.

However, such a rotation of the azimuth is not observed in any of the studied active regions. This may be due to the significantly coarser resolution and the greater noise level which might mask this feature, especially as the azimuth inversion lines—where the azimuth changes from 180° to 0°—do not extend to the center of the

sunspot in the active region measurements. Based on the results from the sunspot simulation though, we should expect the region avoided by the azimuth inversion lines to be of similar size to the area of anisotropy suppression, which is only true for ARs 12786 and 12794 at depths of $z = -10$ to -13 Mm (Figures 3.5p,q,s,t and 3.6p,q,s,t respectively).

Another interesting aspect of our active region measurements is the significantly reduced anisotropy for AR 12786, as compared to ARs 12218 and 12794. While the actual magnitude of the subsurface horizontal magnetic field is, of course, unknown, the surface horizontal field magnitude is similar between each active region. Assuming the field remains constant with depth, it should be expected that the active regions' travel time anisotropies will have correspondingly similar magnitudes. One possibly contribution to the relatively small anisotropy may be AR 12786's slightly smaller area compared to the other two active regions. This would also explain the greater maximum anisotropy in AR 12794 compared to AR 12218, which is moderately smaller, as an acoustic wave traveling through AR 12794 would encounter greater magnetic flux and therefore have a stronger travel time perturbation.

Comparing the azimuth and anisotropy measurements derived from the GB02 procedure with those derived from the Gabor wavelet fitting, it is clear that the GB02-derived measurements outperform in nearly every case. This is somewhat expected as the GB02 procedure is much less sensitive to noise in the cross-correlations; the GB02 procedure has only one dependent parameter for error minimization—the time lag—whereas the Gabor wavelet fitting method has five—the group and phase time lags, cross-correlation amplitude, frequency of oscillation, and width of the Gaussian envelope. While these additional parameters in the Gabor wavelet procedure may be useful for other studies, there is reduced accuracy in the travel time measurement as the combined error of all parameters is minimized, as opposed to only the phase travel time lag in the GB02 procedure.

The measurements made from the acoustic simulation with uniform background magnetic field confirm that the combination of travel times in Equation (3.31) accurately reproduces the magnetic field's azimuth. Other measurements made in this simulation, in conjunction with the simulation of a realistic sunspot, also confirm that the anisotropy parameter defined in Equation (3.32) is a reasonable proxy for the magnitude of the subsurface magnetic field where the approximation of a uniform magnetic field is at least somewhat valid. Despite the increased noise level, we further show that the detection of travel time anisotropy in active regions is feasible and can be used to recover some aspects of the subsurface magnetic field's structure.

5.3 Excitation Mechanisms for Sunquakes

From the correlation analysis made in Section 4.2 with several observed sunquake events, the signal in time-distance diagrams is clearly degenerate in parameter space with respect to source depth and time shift. Recalling that the time shift is between the start time of simulations and the suspected start time of the sunquake event, it should be relatively easy to account for in further analysis. We expect the start time of sunquake events to be close to the HXR peak time and bad pixel times, and any correlation-indicated time shifts which do not align with these times can be disregarded. Accounting for the degeneracy in excitation depth, however, is somewhat more difficult to account for. We find that the lower wave front amplitudes characteristic of deep excitation can be compensated for by greater energy deposition, though bounding the amount of deposited energy by the flare energy budget for a given event's flare-class can reduce this depth uncertainty.

Additionally, there are several events—most notably the X1.0 event—which seem to suggest the presence of a high excitation source in some damping scenarios, though these sources tend to produce weaker p-mode wave fronts and stronger acoustic-gravity waves with increasing height in our simulations. Similar corre-

spondence between excitation height and the strength of acoustic-gravity waves is observed in the simulated events of Section 4.3 with the proton beam heating rates. The 100 keV beam, with the highest location of peak heating around $r = 697.8$ Mm, produced the strongest acoustic-gravity waves of the proton beams considered in this work, for all temporal profiles. The 100 MeV beam which penetrated furthest into the atmosphere correspondingly produced the weakest acoustic-gravity waves.

While the low-energy cutoff of 100 MeV is quite extreme, the initial expectation was that such a deeply penetrating beam would serve as an upper bound of the wavefront amplitude for the collection of simulations, especially the $\delta = 5$ 100 MeV beam which deposits the second greatest amount of heat. As discussed previously in Section 4.3.3 however, the opposite relationship was instead observed, with the weaker and less-deeply penetrating beams producing the stronger wave front amplitudes. While we believe that this relationship is adequately explained by the expected acceleration rates shown in Figure 4.10, it should be noted that the 100 keV beam produced supersonic downflows near the excitation source. For the 20s square heating rate, these downflows approach $M = 4$ at the center of the source. Considering that our model is linear, we do not adequately capture the shock dynamics expected of these downflows, and it may be possible that non-linear effects reduce the resulting wave front's unrealistically large amplitude of ≈ 1 km s^{-1}.

5.4 Directions for Future Work

The results of this dissertation highlight several avenues for future work in the helioseismic study of active regions. Regarding the early detection of emerging active regions, the use of mean phase travel time deviations as indicators of emerging flux appears to be successful. While there is inherent noise in helioseismic measurements made at significant depths ($z = -40$ to -70 Mm), there is significant potential benefit to the corresponding early detection (24-36 hours) compared to only several hours for

more shallow measurements. The phase travel time maps in Section 2.4 also suggest that measurements of flows at similar depths may also yield additional insights, and this is further motivated by the work of Birch et al. (2010).

The direct interpretation of our phase travel time maps, however, remains difficult as the composite measurements are averaged over $\approx$ 30 Mm. A depth-dependent analysis can be made, though at the cost of a decrease in the signal-to-noise ratio. The use of machine learning techniques to interpret the phase travel time maps serve as one potential approach for identifying emerging magnetic flux directly from these maps. Such techniques have already had success, for example in the use of convolutional neural networks (CNNs) to convert far-side travel time measurements into magnetic flux maps (Hess Webber et al., 2020), in up-scaling MDI and GONG Magnetograms to HMI resoltution (Munoz-Jaramillo et al., 2021) and in predicting solar flares from HMI Magnetograms using a support vector machine (SVM) (Bobra & Couvidat, 2015). While in our case there are far fewer positive samples—cases where an active region emerges—compared to negative samples, there exist so-called few sample learning (FSL) techniques which may overcome this bias (Lu et al., 2020).

The clear next step in examining the structure of subsurface magnetic fields in active regions is to develop inversions for the actual magnitude of the horizontal field from the measured travel time anisotropies. Sensitivity kernels derived from the ray-approximation appear to be the most straightforward approach to such inversions, as these can be directly derived from Equations (3.31) and (3.32) similar to the procedure outlined in Kosovichev & Duvall (1997). While the ray approximation is sometimes criticized as being too simplistic, the large scale features recovered by these kernels are not significantly different from those recovered by Fresnel-zone kernels which take into account finite-wavelength effects (Gizon & Birch, 2005; Couvidat et al., 2004).

Recovery of the radial field, however, remains a difficult pursuit, especially in the formulation of Section 3.2. The radial field appears here in two terms, in the interaction with an oscillation's horizontal wavenumber and in the mixed term containing all wavenumbers and Alfvèn speeds. The first term produces travel time deviations which are indistinguishable from sound speed perturbations and are lost in the computation of the travel time anisotropy (Equation (3.32)). There is a possibility of recovering the radial field from the mixed term, as its contribution to the travel time deviation is dependent on the orientation of an incident oscillation relative to the horizontal field component and so does not behave like a sound speed perturbation. This term was estimated to be negligible under the assumption of a uniform radial field, though it may produce a measurable shift in the travel time for a moderately inclined magnetic field.

Moving to the surface processes of active regions, there is still much work to be done in determining the mechanism which excites sunquakes. Recently published work has suggested the possibility of a deep source—up to 1 Mm beneath the quiet Sun photosphere—for some sunquake events (Lindsey et al., 2020), though the results from Section 4.3 highlight the difficulty in exciting a sunquake of moderate amplitude at even relatively shallow depths. Additionally, the results from Section 4.2 indicate that the energy required for such deep excitation increases significantly with depth.

There appears to be much promise in the possibility of comparatively high source heights for sunquakes for particle beams of moderate low-energy cut-off. Admittedly, our model does not treat such sources with sufficient accuracy in terms of any possible non-linear effects. Future works focused on simulating sunquake excitation should include non-linear terms in models, a feat much easier said than done. A comprehensive simulation which includes both the solar atmosphere and interior covers characteristic length scales which vary over many orders of magnitude. For simulations relying on explicit finite differences, the solar atmosphere in particular

requires the use of very short numerical time steps which make long duration simulations infeasible. This problem of long computation time is exacerbated by the inclusion of non-linear terms, as the governing equations will be coupled in angular degree and, therefore, unable to be decomposed into an independently-solvable system.

APPENDIX A

COMPUTING TRAVEL TIME PERTURBATIONS

The method outlined here is derived for sound speed perturbations c but is applicable to any perturbation along the acoustic ray path which produces a mean travel time perturbation. The expected perturbation to the mean travel time is given by

$$\delta\tau_{mean} = -\int_{\Gamma} \frac{\delta c}{c} S ds, \tag{A.1}$$

where Γ is the unperturbed ray path, $S = k/\omega$ is the phase slowness, and ds is the differential of the ray path. We first need to determine the coordinate s, the path length, which depends on radius r and horizontal position θ. For a coordinate system depending on some parameter a, we have

$$ds(a) = \sqrt{dr^2(a) + r^2(a)d\theta^2(a)} = \sqrt{\left(\frac{dr}{d\theta}(a)\right)^2 + r(a)^2}d\theta^2(a). \tag{A.2}$$

Given the dispersion relation for acoustic waves without the acoustic cut-off frequency, which is negligible everywhere but the surface,

$$\omega^2 = c^2(k_h^2 + k_r^2), \tag{A.3}$$

the derivative $dr/d\theta$ can be determined using the ray approximation,

$$\frac{d\mathbf{r}}{dt} = \frac{d\omega}{d\mathbf{k}}. \tag{A.4}$$

We then have

$$\frac{dr}{dt} = \frac{d\omega}{dk_r} = \frac{ck_r}{\sqrt{k_r^2 + k_h^2}} \tag{A.5}$$

and

$$r\frac{d\theta}{dt} = \frac{d\omega}{dk_h} = \frac{rck_h}{\sqrt{k_r^2 + k_h^2}}, \tag{A.6}$$

where $k_r = \sqrt{(\omega/c)^2 - k_h^2}$ is the radial wavenumber and $k_h = \sqrt{l(l+1)}/r = L/r$ is the horizontal wavenumber. The derivative in Equation A.2 is then

$$\frac{dr}{d\theta} = r\frac{dr/dt}{rd\theta/dt} = \frac{k_r}{k_h} = \frac{r^2\sqrt{\left(\frac{\omega}{c}\right)^2 - \left(\frac{L}{r}\right)^2}}{L}. \tag{A.7}$$

We now need to identify the pair of angular degree l and frequency ω which correspond to oscillations reaching our desired observation depth, r_0. This is found by noting that at a given oscillation's turning point, the radial wavenumber goes to

zero. Making this substitution in Equation A.3 yields

$$r_0 = \frac{\sqrt{(l)(l+1)}c(r_0)}{\omega}, \tag{A.8}$$

which can be solved easily through interpolation. The next step is to evaluate the sound speed perturbation δc along the ray path, which requires us to determine the coordinates (r, θ) along the ray path. We find this by solving Equation A.7 to determine the horizontal distance $\theta_{\text{ray}}(r')$ traveled by the ray to reach radius r',

$$\theta_{\text{ray}}(r') = -2 \int_{R_\odot}^{r'} \frac{c}{r\sqrt{\frac{\omega^2}{L^2} - \frac{c^2}{r^2}}} dr. \tag{A.9}$$

Here, r' is varied from the surface $R_\odot$ to the turning point r', where θ_{ray} correspondingly varies from 0 to $\Delta/2$. We have essentially parameterized the ray path along the computation radial mesh such that there is a unique horizontal distance $\theta_{textray}$ for each point in the mesh $r(a)$.

We can now evaluate the sound speed perturbation δc using these parameterized coordinates. However, the sound speed perturbation in Section 2.3 is defined in latitude λ and longitude ϕ, so we also need to determine the global location of a given ray in our computations. To reproduce the appropriate measurement scheme, for example as in Figure 2.2, we need to find opposing points on an annulus centered on a particular point $(\lambda^{star}, \phi^\star$ with radius Δ. Here, we will consider the case of four opposing pairs of points, which correspond to initial bearings $B = \pm m \times 45^\circ$ for

$m = 0, 3$. The coordinates for the starting point are

$$\begin{aligned} \lambda_1 &= \arcsin\left(\sin(\lambda^*)\cos(\Delta) + \cos(\lambda^*)\sin(\Delta)\cos(B)\right) \\ \phi_1 &= \phi^* + \arctan\left(\frac{\sin(B)\sin(\Delta)\cos(\lambda^*)}{\cos(\Delta) - \sin(\lambda^*)\sin(\lambda_1)}\right) \end{aligned} , \tag{A.10}$$

and the remaining coordinates of the ray are found by reversing the initial bearing and substituting the parameterized horizontal distance $\theta_{\text{ray}}(a)$ for Δ. We find the parameterized global coordinates are

$$\begin{aligned} \lambda(a) &= \arcsin\left(\sin(\lambda_1)\cos(\theta_{\text{ray}}(a)) + \cos(\lambda_1)\sin(\theta_{\text{ray}}(a))\cos(B - 180)\right) \\ \phi(a) &= \phi_1 + \arctan\left(\frac{\sin(B - 180)\sin(\theta_{ray}(a))\cos(\lambda_1)}{\cos(\theta_{ray}(a)) - \sin(\lambda_1)\sin(\lambda(a))}\right) \end{aligned} . \tag{A.11}$$

To summarize, we perform the following steps to compute the theoretical mean travel time deviations:

1. Find the pair of ω and l which correspond to oscillations reaching our desired depth with Equation A.8.
2. Parameterize the ray path using Equation A.9.
3. For each point in the resulting map, replicate the appropriate measurement scheme using global coordinates derived from Equations A.10 and A.11.
4. Evaluate the perturbed sound speed, or other perturbed quantity, using the previously obtained global coordinates.
5. Use the evaluated perturbed sound speed, or other perturbed quantity, to compute the corresponding mean travel time deviation from Equation A.1.

APPENDIX B

DERIVING THE CENTRAL DIFFERENCE FORMULA ON A NON-UNIFORM MESH

The central difference formula on a non-uniform grid can be derived from the matrix equation $BA^{-1}\mathbf{x_0} = \mathbf{x}^\star = B\mathbf{x}'$. Here, $\mathbf{x}'$ is the vector whose elements are the k^{th} analytical derivative of the function y at the i^{th} grid point, $\mathbf{x}^\star$ is the vector containing only the first analytical derivative of y at the i^{th} grid point, and B is the matrix which isolates the first analytical derivative which is zero everywhere except the element $B_{1,1} = 1$. The matrix A has columns containing the Taylor expansion coefficients, $(r_i - r_j)^k/k!$, where $k = 0, 3$ for columns 1 to 4 and $j = i-2, i+2$ for rows 1 to 4 with $j = i$ excluded. Explicitly, the matrices are

$$A = \begin{bmatrix} 1 & -(\Delta r_{i-2} + \Delta r_{i-1}) & \frac{1}{2}(\Delta r_{i-2} + \Delta r_{i-1})^2 & -\frac{1}{6}(\Delta r_{i-2} + \Delta r_{i-1})^3 \\ 1 & -\Delta r_{i-1} & \frac{1}{2}\Delta r_{i-1}^2 & -\frac{1}{6}\Delta r_{i-1}^3 \\ 1 & \Delta r_{i+1} & \frac{1}{2}\Delta r_{i+1}^2 & \frac{1}{6}\Delta r_{i+1}^3 \\ 1 & (\Delta r_{i+1} + \Delta r_{i+2}) & \frac{1}{2}(\Delta r_{i+1} + \Delta r_{i+2})^2 & \frac{1}{6}(\Delta r_{i+1} + \Delta r_{i+2})^3 \end{bmatrix} \tag{B.1}$$

and

$$B = \begin{bmatrix} 0 & 0 & 0 & 0 \\ 0 & 1 & 0 & 0 \\ 0 & 0 & 0 & 0 \\ 0 & 0 & 0 & 0 \end{bmatrix}, \tag{B.2}$$

and the relevant vectors are

$$\mathbf{x_0} = \begin{bmatrix} f_{i-2}^n \\ f_{i-1}^n \\ f_{i+1}^n \\ f_{i+2}^n \end{bmatrix}, \tag{B.3}$$

$$\mathbf{x'} = \begin{bmatrix} f_i^n \\ f_i^{n\prime} \\ f_i^{n\prime\prime} \\ f_i^{n\prime\prime\prime} \end{bmatrix}, \tag{B.4}$$

and

$$\mathbf{x^\star} = \begin{bmatrix} 0 \\ f_i^{n\prime} \\ 0 \\ 0 \end{bmatrix}, \tag{B.5}$$

Solving the previous matrix equation and using the coefficients on the following page, it can be shown that the appropriate difference formula is

$$\frac{\partial f}{\partial r}\left(t = t_n, r = r_i\right) \approx -\frac{N_{i-2}}{D_{i-2}} f_{i-2}^n + \frac{N_{i-1}}{D_{i-1}} f_{i-1}^n - \frac{N_{i+1}}{D_{i+1}} f_{i+1}^n + \frac{N_{i+2}}{D_{i+2}} f_{i+2}^n, \tag{B.6}$$

with

$$N_{i-2} = -\Delta r_{i+1}\Delta r_{i-1} - \Delta r_{i+1}(\Delta r_{i+1} + \Delta r_{i+1}) + \Delta r_{i-1}(\Delta r_{i+1} + \Delta r_{i+1}), \quad \text{(B.7)}$$

$$D_{i-2} = (\Delta r_{i+1} + (\Delta r_{i-2} + \Delta r_{i-1}))((\Delta r_{i+1} + \Delta r_{i+1}) + (\Delta r_{i-2} + \Delta r_{i-1}))(\Delta r_{i-1} - (\Delta r_{i-2} + \Delta r_{i-1})), \quad \text{(B.8)}$$

$$N_{i-1} = \Delta r_{i+1}(\Delta r_{i-2} + \Delta r_{i-1}) - \Delta r_{i+1}(\Delta r_{i+1} + \Delta r_{i+1}) + (\Delta r_{i+1} + \Delta r_{i+1})(\Delta r_{i-2} + \Delta r_{i-1}), \quad \text{(B.9)}$$

$$D_{i-1} = (\Delta r_{i+1} + \Delta r_{i-1})(\Delta r_{i-1} + (\Delta r_{i+1} + \Delta r_{i+1}))(\Delta r_{i-1} - (\Delta r_{i-2} + \Delta r_{i-1})), \quad \text{(B.10)}$$

$$N_{i+1} = \Delta r_{i-1}(\Delta r_{i+1} + \Delta r_{i+1}) - \Delta r_{i-1}(\Delta r_{i-2} + \Delta r_{i-1}) + (\Delta r_{i+1} + \Delta r_{i+1})(\Delta r_{i-2} + \Delta r_{i-1}), \quad \text{(B.11)}$$

$$D_{i+1} = (\Delta r_{i+1} + \Delta r_{i-1})(\Delta r_{i+1} + (\Delta r_{i-2} + \Delta r_{i-1}))(\Delta r_{i+1} - (\Delta r_{i+1} + \Delta r_{i+1})), \tag{B.12}$$

$$N_{i+2} = \Delta r_{i+1}\Delta r_{i-1} + \Delta r_{i+1}(\Delta r_{i-2} + \Delta r_{i-1}) - \Delta r_{i-1}(\Delta r_{i-2} + \Delta r_{i-1}), \tag{B.13}$$

and

$$D_{i+2} = (\Delta r_{i-1} + (\Delta r_{i+1} + \Delta r_{i+1}))((\Delta r_{i+1} + \Delta r_{i+1}) + (\Delta r_{i-2} + \Delta r_{i-1}))(\Delta r_{i+1} - (\Delta r_{i+1} + \Delta r_{i+1})). \tag{B.14}$$

REFERENCES

Allred, J. C., Alaoui, M., Kowalski, A. F. & Kerr, G. S. 2020. Modeling the Transport of Nonthermal Particles in Flares Using Fokker-Planck Kinetic Theory. *Astrophysical Journal*, 902, 16, doi: 10.3847/1538-4357/abb239

Aptekar, R. L., Frederiks, D. D., Golenetskii, S. V., et al. 1995. Konus-W Gamma-Ray Burst Experiment for the GGS Wind Spacecraft. *Space Science Reviews*, 71, 265, doi: 10.1007/BF00751332

Aschwanden, M. J. 2019. Global Energetics of Solar Flares. IX. Refined Magnetic Modeling. *Astrophysical Journal*, 885, 49, doi: 10.3847/1538-4357/ab46c1

Asplund, M., Grevesse, N., Sauval, A. J. & Scott, P. 2009. The Chemical Composition of the Sun. *Annual Review of Astronomy & Astrophysics*, 47, 481, doi: 10.1146/annurev.astro.46.060407.145222

Babcock, H. W. 1961. The Topology of the Sun's Magnetic Field and the 22-YEAR Cycle. *Astrophysical Journal*, 133, 572, doi: 10.1086/147060

Birch, A. C., Braun, D. C. & Fan, Y. 2010. An Estimate of the Detectability of Rising Flux Tubes. *Astrophysical Journal Letters*, 723, L190, doi: 10.1088/2041-8205/723/2/L190

Birch, A. C., Braun, D. C., Leka, K. D., Barnes, G. & Javornik, B. 2013. Helioseismology of Pre-emerging Active Regions. II. Average Emergence Properties. *Astrophysical Journal*, 762, 131, doi: 10.1088/0004-637X/762/2/131

Birch, A. C. & Felder, G. 2004. Accuracy of the Born and Ray Approximations for Time-Distance Helioseismology of Flows. *Astrophysical Journal*, 616, 1261, doi: 10.1086/424961

Birch, A. C., Kosovichev, A. G., Price, G. H. & Schlottmann, R. B. 2001. The Accuracy of the Born and Ray Approximations in Time-Distance Helioseismology. *Astrophysical Journal Letters*, 561, L229, doi: 10.1086/324766

Bobra, M. G. & Couvidat, S. 2015. Solar Flare Prediction Using SDO/HMI Vector Magnetic Field Data with a Machine-learning Algorithm. *Astrophysical Journal*, 798, 135, doi: 10.1088/0004-637X/798/2/135

Braun, D. C. 2012. Comment on "Detection of Emerging Sunspot Regions in the Solar Interior". *Science*, 336, 296, doi: 10.1126/science.1215425

Braun, D. C. 2016. A Helioseismic Survey of Near-surface Flows Around Active Regions and their Association with Flares. *Astrophysical Journal*, 819, 106, doi: 10.3847/0004-637X/819/2/106

Braun, D. C. & Birch, A. C. 2008. Surface-Focused Seismic Holography of Sunspots: I. Observations. *Solar Physics*, 251, 267, doi: 10.1007/s11207-008-9152-5

Braun, D. C., Lindsey, C., Werne, J., et al. 2010. The Stanford Synoptic Seismic Monitor of the Sun's Far Hemisphere, Tech. rep., Joint Science Operations Center, Stanford University. http://jsoc.stanford.edu/data/farside/explanation.pdf [accessed on August 1, 2022]

Brown, J. C. 1971. The Deduction of Energy Spectra of Non-Thermal Electrons in Flares from the Observed Dynamic Spectra of Hard X-Ray Bursts. *Solar Physics*, 18, 489, doi: 10.1007/BF00149070

Brummell, N., Cline, K. & Cattaneo, F. 2002. Formation of Buoyant Magnetic Structures by a Localized Velocity Shear. *Monthly Notices of the Royal Astronomical Society*, 329, L73, doi: 10.1046/j.1365-8711.2002.05183.x

Cally, P. S. 2005. Local Magnetohelioseismology of Active Regions. *Monthly Notices of the Royal Astronomical Society*, 358, 353, doi: 10.1111/j.1365-2966.2005.08742.x

Carroll, B. W. & Ostlie, D. A. 1996, An Introduction to Modern Astrophysics (Reading, MA: Addison-Wessley)

Chen, P. F. 2011. Coronal Mass Ejections: Models and Their Observational Basis. *Living Reviews in Solar Physics*, 8, 1, doi: 10.12942/lrsp-2011-1

Chen, R. 2019. Helioseismic Measurements of the SUN'S Meridional Circulation and Sunquakes. PhD thesis, Stanford University, Stanford, CA

Christensen-Dalsgaard, J. 2002. Helioseismology. *Reviews of Modern Physics*, 74, 1073, doi: 10.1103/RevModPhys.74.1073

Christensen-Dalsgaard, J., Gough, D. O. & Thompson, M. J. 1988. Determination of the Solar Internal Sound Speed by Means of a Differential Asymptotic Inversion. In European Space Agency Special Publication, Vol. 286, *Seismology of the Sun and Sun-Like Stars*, ed. E. J. Rolfe, Paris, France, 493–497

Christensen-Dalsgaard, J., Dappen, W., Ajukov, S. V., et al. 1996. The Current State of Solar Modeling. *Science*, 272, 1286, doi: 10.1126/science.272.5266.1286

Cline, K. S., Brummell, N. H. & Cattaneo, F. 2003. On the Formation of Magnetic Structures by the Combined Action of Velocity Shear and Magnetic Buoyancy. *Astrophysical Journal*, 588, 630, doi: 10.1086/373894

Cliver, E. W., Schrijver, C. J., Shibata, K. & Usoskin, I. G. 2022. Extreme Solar Events. *Living Reviews in Solar Physics*, 19, 2, doi: 10.1007/s41116-022-00033-8

Courant, R., Friedrichs, K. & Lewy, H. 1967. On the Partial Difference Equations of Mathematical Physics. *IBM Journal of Research and Development*, 11, 215, doi: 10.1147/rd.112.0215

Couvidat, S. & Birch, A. C. 2006. Optimal Gaussian Phase-Speed Filters in Time-Distance Helioseismology. *Solar Physics*, 237, 229, doi: 10.1007/s11207-006-0209-z

Couvidat, S., Birch, A. C., Kosovichev, A. G. & Zhao, J. 2004. Three-dimensional Inversion of Time-Distance Helioseismology Data: Ray-Path and Fresnel-Zone Approximations. *Astrophysical Journal*, 607, 554, doi: 10.1086/383342

Couvidat, S., Schou, J., Hoeksema, J. T., et al. 2016. Observables Processing for the Helioseismic and Magnetic Imager Instrument on the Solar Dynamics Observatory. *Solar Physics*, 291, 1887, doi: 10.1007/s11207-016-0957-3

Donea, A. C. & Lindsey, C. 2005. Seismic Emission from the Solar Flares of 2003 October 28 and 29. *Astrophysical Journal*, 630, 1168, doi: 10.1086/432155

Duvall, T. L., J., Jefferies, S. M., Harvey, J. W. & Pomerantz, M. A. 1993. Time-distance Helioseismology. *Nature*, 362, 430, doi: 10.1038/362430a0

Fan, Y. 2004. Magnetic Fields in the Solar Convection Zone. *Living Reviews in Solar Physics*, 1, 1, doi: 10.12942/lrsp-2004-1

—. 2008. The Three-dimensional Evolution of Buoyant Magnetic Flux Tubes in a Model Solar Convective Envelope. *Astrophysical Journal*, 676, 680, doi: 10.1086/527317

Felipe, T., Braun, D. C., Crouch, A. D. & Birch, A. C. 2016. Helioseismic Holography of Simulated Sunspots: Magnetic and Thermal Contributions to Travel Times. *Astrophysical Journal*, 829, 67, doi: 10.3847/0004-637X/829/2/67

Fisher, G. H., Canfield, R. C. & McClymont, A. N. 1985. Flare Loop Radiative Hydrodynamics. V - Response to Thick-target Heating. VI - Chromospheric Evaporation due to Heating by Nonthermal Electrons. VII - Dynamics of the Thick-target Heated Chromosphere. *Astrophysical Journal*, 289, 414, doi: 10.1086/162901

Gizon, L. 2006. Tomography of the Solar Interior. *Modern Physics Letters A*, 21, 1701, doi: 10.1142/S0217732306021207

Gizon, L. & Birch, A. C. 2002. Time-Distance Helioseismology: The Forward Problem for Random Distributed Sources. *Astrophysical Journal*, 571, 966, doi: 10.1086/340015

—. 2005. Local Helioseismology. *Living Reviews in Solar Physics*, 2, 6, doi: 10.12942/lrsp-2005-6

Gizon, L., Fournier, D., Yang, D., Birch, A. C. & Barucq, H. 2018. Signal and Noise in Helioseismic Holography. *Astronomy & Astrophysics*, 620, A136, doi: 10.1051/0004-6361/201833825

Gough, D. O. 1993. Linear Adiabatic Stellar pulsation. In *Astrophysical Fluid Dynamics - Les Houches 1987* (Amsterdam, Netherlands: Elsevier), 399–560

Hartlep, T., Kosovichev, A. G., Zhao, J. & Mansour, N. N. 2011. Signatures of Emerging Subsurface Structures in Acoustic Power Maps of the Sun. *Solar Physics*, 268, 321, doi: 10.1007/s11207-010-9544-1

Hartlep, T., Zhao, J., Mansour, N. N. & Kosovichev, A. G. 2008. Validating Time-Distance Far-Side Imaging of Solar Active Regions through Numerical Simulations. *Astrophysical Journal*, 689, 1373, doi: 10.1086/592721

Hathaway, D. H. 2015. The Solar Cycle. *Living Reviews in Solar Physics*, 12, 4, doi: 10.1007/lrsp-2015-4

Hess Webber, S. A., Chen, R., DeRosa, M. L., Upton, L. & Zhao, J. 2020. Using New Acoustically-Derived Solar Far-Side Magnetic-Flux Maps for Data Assimilation in Flux Transport Models. In *American Geophysical Union Fall Meeting Abstracts*, Vol. 2020, SH002–0005

Hudson, H. S. 2011. Global Properties of Solar Flares. *Space Science Reviews*, 158, 5, doi: 10.1007/s11214-010-9721-4

Hughes, D. W., Falle, S. A. E. G. & Joarder, P. 1998. The Rise of Twisted Magnetic Flux Tubes. *Monthly Notices of the Royal Astronomical Society*, 298, 433, doi: 10.1046/j.1365-8711.1998.01622.x

Ilonidis, S., Zhao, J. & Hartlep, T. 2013. Helioseismic Investigation of Emerging Magnetic Flux in the Solar Convection Zone. *Astrophysical Journal*, 777, 138, doi: 10.1088/0004-637X/777/2/138

Ilonidis, S., Zhao, J. & Kosovichev, A. 2011. Detection of Emerging Sunspot Regions in the Solar Interior. *Science*, 333, 993, doi: 10.1126/science.1206253

Ilonidis, S., Zhao, J. & Kosovichev, A. G. 2012. Helioseismic Detection of Emerging Magnetic Flux. In Astronomical Society of the Pacific Conference Series, Vol. 462, *Progress in Solar/Stellar Physics with Helio- and Asteroseismology*, ed. H. Shibahashi, M. Takata, & A. E. Lynas-Gray (San Francisco, CA: Astronomical Society of the Pacific), 283. https://arxiv.org/abs/1203.2546 [accessed on May 1, 2021]

Jain, K., Komm, R. W., González Hernández, I., Tripathy, S. C. & Hill, F. 2012. Subsurface Flows in and Around Active Regions with Rotating and Non-rotating Sunspots. *Solar Physics*, 279, 349, doi: 10.1007/s11207-012-0039-0

Jain, R. 2007. Effects of Horizontal Magnetic Fields on Acoustic Travel Times. *Astrophysical Journal*, 656, 610, doi: 10.1086/510349

Jeffery, D. J. & Branch, D. 1990. Analysis of Supernova Spectra. In *Supernovae, Jerusalem Winter School for Theoretical Physics*, ed. J. C. Wheeler, T. Piran, & S. Weinberg, Vol. 6, Jerusalem, Israel, 149

Joint Science Operations Center. 2022. Stanford Seismic Monitor of the Sun's Far Hemisphere for the Solar Dynamics Observatory: Composite Maps of Full Sun. http://jsoc.stanford.edu/data/farside/Composite_Maps_JPEG/COMPOSITE_MAP_2022.07.29_00:00:00.png [accessed on August 1, 2022]

Kholikov, S. 2013. A Search for Helioseismic Signature of Emerging Active Regions. *Solar Physics*, 287, 229, doi: 10.1007/s11207-013-0321-9

Khomenko, E. & Collados, M. 2006. Numerical Modeling of Magnetohydrodynamic Wave Propagation and Refraction in Sunspots. *Astrophysical Journal*, 653, 739, doi: 10.1086/507760

Kosovichev, A. G. 2006. Direct Observations of Acoustic Waves Excited by Solar Flares and their Propagation in Sunspot Regions. *SoPh*, 277, 59

—. 2011, In Lecture Notes in Physics, ed. J.-P. Rozelot & C. Neiner, Vol. 832 (Berlin, Germany: Springer Verlag), 3, doi: 10.1007/978-3-642-19928-8_1

—. 2015, Sunquakes: Helioseismic response to solar flares, in: Extraterrestrial Seismology (Cambridge, United Kingdom: Cambridge University Press), 306–322, doi: 10.1017/CBO9781107300668.025

Kosovichev, A. G. & Duvall, T. L., J. 1997. Acoustic Tomography of Solar Convective Flows and Structures. In Astrophysics and Space Science Library, Vol. 225, *SCORe'96 : Solar Convection and Oscillations and their Relationship*, ed. F. P. Pijpers, J. Christensen-Dalsgaard, & C. S. Rosenthal (Dordrecht, Germany: Springer Dordrecht), 241–260, doi: 10.1007/978-94-011-5167-2_26

Kosovichev, A. G., Duvall, T. L., J. & Scherrer, P. H. 2001. Probing Magnetic Structures in the Solar Interior by Helioseismic Tomography. In Astronomical Society of the Pacific Conference Series, Vol. 248, *Magnetic Fields Across the Hertzsprung-Russell Diagram*, ed. G. Mathys, S. K. Solanki, & D. T. Wickramasinghe (San Francisco, CA: Astronomical Society of the Pacific), 169

Kosovichev, A. G., Duvall, T. L. ,Jr., J. & Scherrer, P. H. 2000. Time-Distance Inversion Methods and Results - (Invited Review). *Solar Physics*, 192, 159, doi: 10.1023/A:1005251208431

Kosovichev, A. G. & Zharkova, V. V. 1995. Seismic Response to Solar Flares: Theoretical Predictions. In European Space Agency Special Publication, Vol. 376, *Helioseismology*, Paris, France, 341

Kosovichev, A. G. & Zharkova, V. V. 1998. X-ray flare sparks quake inside Sun. *Nature*, 393, 317, doi: 10.1038/30629

Leighton, R. B. 1964. Transport of Magnetic Fields on the Sun. *Astrophysical Journal*, 140, 1547, doi: 10.1086/148058

Lindsey, C. & Braun, D. C. 1997. Helioseismic Holography. *Astrophysical Journal*, 485, 895, doi: 10.1086/304445

—. 2000. Basic Principles of Solar Acoustic Holography - (Invited Review). *Solar Physics*, 192, 261, doi: 10.1023/A:1005227200911

—. 2005. The Acoustic Showerglass. I. Seismic Diagnostics of Photospheric Magnetic Fields. *Astrophysical Journal*, 620, 1107, doi: 10.1086/426065

Lindsey, C., Buitrago-Casas, J. C., Martínez Oliveros, J. C., et al. 2020. Submerged Sources of Transient Acoustic Emission from Solar Flares. *Astrophysical Journal Letters*, 901, L9, doi: 10.3847/2041-8213/abad2a

Livingston, W. 2002. Sunspots Observed to Physically Weaken in 2000-2001. *Solar Physics*, 207, 41, doi: 10.1023/A:1015555000456

Lu, J., Gong, P., Ye, J. & Zhang, C. 2020. Learning from Very Few Samples: A Survey. *arXiv e-prints*, arXiv:2009.02653. https://arxiv.org/abs/2009.02653 [accessed on May 1, 2021]

Lysenko, A. L., Altyntsev, A. T., Meshalkina, N. S., Zhdanov, D. & Fleishman, G. D. 2018. Statistics of "Cold" Early Impulsive Solar Flares in X-ray and Microwave domains. *ApJ*, 887, 145. https://arxiv.org/abs/1802.09288 [accessed on May 1, 2021]

Macrae, C., Zharkov, S., Zharkova, V., et al. 2018. Lost and Found Sunquake in the 6 September 2011 Flare Caused by Beam Electrons. *Astronomy & Astrophysics*, 619, A65, doi: 10.1051/0004-6361/201832896

Malanushenko, A., Braun, D., Kholikov, S., Leibacher, J. & Lindsey, C. 2004. Acoustic Holographic Studies of Solar Active Regions. In *Multi-Wavelength Investigations of Solar Activity*, ed. A. V. Stepanov, E. E. Benevolenskaya, & A. G. Kosovichev, Vol. 223, 283–284, doi: 10.1017/S1743921304005940

Martinez Pillet, V. & Vazquez, M. 1993. The Continuum Intensity-Magnetic Field Relation in Sunspot Umbrae. *Astronomy & Astrophysics*, 270, 494

Masuda, S., Kosugi, T., Hara, H., Tsuneta, S. & Ogawara, Y. 1994. A loop-top hard X-ray source in a compact solar flare as evidence for magnetic reconnection. *Nature*, 371, 495, doi: 10.1038/371495a0

Moradi, H., Hanasoge, S. M. & Cally, P. S. 2009. Numerical Models of Travel-Time Inhomogeneities in Sunspots. *Astrophysical Journal Letters*, 690, L72, doi: 10.1088/0004-637X/690/1/L72

Munoz-Jaramillo, A., Jungbluth, A., Gitiaux, X., et al. 2021. Cross-calibration, super-resolution, and uncertainty estimation of the conversion of MDI and GONG to HMI full-disk magnetograms using deep learning. In American Astronomical Society Meeting Abstracts, Vol. 53, *American Astronomical Society Meeting Abstracts* (Washington, DC: AAS Publishing), 123.03

Neupert, W. M. 1968. Comparison of Solar X-Ray Line Emission with Microwave Emission during Flares. *Astrophysical Journal Letters*, 153, L59, doi: 10.1086/180220

Nigam, R., Kosovichev, A. G. & Scherrer, P. H. 2007. Analytical Models for Cross-Correlation Signal in Time-Distance Helioseismology. *Astrophysical Journal*, 659, 1736, doi: 10.1086/512535

Parchevsky, K. V. & Kosovichev, A. G. 2009. Numerical Simulation of Excitation and Propagation of Helioseismic MHD Waves: Effects of Inclined Magnetic Field. *Astrophysical Journal*, 694, 573, doi: 10.1088/0004-637X/694/1/573

Parker, E. N. 1979. Sunspots and the Physics of Magnetic Flux Tubes. I. The General Nature of the Sunspots. *Astrophysical Journal*, 230, 905, doi: 10.1086/157150

Pedram, E. & Matthews, S. A. 2012. A Survey of the Hard X-Ray Characteristics of Seismically Active and Quiet White-Light Flares. *Solar Physics*, 277, 317, doi: 10.1007/s11207-011-9922-3

Priest, E. R. & Forbes, T. G. 2002. The Magnetic nature of Solar Flares. *Astronomy & Astrophysics Reviews*, 10, 313, doi: 10.1007/s001590100013

Prokakis, T. 1974. The Depth of Sunspots. *Solar Physics*, 35, 105, doi: 10.1007/BF00156960

Rempel, M. 2012. Numerical Sunspot Models: Robustness of Photospheric Velocity and Magnetic Field Structure. *Astrophysical Journal*, 750, 62, doi: 10.1088/0004-637X/750/1/62

Rhodes, E. J., J., Reiter, J., Schou, J., et al. 2011. Temporal Changes in the Frequencies and Widths of the Solar P-mode Oscillations. In Journal of Physics Conference Series, Vol. 271, *GONG-SoHO 24: A New Era of Seismology of the Sun and Solar-Like Stars* (Bristol, United Kingdom: IOP Publishing), 012029, doi: 10.1088/1742-6596/271/1/012029

Rickett, J. E. & Claerbout, J. F. 2000. Calculation of the Sun's Acoustic Impulse Response by Multi-Dimensional Spectral Factorization. *Solar Physics*, 192, 203, doi: 10.1023/A:1005205406377

Rimmele, T. R., Goode, P. R., Harold, E. & Stebbins, R. T. 1995. Dark Lanes in Granulation and the Excitation of Solar Oscillations. *Astrophysical Journal Letters*, 444, L119, doi: 10.1086/187874

Row, R. V. 1967. Acoustic-gravity Waves in the Upper Atmosphere due to a Nuclear Detonation and an Earthquake. *Journal of Geophysics Research*, 72, 1599, doi: 10.1029/JZ072i005p01599

Schou, J., Antia, H. M., Basu, S., et al. 1998. Helioseismic Studies of Differential Rotation in the Solar Envelope by the Solar Oscillations Investigation Using the Michelson Doppler Imager. *Astrophysical Journal*, 505, 390, doi: 10.1086/306146

Schrijver, C. J. 2007. A Characteristic Magnetic Field Pattern Associated with All Major Solar Flares and Its Use in Flare Forecasting. *Astrophysical Journal Letters*, 655, L117, doi: 10.1086/511857

Sharykin, I. N. & Kosovichev, A. G. 2020. Sunquakes of Solar Cycle 24. *Astrophysical Journal*, 895, 76, doi: 10.3847/1538-4357/ab88d1

Sharykin, I. N., Kosovichev, A. G., Sadykov, V. M., Zimovets, I. V. & Myshyakov, I. I. 2017. Investigation of Relationship between High-energy X-Ray Sources and Photospheric and Helioseismic Impacts of X1.8 Solar Flare of 2012 October 23. *Astrophysical Journal*, 843, 67, doi: 10.3847/1538-4357/aa77f1

Singh, N. K., Raichur, H. & Brandenburg, A. 2016. High-wavenumber Solar F-mode Strengthening Prior to Active Region Formation. *Astrophysical Journal*, 832, 120, doi: 10.3847/0004-637X/832/2/120

Skartlien, R. & Rast, M. P. 2000. P-mode Intensity-Velocity Phase Differences and Convective Sources. *Astrophysical Journal*, 535, 464, doi: 10.1086/308845

Solanki, S. K. 2003. Sunspots: An Overview. *Astronomy & Astrophysics Reviews*, 11, 153, doi: 10.1007/s00159-003-0018-4

Stefan, J. T. & Kosovichev, A. G. 2020. Estimation of Key Sunquake Parameters through Hydrodynamic Modeling and Cross-correlation Analysis. *Astrophysical Journal*, 895, 65, doi: 10.3847/1538-4357/ab88ae

—. 2022. Detection of Travel Time Anisotropy from Subsurface Horizontal Magnetic Fields. *Astrophysical Journal*, 930, 10, doi: 10.3847/1538-4357/ac602a

Stefan, J. T., Kosovichev, A. G. & Stejko, A. M. 2021. Analysis of Time-Distance Helioseismology for Detection of Emerging Active Regions. *Astrophysical Journal*, 913, 87, doi: 10.3847/1538-4357/abf2bf

Stejko, A. M., Kosovichev, A. G. & Mansour, N. N. 2021. Helioseismic Modeling of Background Flows. *Astrophysical Journal Supplement*, 253, 9, doi: 10.3847/1538-4365/abd3fe

Tassoul, M. 1980. Asymptotic Approximations for Stellar Nonradial Pulsations. *Astrophysical Journal Supplement*, 43, 469, doi: 10.1086/190678

Toriumi, S., Ilonidis, S., Sekii, T. & Yokoyama, T. 2013. Probing the Shallow Convection Zone: Rising Motion of Subsurface Magnetic Fields in the Solar Active Region. *Astrophysical Journal Letters*, 770, L11, doi: 10.1088/2041-8205/770/1/L11

Tschernitz, J., Veronig, A. M., Thalmann, J. K., Hinterreiter, J. & Pötzi, W. 2018. Reconnection Fluxes in Eruptive and Confined Flares and Implications for Superflares on the Sun. *Astrophysical Journal*, 853, 41, doi: 10.3847/1538-4357/aaa199

UCAR. 2011. Learning Zone: Sun and Space Weather: Sunspots. https://scied.ucar.edu/learning-zone/sun-space-weather/sunspots [accessed on August 1, 2022]

Ulyanov, A. S., Bogachev, S. A., Loboda, I. P., Reva, A. A. & Kirichenko, A. S. 2019. Direct Evidence for Magnetic Reconnection in a Solar EUV Nanoflare. *Solar Physics*, 294, 128, doi: 10.1007/s11207-019-1472-0

Vallis, G. K. 2006, Atmospheric and Oceanic Fluid Dynamics (Cambridge, United Kingdom: Cambridge University Press)

Vernazza, J. E., Avrett, E. H. & Loeser, R. 1981. Structure of the Solar Chromosphere. III. Models of the EUV Brightness Components of the Quiet Sun. *Astrophysical Journal Supplement*, 45, 635, doi: 10.1086/190731

Veronig, A., Temmer, M., Hanslmeier, A., Otruba, W. & Messerotti, M. 2002. Temporal Aspects and Frequency Distributions of Solar Soft X-ray Flares. *Astronomy & Astrophysics*, 382, 1070, doi: 10.1051/0004-6361:20011694

Vögler, A., Shelyag, S., Schüssler, M., et al. 2005. Simulations of Magneto-convection in the Solar Photosphere. Equations, Methods, and Results of the MURaM code. *Astronomy & Astrophysics*, 429, 335, doi: 10.1051/0004-6361:20041507

Vranjes, J. 2014. Viscosity Effects on Waves in Partially and Fully Ionized Plasma in Magnetic Field. *Monthly Notices of the Royal Astronomical Society*, 445, 1614, doi: 10.1093/mnras/stu1887

Wang, Y. & Zhang, J. 2007. A Comparative Study between Eruptive X-Class Flares Associated with Coronal Mass Ejections and Confined X-Class Flares. *Astrophysical Journal*, 665, 1428, doi: 10.1086/519765

Yashiro, S., Gopalswamy, N., Akiyama, S., Michalek, G. & Howard, R. A. 2005. Visibility of Coronal Mass Ejections as a Function of Flare Location and Intensity. *Journal of Geophysical Research (Space Physics)*, 110, A12S05, doi: 10.1029/2005JA011151

Zhao, J. 2007. Time-Distance Imaging of Solar Far-Side Active Regions. *Astrophysical Journal Letters*, 664, L139, doi: 10.1086/520837

Zhao, J. & Kosovichev, A. G. 2003. Helioseismic Observation of the Structure and Dynamics of a Rotating Sunspot Beneath the Solar Surface. *Astrophysical Journal*, 591, 446, doi: 10.1086/375343

Zhao, J., Couvidat, S., Bogart, R. S., et al. 2012. Time-Distance Helioseismology Data-Analysis Pipeline for Helioseismic and Magnetic Imager Onboard Solar Dynamics Observatory (SDO/HMI) and Its Initial Results. *Solar Physics*, 275, 375, doi: 10.1007/s11207-011-9757-y

Zharkova, V. & Zharkov, S. 2015. On the Generation of Hydrodynamic Shocks by Mixed Beams and Occurrence of Sunquakes in Flares. *Solar Physics*, 290, 3163, doi: 10.1007/s11207-015-0813-x

Zharkova, V. V. & Zharkov, S. I. 2007. On the Origin of Three Seismic Sources in the Proton-rich Flare of 2003 October 28. *Astrophysical Journal*, 664, 573, doi: 10.1086/518731